Cusp Ion Structures and Their Relation to Magnetopause Processes

BY

Hyun Ju Connor

B.S., Kyungpook National University (2002)
M.S., Kyungpook National University (2004)

DISSERTATION

Submitted to the University of New Hampshire
in partial fulfillment of
the requirements for the degree of

Doctor of Philosophy

in

Physics

May 2012

This dissertation has been examined and approved.

Dissertation director, Joachim Raeder

Professor of Physics

Silas R. Beane

Associate Professor of Physics

Lynn Kistler

Professor of Physics

Martin Lee

Professor of Physics

Eberhard Möbius

Professor of Physics

Date

Dedication

To my parents, Boya Lee and Daewoo Kim.

Acknowledgments

I would like to express my deepest gratitude to my advisor, Joachim Raeder, for his excellent guidance, support, and patience. He was always willing to take his time out of his busy schedule to discuss the details of my research. His insightful advice was always helpful to polish my ideas. I especially appreciated him waiting all these years for me to finish this dissertation research on my own pace. I truly believe that his experience gave me a valuable asset for my future.

I am very appreciated to my collaborator, Dr. K. J. Trattner. The discussions we had at every GEM and AGU meeting were very pleasant and fruitful for me to understand my research subject. His suggestions and questions also helped me in developing my research.

To Professor Silas R. Beane, Lynn Kistler, Martin Lee, and Eberhard Möbius, I'd like to thank you all for accepting to be my committee members, and attending my thesis proposal, annual meeting, and thesis defense. Your collective advice was invaluable. I also thank you to read my dissertation thoroughly.

I greatly appreciate Erin Somers, Douglas Larson, and Matt Argil for editing my dissertation despite my incessant bothering. English has never been easy to me. Without their help, I would not finish my dissertation on time.

I'd like to thank to my parents, Boya Lee and Daewoo Kim. Their love always gave me a strength to go forward. My mother, a successful Korean costume designer, inspired me to be enthusiastic and passionate in my job. My father taught me patience which helped me on track. I am very proud of being their daughter.

I also wish to thank my husband, Taylor Connor, for being next to me and listening to all my complaints and doubts about future, and my dog, Indiana Jones, for his fun nature which made me laugh even when I was depressed and sad.

This dissertation research was supported by grants ATM-0503189 and ATM-0639658 from the National Science Foundation, grant NNX10AL07G from the National Aeronautics and Space Administration. I especially thank to the Korean Science and Engineering Foundation for supporting me for the first two years in USA (grant C00058). Without their support, living in the USA would be much more difficult.

Table of Contents

List of Tables

List of Figures

ABSTRACT

Cusp Ion Structures and Their Relation to Magnetopause Processes

by

Hyun Ju Connor
University of New Hampshire, May, 2012

Dispersed ion structures observed near the magnetosphere cusps have long been used to infer locations and properties of reconnection at the Earth's magnetopause. However, observations are often difficult to interpret since spacecraft move relative to a cusp ion structure, creating temporal/spatial ambiguity in the observations. Models of cusp ion structures are also limited to the cases during stable solar wind and IMF because empirical models are used to obtain the Earth's electromagnetic fields. In this dissertation, we develop a dynamic model of cusp ion structures usable for non-steady solar wind and IMF cases by using the Liouville Theorem Particle Tracer (LTPT) with the OpenGGCM 3D global MHD model. We first test our model's validity by reconstructing cusp ion structures observed from Cluster and Polar satellites. Our model faithfully reproduces various observed cusp ion structures, such as normal dispersion, reverse dispersion, double dispersions, and stepped dispersion. We also demonstrate our model's ability to investigate magnetopause processes that relate to the cusp structures. By analyzing the precipitating pattern of cusp ions and the magnetopause movement, we find that sudden increase of solar wind pressure, non-steady reconnection rates, and change of IMF clock angle cause the various dispersions in the Cluster and Polar observations. After the model validation test, we study the general relation between cusp ion structures and magnetopause processes during four different IMF clock angles of 0°, 60°, 120°, and 180°. Our model produces a reverse dispersion, double reverse dispersions, a flat and dispersed structure, and a normal dispersion under each IMF condition, respectively. From the detailed study of the ion entry points and the reconnection patterns on the magnetopause, we find that lobe reconnection, recurring FTE formation,

coexistence of component and anti-parallel reconnection, and subsolar reconnection cause each cusp structure. We also find that cusp ions during northward IMF originate from an anti-parallel reconnection zone whose shear angle is over 170°. Conversely, during southward IMF ions precipitate not only from a high shear angle zone but also from a very low shear angle zone.

Chapter 1

Introduction

Magnetic reconnection is a major mechanism for transporting the mass, momentum, and energy of solar wind into the magnetosphere, causing various geomagnetic events on the Earth. In order to understand the global magnetospheric system, it is necessary to understand this mechanism. However, reconnection happens on scales of a few ion or electron inertial lengths. Therefore, the direct observation of a reconnection site is very difficult. With this restriction, scientists have studied the dynamic processes of reconnection which can be observed far from the reconnection site. High-speed plasma flows, flux transfer events, and cusp ion signatures are those events, and have been studied to infer the properties and locations of reconnection. In this dissertation, we will develop a dynamic model of cusp ion structure by using a state of the art MHD model and a particle tracer, and use it as a tool to study dayside reconnection processes.

1.1 The Earth's magnetosphere

The Earth's magnetosphere is a dynamic structure using solar wind energy as fuel. When the solar wind approaches the Earth, it first meets the bowshock, the boundary where solar wind plasma is abruptly slowed down, compressed, and heated. The region sunward of the bowshock is called "upstream", and the region anti-sunward is called "downstream". Solar wind plasma continues its journey to the Earth and

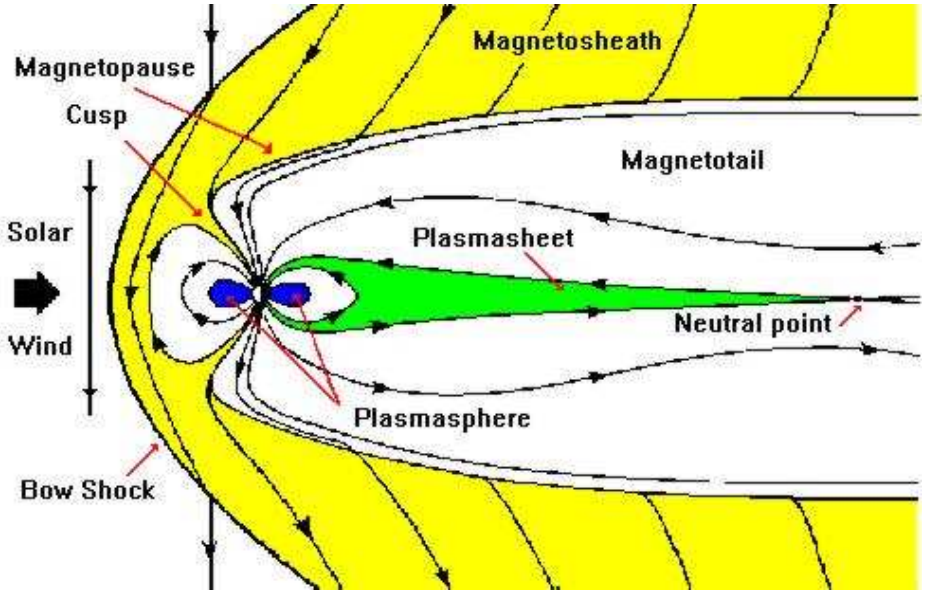

Figure 1-1: The Earth's magnetosphere.

meets another boundary called the magnetopause which separates the solar wind plasma from the Earth's magnetospheric plasma. The magnetic shear between the two plasma regions induces a strong current on the magnetopause, preventing the solar wind plasma from bombarding the Earth via the $\mathbf{J} \times \mathbf{B}$ force. The region between the bowshock and the magnetopause is called the magnetosheath. Figure 1-1 shows a configuration of the Earth's magnetosphere. The magnetopause is not a perfect shield. Magnetic reconnection occurs at the magnetopause, creating open field lines that connect interplanetary magnetic field to the Earth's magnetic field. Solar wind particles penetrate into the Earth's system via these open field lines. Some of the particles directly precipitate into the Earth's cusp, the funnel-like region in Figure 1-1, and some of them move toward the magnetotail. Magnetic reconnection also occurs in the magnetotail, producing extended closed field lines that convect earthward. Solar wind plasma comes back to the Earth's magnetosphere with these closed field lines, causing various geomagnetic events such as auroras, substorms, and

magnetic storms.

There are many theories about where and when dayside reconnection occurs. The theory of anti-parallel reconnection suggests that reconnection happens where the IMF becomes anti-parallel to the Earth's magnetic field. This reconnection happens near the subsolar region during southward IMF and the lobe region during northward IMF. These reconnection sites, also called X-lines, are shown in Figure 1-2 with the magnetic configuration of the dayside magnetosphere. The theory of component reconnection, on the other hand, insists that the angle between the IMF and the Earth's field, called the magnetic shear angle, does not need to be anti-parallel, and that a certain angle, usually more than 50°, is enough to produce reconnection. This component reconnection region is usually described as a line on the magnetopause that maximizes magnetic shear angle. Figure 1-3 shows dayside reconnection modes as a function of IMF clock angle, calculated from this component reconnection theory. The reconnection line, the white curved line, lies across the equatorial magnetopause during southward IMF, and tilts poleward as IMF B_y becomes dominant. For northward IMF, this reconnection line becomes a closed circle. Component reconnection, therefore, happens in much broader regions while anti-parallel reconnection occurs at only a few places on the magnetopause. There is also a possibility that both anti-parallel and component reconnection occur simultaneously.

1.2 Cusp ion structures

The Earth's magnetic cusps are funnel-like regions where solar wind plasma (which is heated and compressed in the magnetosheath) directly precipitates from the reconnection sites. The number density and energy in the cusps are nearly equal to those of the magnetosheath plasma, the former being ~ 10 cm^{-3} and the latter ~ 100 eV. Since solar wind particles move diamagnetically, the cusps have a higher number

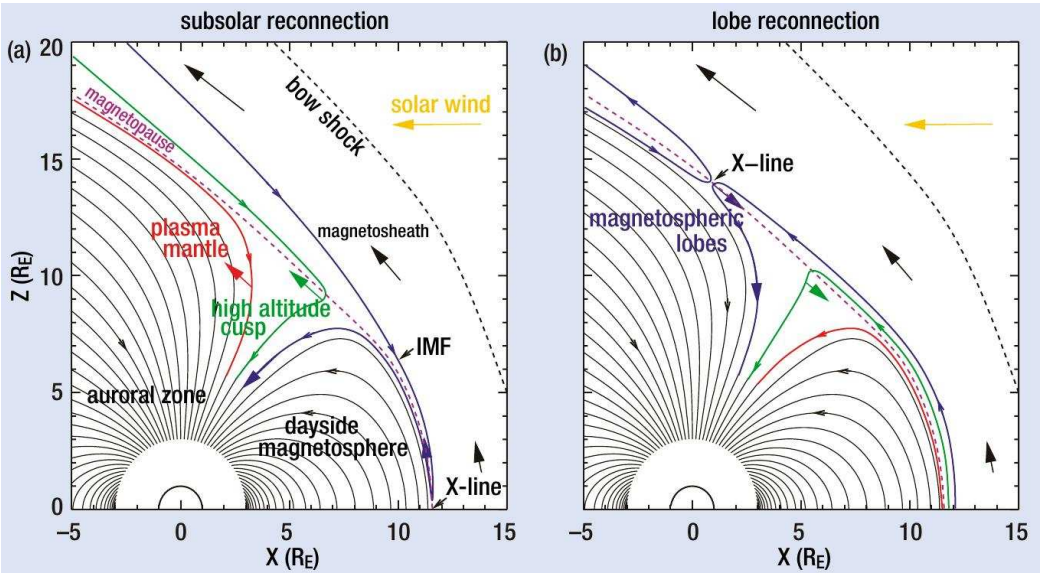

Figure 1-2: The magnetic field topology and the plasma flow at the high-altitude cusp (a) during southward IMF and (b) during northward IMF. [*Lavraud and Cargill et al.*, 2005] The magnetic field lines convect from the blue to the green, and then to the red line. The corresponding plasma flows are shown as the same colored arrows.

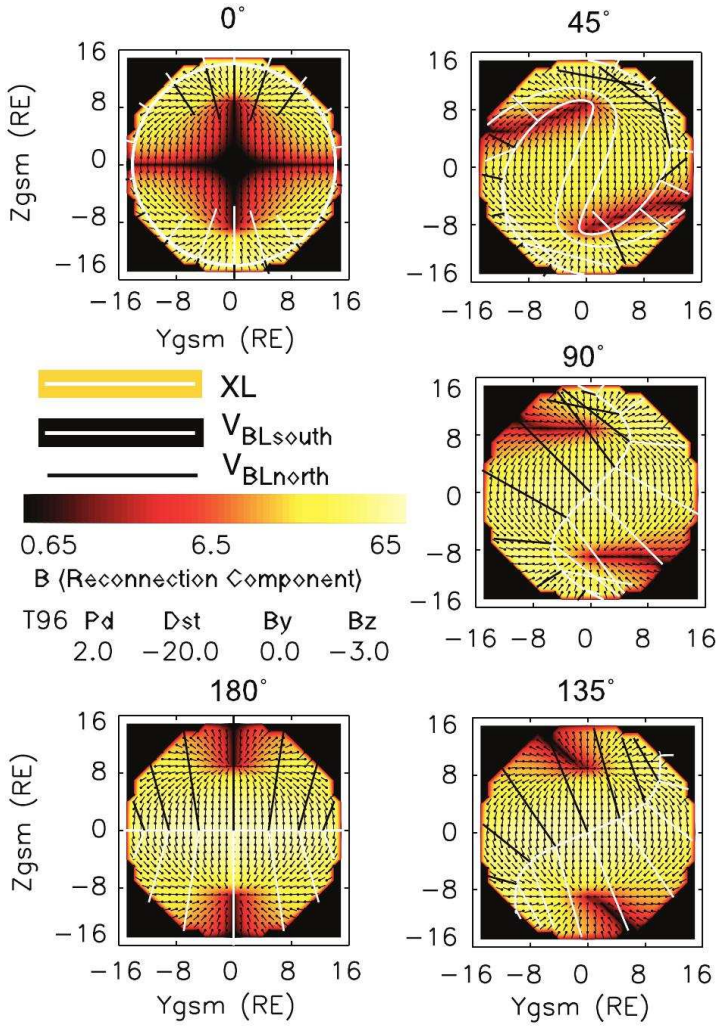

Figure 1-3: The dayside reconnection mode on the magnetopause as a function of IMF clock angle as viewed from the Sun. The curved white lines represent component reconnection lines. [*Moore et al.*, 2002]

density and lower magnetic field strength than the magnetosphere. The cusps are also regions full of open field lines, and extend from the open/closed field line boundary on the dayside magnetopause to where the magnetosheath plasma no longer directly precipitates [*Maynard*, 2005].

The cusps are under the direct impact of dayside reconnection. Reconnection happens on the dayside magnetopause where the interplanetary magnetic field (IMF) meets the Earth's magnetic field, and creates open field lines with one end on the Earth and the other end downtail in space. Solar wind plasma penetrates into the Earth's magnetosphere along these open field lines. As the field lines connect the cusps to the magnetopause, satellites in the cusp observe solar wind plasma precipitating from the reconnection sites wherever reconnection happens on the magnetopause. Therefore, the cusps provide a good environment to study dayside reconnection.

Cusp ion structures, as seen on an energy versus latitude (or energy versus time) spectrogram of cusp ions, display the precipitating patterns of solar wind plasma. During southward IMF, reconnection occurs near the subsolar region, creating kinked open field lines that convect tailward by magnetic tension force and magnetosheath flow. Figure 1-2(a) shows the magnetic field topology and plasma flow during southward IMF. The open field lines convect from the blue to the green, and then to the red line. The corresponding plasma flows are shown as the same-colored arrows. During the field line convection, magnetosheath particles precipitate into the cusp along the open field lines. Fast, high-energy ions arrive at the cusp earlier than the slow, low-energy ions. This is called the velocity filter effect [*Rosenbauer et al.*, 1975; *Shelley et al.*, 1976; *Reiff et al.*, 1977; *Hill and Reiff*, 1977]. As the field lines move tailward, high energy ions precipitate into the low latitudes of the cusp and low energy ions precipitate into the high latitudes of the cusp. Therefore, the energy versus latitude spectrogram shows high to low energy dispersion as the latitude increases.

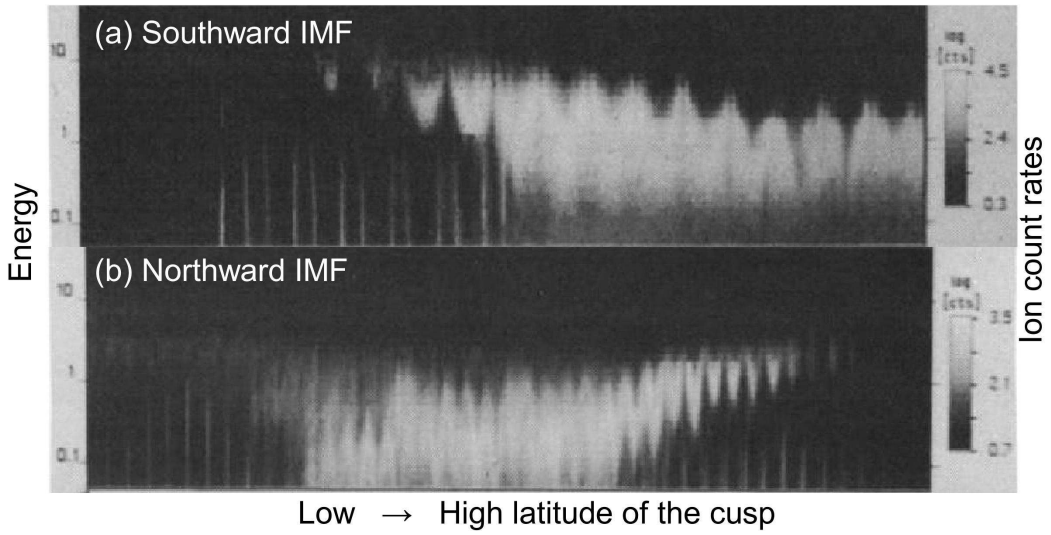

Figure 1-4: The energy versus latitude spectrograms of the cusp ions. (a) a normal dispersion during southward IMF and (b) a reverse dispersion during northward IMF. [modified from *Woch and Lundin*, 1992]

This dispersed structure is called a normal dispersion (See Figure 1-4(a)). During northward IMF, reconnection creates kinked open field lines near the magnetospheric lobes, as shown in Figure 1-2(b). As the open field lines convect equatorward by magnetic tension force, high-energy ions precipitate at high latitudes of the cusp, and low-energy ions precipitate at low latitudes of the cusp. The energy of precipitating ion, therefore, increases as the latitude increases. This dispersed structure is called a reverse dispersion (See Figure 1-4(b)).

Unlike these two simple cusp structures, cusp ion structures are often complicated (See Figure 1-5). More detailed studies are needed to understand the relation between cusp ion structures and dayside reconnection.

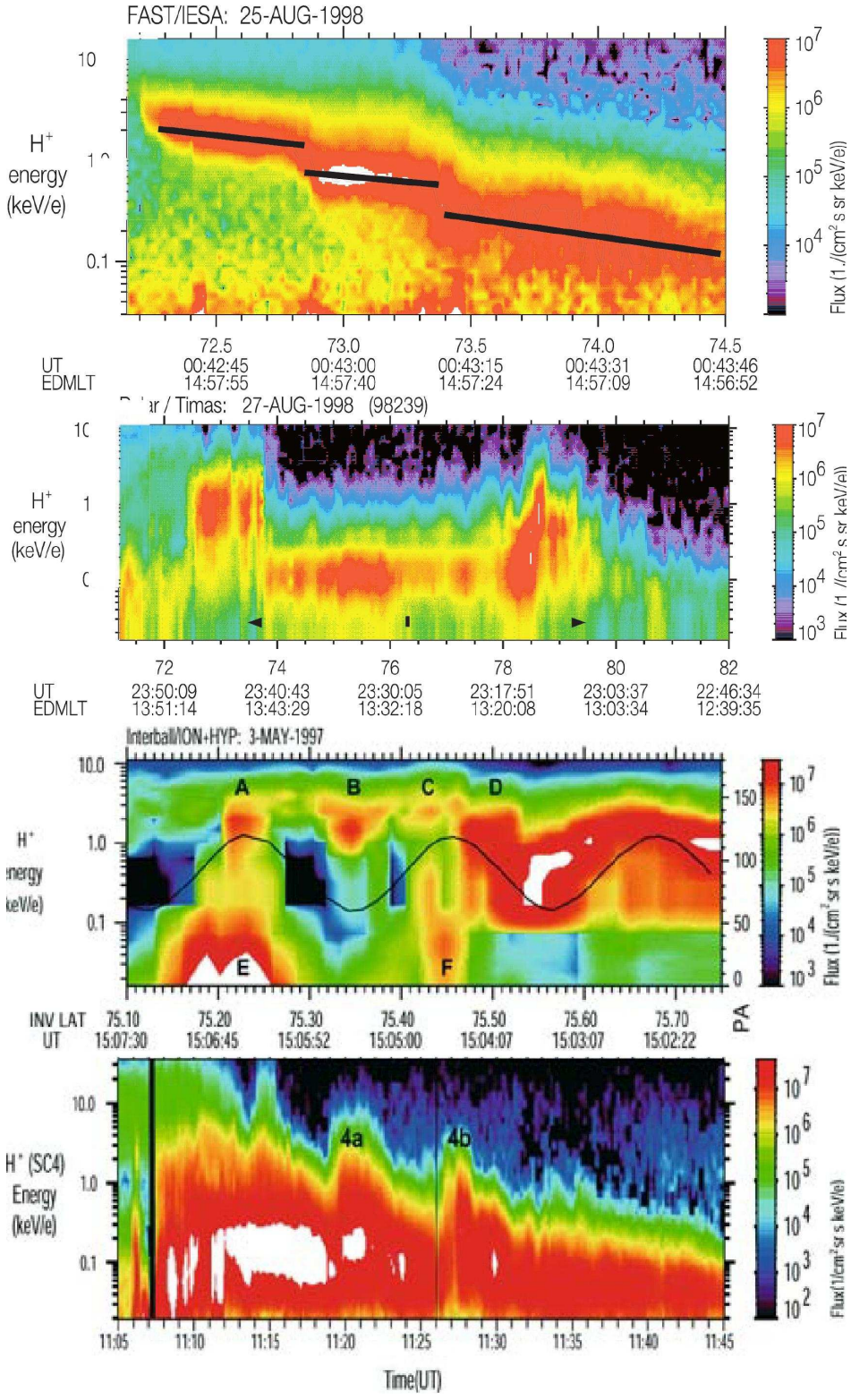

Figure 1-5: Various cusp ion structures from *Trattner et al.* [2002, 2005]

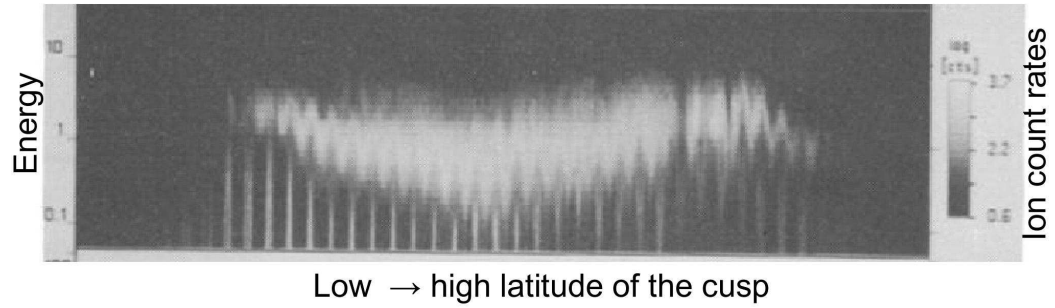

Figure 1-6: A V-shaped cusp ion structure. [modified from *Woch and Lundin*, 1992]

1.3 Temporal and spatial nature of cusp ion structures

Cusp ion structures are broadly divided into two categories: temporal and spatial structures. Temporal cusp structures are caused by temporal variations of dayside reconnection while spatial structures are produced by spatial variations. We can infer the reconnection properties by investigating in which category a cusp structure is included. In this section, we discuss how to distinguish the types of cusp structures and which reconnection property produces them by introducing examples of each.

Satellites move relative to the cusp, creating temporal and spatial ambiguities in the observations. To distinguish between the temporal versus spatial nature of cusp ion structures, at least two satellites need to be in the cusp. For example, consider that a satellite observes a V-shaped structure like the one shown in Figure 1-6. As we discussed in the previous section, subsolar reconnection produces a normal dispersion, and lobe reconnection produces a reverse dispersion. The V-shaped structure is the combination of these two dispersions. With one single satellite, we have two possible scenarios. The first scenario is that subsolar reconnection changes into lobe reconnection while a satellite moves from low to high latitude. The second scenario is that two reconnection sites coexist during the satellite's cusp crossing. These scenarios explain two different reconnection properties (temporal and spatial). To confirm the

reconnection property, we need one more satellite in the cusp to see if the V-shaped structure is stationary.

To distinguish temporal cusp ion structures, two satellites need to stay in different parts of the cusp at the same time. If both satellites observe similar structures at different locations approximately at the same time, the structures are considered to be temporal structures. *Trattner et al.* [2008] have studied this type of temporal event observed by Cluster spacecraft. Cluster is composed of four identical satellites which travel in tetrahedron formation, and is therefore perfect for distinguishing between temporal and spatial behavior of cusp ion structures. The top panel of Figure 1-7 shows solar wind conditions observed by WIND on 23 September 2001. Number density, solar wind velocity, IMF B_x (black line), B_y (green line), and B_z (shaded area) are plotted. The two vertical lines in the IMF plot represent when Cluster satellites (SC4 and SC1) enter the cusp. SC4 is located poleward of SC1, entering the cusp earlier than SC1. At the cusp entry of the Cluster satellites, IMF B_z is southward.

The bottom panel of Figure 1-7 shows the observations of SC1 and SC4. Both satellites observe two step-up structures, marked as 1a and 1b for SC1 and 4a and 4b for SC4. SC1 observes the step-up structures about 1 minute later than SC4. *Trattner et al.* [2008] calculated the convection speed of magnetic field lines by using the SuperDARN radar observations, showing that the speed of field lines matches with that of each step-up structure. Thus, these structures are temporal structures convecting poleward with the magnetic field lines.

Figure 1-8 shows the relation between temporal cusp structure and intermittent dayside reconnection. The left and right panels show the magnetopause viewed from the dusk and the mid-afternoon, respectively. The black lines are the open field lines draped over the magnetopause. The red and blue dots represent the approximate

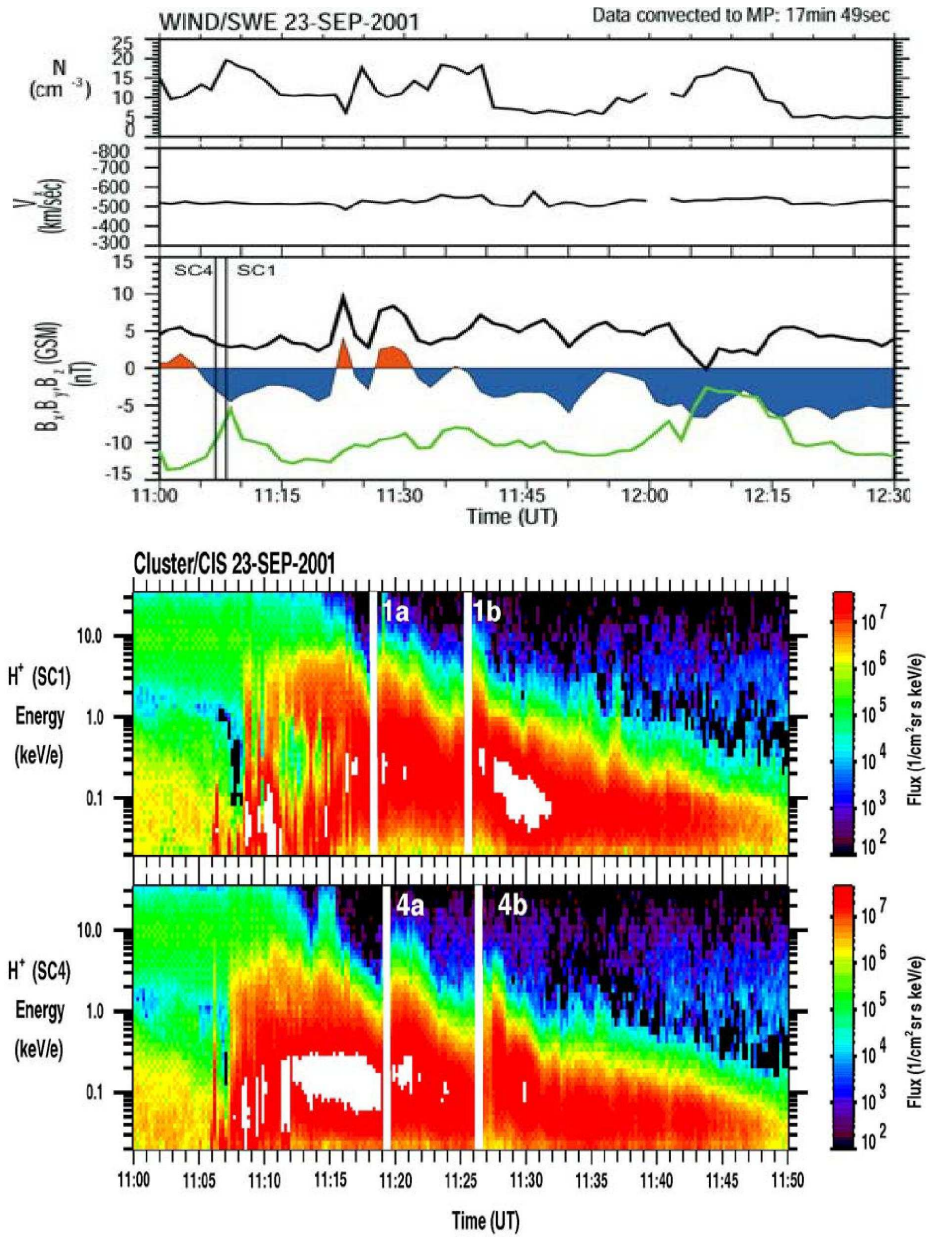

Figure 1-7: Temporal cusp ion structures observed by Cluster satellites, SC1 and SC4. (Top) Solar wind conditions observed by WIND on 23 September 2001. Number density, solar wind velocity, and IMF B_x (black line), B_y (green line), and B_z (shaded area) are plotted. The vertical black lines show when SC1 and SC4 enter the cusp. (Bottom) The energy versus time spectrograms observed by SC1 and SC4 on 23 September 2001. The two step-up structures are marked as 1a and 1b for SC1 and 4a and 4b for SC4. [*Trattner et al.*, 2008]

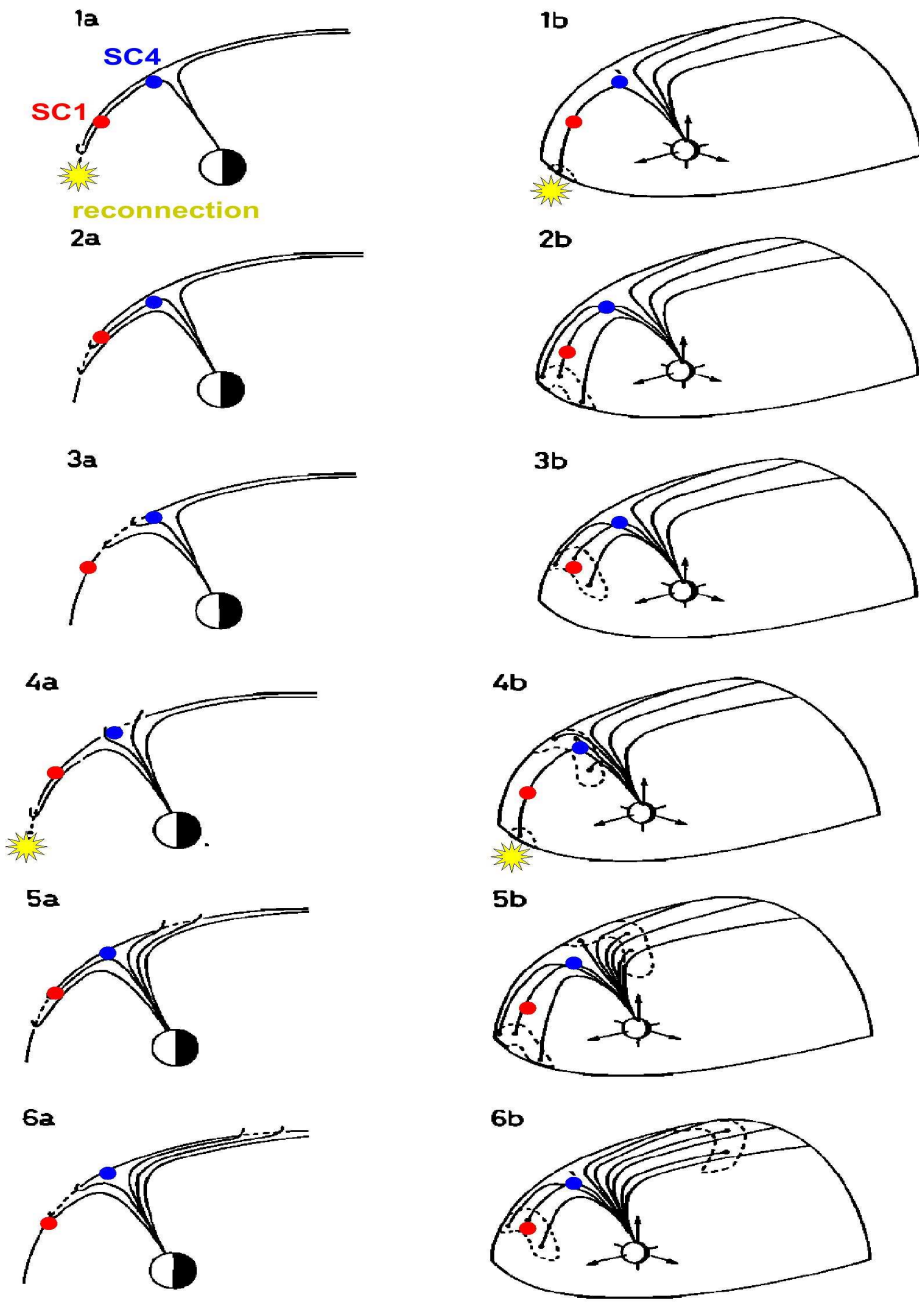

Figure 1-8: The relation between temporal cusp ion structure and intermittent subsolar reconnection. The left and right panels show the magnetopause viewed from dusk and mid-afternoon, respectively. Red and blue dots represent the approximate locations of SC1 and SC4, and yellow stars show the reconnection bursts. [modified from *Smith and Lockwood*, 1996]

locations of SC1 and SC4. The yellow stars show the reconnection burst. When reconnection happens near the subsolar region (See 1a and 1b in Figure 1-8), open field lines are created and convect poleward (2a and 2b). When these newly opened field line pass SC1 (3a and 3b), it observes the first step-up structure. The field lines continuously convect poleward and pass SC4 about 1 minute later (4a and 4b). Then, SC4 observes the first step-up structure. Meanwhile, another reconnection burst happens at the subsolar point, and the newly opened field lines convect poleward (5a and 5b). When SC1 is on these open field lines (6a and 6b), it observes the second step-up structure. SC4 also observes the second step-up structure 1 minute later when the field lines pass SC4. This is how the two step-up structures are observed by the Cluster satellites. Intermittent reconnection on the dayside magnetopause drops solar wind ions into the cusp, producing the temporal step-up structures.

To distinguish spatial cusp ion structures, two satellites need to traverse the cusp at different times. If both satellites observe similar cusp structures at different cusp crossing times, the structures are considered to be spatial structures. *Trattner et al.* [2002] have used the FAST and Polar spacecraft in order to investigate spatial cusp structures. The FAST spacecraft is on a low-altitude orbit and moves faster than the Polar spacecraft which has a high-altitude orbit. Their different orbital speeds set up good conditions for distinguishing spatial cusp structures. Consider that intermittent reconnection creates open field lines moving faster than the Polar speed and slower than the FAST speed. As new open field lines have more high-energy ions than old open field lines, Polar observes a step-up structure when the new field lines catch up with Polar. On the other hand, FAST catches up with the old field lines due to its fast speed, observing a step-down structure. Figure 1-9 shows schematic representation of this temporal structure observed by FAST and Polar. The temporal structure appears differently in their observations due to the different orbit speed. Therefore, FAST

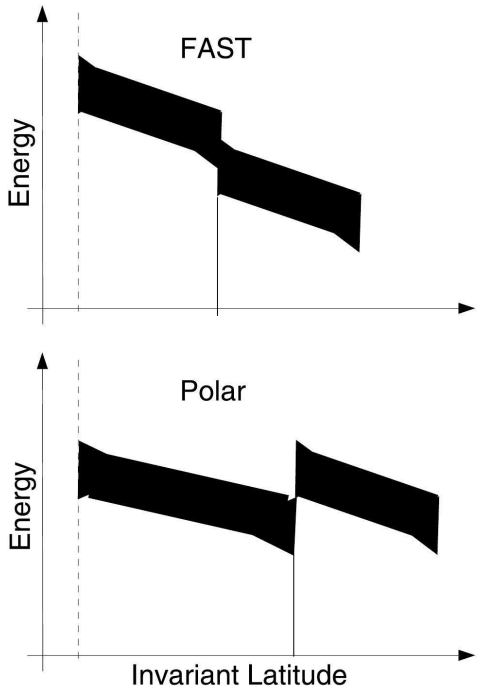

Figure 1-9: Schematic representation of a temporal structure observed by the Polar and FAST satellites. Because of their different orbital speeds, two satellites observe the same event differently. [*Trattner et al.*, 2002]

and Polar observations can distinguish spatial cusp structures easily by searching the datasets for the logical pairs.

Figure 1-10 shows one example of a spatial structure. The top panel of Figure 1-10 represents solar wind conditions observed by Wind on 25 September 1998. The number density, solar wind speed, IMF B_x (thick line), B_y (thin line), and B_z (shaded area) are plotted. The black bars in the density plot show when the FAST and Polar spacecraft reside in the cusp. During the whole cusp crossing time, the IMF is strongly southward and duskward. The bottom panel of Figure 1-10 shows the spectrograms observed by FAST and Polar. Although Polar passes the cusp about 35 minutes later than FAST, both satellites observe similar cusp structures, suggesting that the observed structure is spatial. *Trattner et al.* [2002] suggested that multiple reconnection sites cause the spatial structures. Figure 1-11 shows the schematic representation of this theory on the ionosphere. Two reconnection sites produce two different flux tubes, one near local noon and another in the dawn section. As each flux tube has a different history of field lines, a satellite observes a distinct cusp structure when it passes from one flux tube to another. Although the Polar and FAST spacecraft enter the cusp at different times, two reconnection sites consistently produce the two flux tubes, and both satellites cross the two flux regions, observing similar cusp structures. Thus, multiple reconnection sites can lead to the spatial structures.

1.4 Modeling of cusp ion structures

Investigating whether a cusp ion structure is temporal or spatial is key to understanding the temporal versus spatial nature of dayside reconnection. Consequently, for this investigation, at least two satellites need to be in the cusp in order to avoid temporal and spatial ambiguities. Under this limitation, models of cusp ion structures have

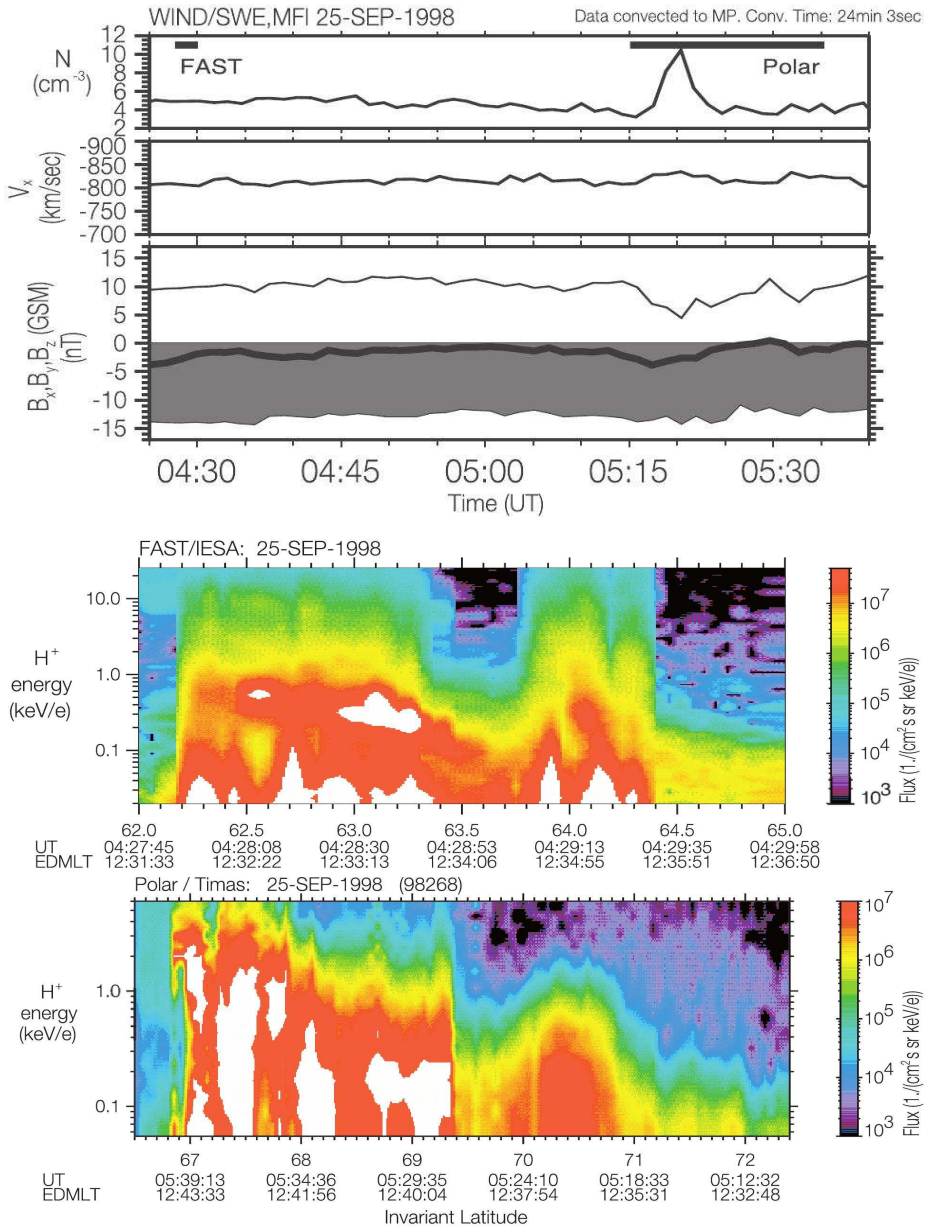

Figure 1-10: Spatial cusp ion structure observed by the FAST and Polar satellites. (Top) Solar wind conditions observed by Wind on 25 September 1998. Number density, velocity, IMF B_x (thick line), B_y (thin line), and B_z (a shaded area) are plotted. (Bottom) Comparison of FAST and Polar omni-directional flux measurements. [*Trattner et al.*, 2002]

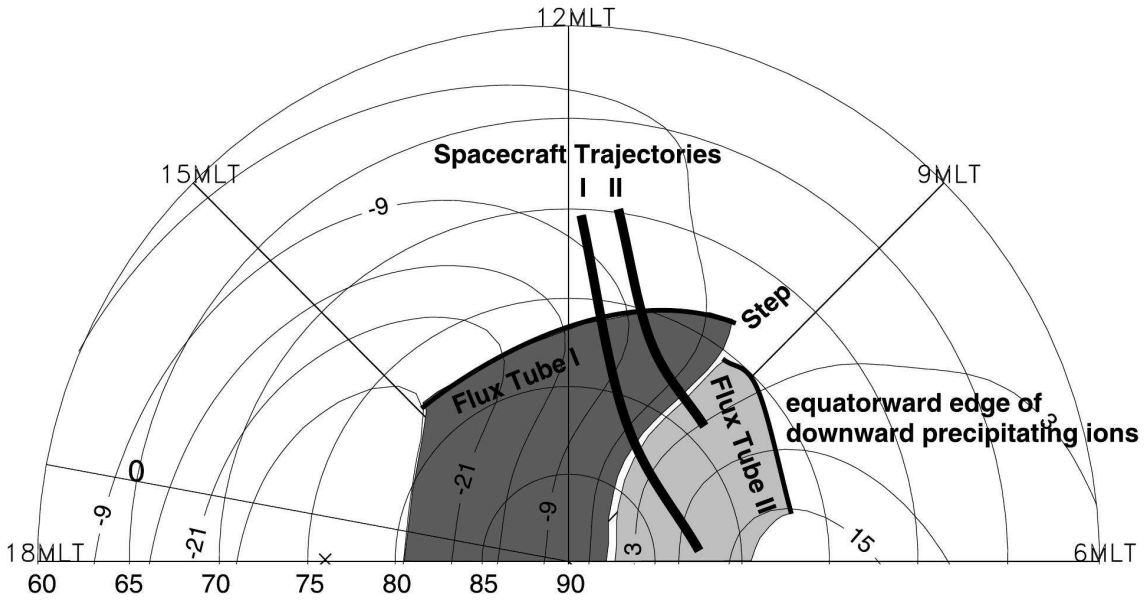

Figure 1-11: The relation between spatial structure and multiple reconnection sites. [*Trattner et al.*, 2002]

been developed as a tool for understanding the relation between cusp ion structure and dayside reconnection. In this section, we introduce these modeling approaches.

Onsager et al. [1995] introduces the first model of cusp ion structures by using three steps. First, the model traces test particles backward in time from the satellite location inside the cusp to the magnetopause. Onsager's model tracks the guiding center of these particles by integrating the parallel equation of motion with magnetic fields obtained from the Stern empirical model [*Stern et al.*, 1985] and simple dawn-dusk electric fields. Second, the model estimates particle acceleration at the magnetopause crossing, and uses this information to calculate particle velocities in the magnetosheath. Last, the model calculates phase-space densities of these particles with the particle velocities in the magnetosheath and the distribution function of the magnetosheath. By assuming that the magnetosheath plasma follows Maxwell distributions, *Onsager et al.* [1995] calculate the distribution function by using den-

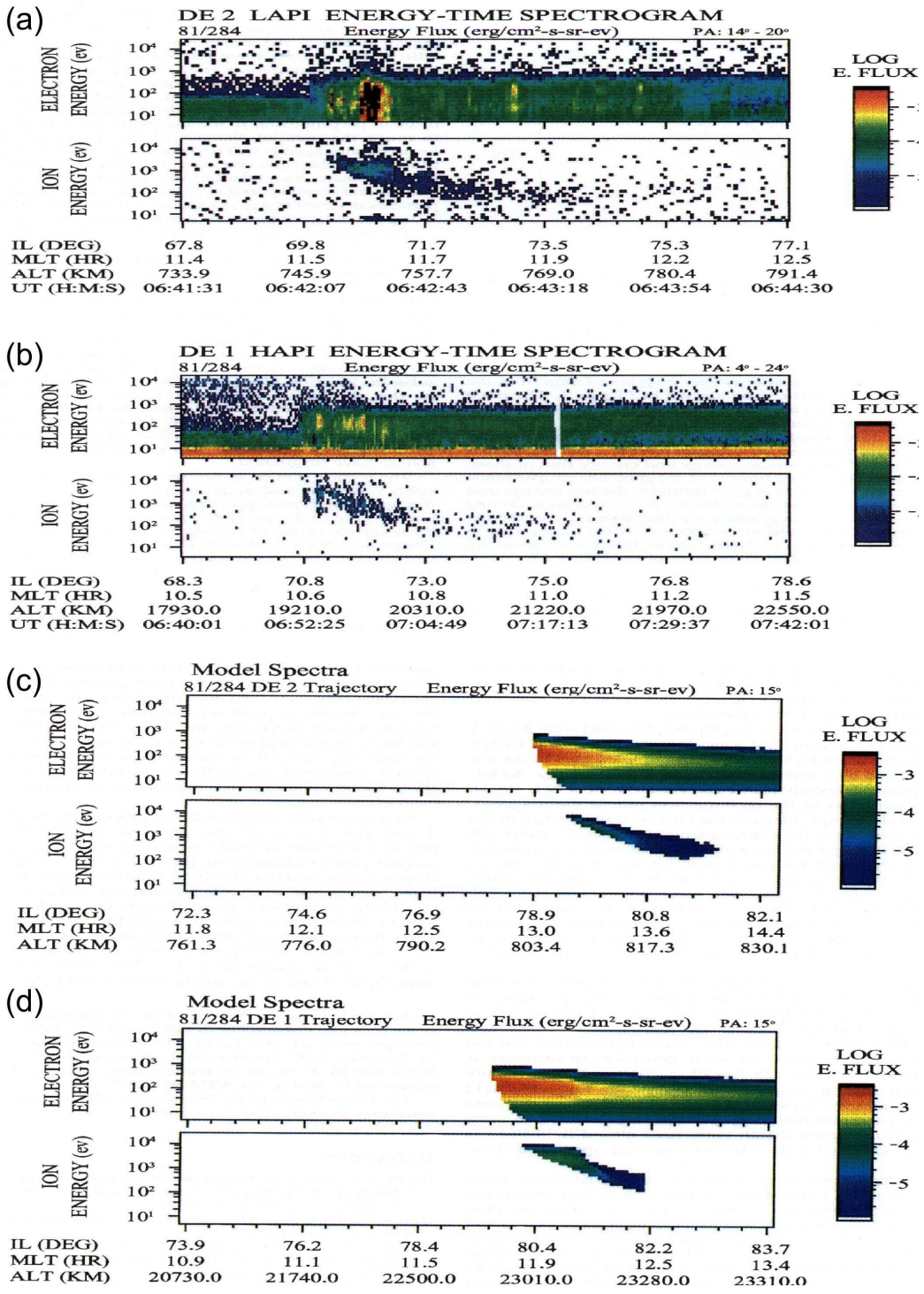

Figure 1-12: Comparison of Onsager's model results with the satellite observations. (a),(b) : the energy versus time spectrogram observed by DE2 and DE1. (c),(d) : the model results for DE2 and DE1 observations. [*Onsager et al.*, 1995]

sity, bulk speed, and temperature estimated from the gas dynamic results of *Spreiter and Stahara* [1985]. Additionally, the model assumes no collision along the particle trajectories, and therefore, by Liouville's theorem, the phase-space densities are conserved along particle trajectories. The densities calculated at the magnetosheath are used for the energy-time spectrogram, constructing cusp ion structures.

Onsager et al. [1995] reconstruct the normal dispersion observed by the two conjugate Dynamic Explorers, DE1 and DE2. DE1 passes the cusp about 10 minutes after DE2. In spite of the different cusp crossing times, they observe similar structures, indicating the spatial nature of this structure. Figure 1-12 (a) and (b) show the normal dispersion observed by DE2 and DE1, and (c) and (d) shows the modeled spectrograms. Onsager's model reproduces key features of the satellite observations, demonstrating that the modeling technique is applicable to study cusp ion structures.

Motivated by *Onsager et al.* [1995], *Wing et al.* [2001] develop an improved model of cusp ion structures whose basic approach is the same as Onsager's method. First, Wing's model traces the guiding centers of cusp particles backward in time until the particles reach the magnetopause. This model uses a more advanced empirical electromagnetic field model composed of the T96 magnetic field model [*Tsyganenko and Stern*, 1996] and the electric field model obtained from statistical APL convection patterns [*Rhuhoniemi and Greenwald*, 1996]. After calculating particle acceleration at the magnetopause, Wing's model determines the phase-space densities of test particles based on their velocity in the magnetosheath and the magnetosheath plasma distribution. Unlike Onsager's model that uses a Maxwellian distribution, Wing's model uses a Kappa distribution since satellite observations have revealed that superthermal magnetosheath ions follow a power law distribution. Acceleration or diffusion processes causing this kappa distribution are not well understood. Finally, Wing's model uses phase-space densities calculated in the magnetosheath to construct cusp

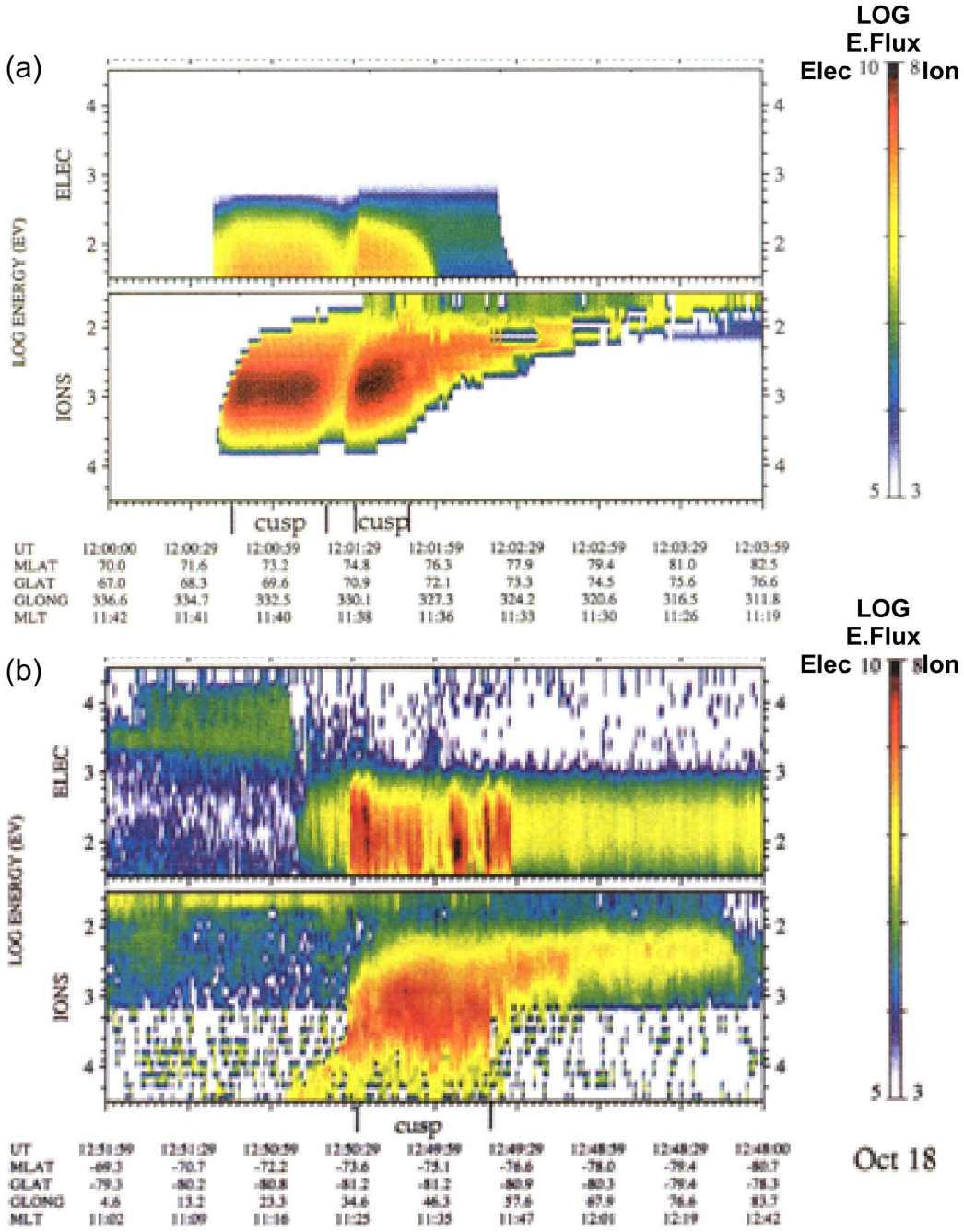

Figure 1-13: Comparison of Wing's model result with the satellite observation. (a) The double dispersion expected by Wing's model during strongly duskward and weakly southward IMF. (b) The double dispersion observed by the DMSP satellite during the similar IMF condition. [*Wing et al.*, 2001]

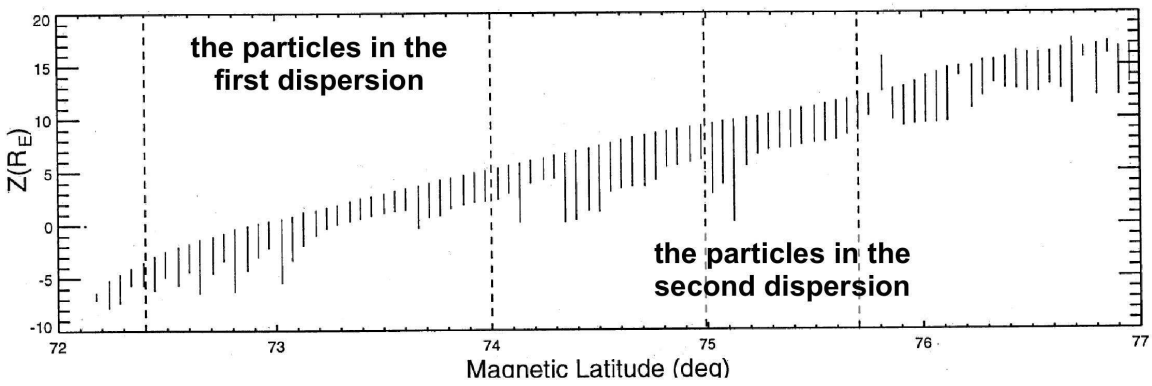

Figure 1-14: The Z_{gse} coordinate of the ion entry points on the magnetopause. The X axis is the magnetic latitude where particles precipitate. [modified from *Wing et al.*, 2001]

ion structures by assuming that the densities are conserved along the trajectories. The main difference between the two models of Wing and Onsager is that the former uses a more advanced empirical model for the particle tracer and more realistic magnetosheath plasma distribution for a phase-space density calculation.

Wing et al. [2001] predict double dispersions during weakly southward and strongly duskward IMF by using their improved model of cusp ion structures. They confirm the model predictions by showing that 70 percent of cusp ion structures observed by DMSP satellites during similar IMF conditions are double dispersions. Figure 1-13 (a) and (b) show the predicted and observed double dispersions. The dispersion at low latitude is less sloped than the one at high latitude. To understand the reconnection mechanism that produces double dispersions, *Wing et al.* [2001] examine where the test ions penetrate the magnetopause. Figure 1-14 shows the Z component of the ion entry points on the magnetopause. Ions producing the first dispersion originate from the lower latitudes of the magnetopause while ions producing the second dispersion come from the higher latitudes. This implies that two reconnection sites exist on the

low and high latitudes of the magnetopause, producing double dispersions.

The previous models by Onsager and Wing have demonstrated their ability to construct cusp structures and have inferred the dayside reconnection properties. However, the models use static empirical electromagnetic field models, and therefore their studies are limited only to spatial cusp structures during constant solar wind conditions. To study temporal cusp structures during non-steady solar wind conditions, a new, dynamic model of cusp ion structure is necessary.

1.5 Introduction to our research

In this dissertation, we develop a new model of cusp ion structures that is also valid for dynamic solar wind and IMF conditions. Our model uses the Liouville Theorem Particle Tracer (LTPT) together with the OpenGGCM three-dimensional global magnetosphere-ionosphere MHD model. The LTPT conducts a full particle tracing by integrating the Lorentz equation and the equation of motion. It traces cusp ions backward in time from the cusp to the magnetosheath. Then it calculates the phase-space densities of cusp ions based on their velocity information and the velocity distribution in the magnetosheath, employing Liouville's theorem. OpenGGCM solves resistive MHD equations with SW/IMF input from ACE or Wind, and provides time-dependent electromagnetic fields for the LTPT as well as number density, velocity, and plasma pressure. A major difference between our model and the previous models of Onsager and Wing is that the ions move freely in 3D space by interacting with time-dependent electromagnetic fields under various SW/IMF conditions.

We introduce the details of our OpenGGCM-LTPT model in chapter 2. Then, in chapter 3, we verify our model's validity by reproducing cusp ion structures observed from three cusp-crossing events of Cluster and Polar satellites. We also demonstrate that our model can distinguish between the temporal and spatial nature of cusp

ion structures, and can investigate the magnetopause processes that lead to these structures. After this model validation test, we study the general relation between cusp ion structures and magnetopause processes during four IMF clock angles of 0°, 60°, 120°, and 180°. Chapter 4 covers this study. Finally, in chapter 5, we summarize our results.

Chapter 2

Model of cusp ion structures

In this chapter, we introduce our new model of cusp ion structures which is composed of the OpenGGCM global MHD model and the Liouville Theorem Particle Tracer (LTPT). Previous models by Onsager and Wing trace cusp ions back to the magnetosheath by using empirical electromagnetic field models, and therefore their studies are limited to only cusp structures during constant solar wind conditions. Conversely, our model uses the OpenGGCM global MHD model which provides time dependent electromagnetic fields, and can therefore expand the study of cusp ion structures even for dynamic solar wind conditions. In this chapter, we first introduce the general concepts of magnetohydrodynamics, and then discuss the OpenGGCM model and the LTPT code. Finally, we briefly summarize the methodology of our OpenGGCM-LTPT model.

2.1 Magnetohydrodynamics (MHD)

Magnetohydrodynamics is a branch of science that describes dynamics of electronically conducting fluids in a magnetic field. A moving conductive fluid induces currents, modifying a magnetic field which in turn changes the fluid movement. MHD explains this coupled system by using the fluid equations and Maxwell's equations. This MHD approach is often used for understanding motion of a space plasma, an ionized gas composed of electrons and ions. The Earth's magnetosphere is one of the

research areas that uses the MHD approach. With advanced computing technologies, scientists can develop three-dimensional global MHD models such as OpenGGCM, BATSRUS, GUMICS, etc., and use them as a tool to understand various geomagnetic events inside the Earth's magnetosphere. In this section, we will derive MHD equations that these models are based on.

2.1.1 One-fluid theory

Vlasov equation

Plasmas contain electrons and ions with approximately equal charge densities. The ions can be protons, He^{2+}, O^{+}, etc. Plasmas of each species are described by distribution functions $f_s(\mathbf{r}, \mathbf{v}, t)$ where s represents the particle species, $\mathbf{r}$ is the position vector (x, y, z), $\mathbf{v}$ is the velocity vector (v_x, v_y, v_z) , and t is the time scalar. $\mathbf{r}$, $\mathbf{v}$, and t are called phase space coordinates and they are independent of each other. The number of type s particles per unit volume dV at time t can be expressed:

$$f_s(\mathbf{r}, \mathbf{v}, t)dV = f_s d\mathbf{r} d\mathbf{v} \tag{2.1}$$

$$= f_s dx dy dz dv_x dv_y dv_z. \tag{2.2}$$

To express the time variation of a type s plasma, the total time derivative of the distribution function becomes:

$$\frac{df_s(\mathbf{r}, \mathbf{v}, t)}{dt} = \frac{\partial f_s}{\partial t} + \frac{\partial f_s}{\partial x}\frac{dx}{dt} + \frac{\partial f_s}{\partial y}\frac{dy}{dt} + \frac{\partial f_s}{\partial z}\frac{dz}{dt} + \frac{\partial f_s}{\partial v_x}\frac{dv_x}{dt} + \frac{\partial f_s}{\partial v_y}\frac{dv_y}{dt} + \frac{\partial f_s}{\partial v_z}\frac{dv_z}{dt} \tag{2.3}$$

$$= \frac{\partial f_s}{\partial t} + v_x\frac{\partial f_s}{\partial x} + v_y\frac{\partial f_s}{\partial y} + v_z\frac{\partial f_s}{\partial z} + a_x\frac{\partial f_s}{\partial v_x} + a_y\frac{\partial f_s}{\partial v_y} + a_z\frac{\partial f_s}{\partial v_z} \tag{2.4}$$

$$= \frac{\partial f_s}{\partial t} + \mathbf{v}\cdot\nabla_{\mathbf{r}} f_s + \mathbf{a}\cdot\nabla_{\mathbf{v}} f_s \tag{2.5}$$

where $\nabla_{\mathbf{v}} = \frac{\partial}{\partial v_x} + \frac{\partial}{\partial v_y} + \frac{\partial}{\partial v_z}$. If the plasma is collisionless, the time derivative of the distribution function is zero. Then, the above equation becomes the Vlasov equation:

$$\frac{df_s(\mathbf{r}, \mathbf{v}, t)}{dt} = \frac{\partial f_s}{\partial t} + \mathbf{v}\cdot\nabla_{\mathbf{r}} f_s + \mathbf{a}\cdot\nabla_{\mathbf{v}} f_s = 0. \tag{2.6}$$

The collision frequencies of solar wind plasma and magnetospheric plasma are very small, approximately $10^{-4}/s$ and $10^{-8}/s$, respectively. The assumption that plasma is collisionless is, therefore, a reasonable approach.

The acceleration **a** is affected by non-collisional forces such as gravity and the electromagnetic force. Gravity can be neglected because of its small value. Then, the Vlasov equation becomes:

$$\frac{df_s(\mathbf{r},\mathbf{v},t)}{dt} = \frac{\partial f_s}{\partial t} + \mathbf{v}\cdot\nabla_{\mathbf{r}} f_s + \frac{q_s}{m_s}(\mathbf{E}+\mathbf{v}\times\mathbf{B})\cdot\nabla_{\mathbf{v}} f_s = 0. \tag{2.7}$$

where q_s is the electrical charge of type s particle, m_s is its mass, **E** is electric field, and **B** is magnetic field. Maxwell's equations can be used to determine **E** and **B**.

Macroscopic plasma parameters

Since the distribution function is often complicated, it is useful to define the macroscopic plasma parameters such as density and average velocity for a better understanding of the average behavior of a plasma. The macroscopic parameters are defined by the first few velocity moments of the distribution function:

$$M_s^i(\mathbf{r},t) = \int f_s(\mathbf{r},\mathbf{v},t)\mathbf{v}^i d\mathbf{v} \tag{2.8}$$

where $i = 0, 1, 2, 3$. The number density of particle species s is given by the zeroth $(i = 0)$ moment:

$$n_s = \int f_s d\mathbf{v}. \tag{2.9}$$

The average velocity $\mathbf{u}_s$ is defined from the first moment:

$$\mathbf{u}_s = \frac{1}{n_s}\int \mathbf{v} f_s d\mathbf{v}. \tag{2.10}$$

The second moment of the distribution function is related to the pressure tensor:

$$\tilde{\mathrm{P}}_s = m_s \int (\mathbf{v}-\mathbf{u}_s)(\mathbf{v}-\mathbf{u}_s) f_s d\mathbf{v}. \tag{2.11}$$

This represents the momentum flux in the frame of reference which moves at a velocity $\mathbf{u}_s$. For an isotropic plasma pressure, the off-diagonal terms of $\tilde{\mathrm{P}}_s$ that describe shear stresses vanish and only the diagonal terms are left. Then, the pressure can be simplified to:

$$\mathrm{p}_s = \frac{m_s}{3}\int(\mathbf{v}-\mathbf{u}_s)\cdot(\mathbf{v}-\mathbf{u}_s)f_s d\mathbf{v} \tag{2.12}$$

which is the trace of the pressure tensor. The internal kinetic energy, ε_s is also defined from the second moment:

$$\varepsilon_s = \int \frac{1}{2}m(v-u_s)^2 f_s d\mathbf{v}. \tag{2.13}$$

The next higher moment is called the heat flux tensor:

$$\tilde{\mathrm{Q}}_s = m_s\int(\mathbf{v}-\mathbf{u}_s)(\mathbf{v}-\mathbf{u}_s)(\mathbf{v}-\mathbf{u}_s)f_s d\mathbf{v}. \tag{2.14}$$

By taking the trace of the heat flux tensor, we obtain the heat flux vector:

$$\tilde{\mathrm{q}}_s = \frac{m_s}{2}\int(\mathbf{v}-\mathbf{u}_s)\cdot(\mathbf{v}-\mathbf{u}_s)(\mathbf{v}-\mathbf{u}_s)f_s d\mathbf{v} \tag{2.15}$$

which describes the flux of internal kinetic energy.

The mass density ρ_{ms}, charge density ρ_{qs}, and current density J_s can be calculated by using the average number density n_s and the average velocity $\mathbf{u}_s$:

$$\rho_{ms} = m_s n_s, \quad \rho_m = \sum_s \rho_{ms} \tag{2.16}$$

$$\rho_{qs} = q_s n_s, \quad \rho_q = \sum_s \rho_{qs} \tag{2.17}$$

$$\mathbf{J}_s = q_s n_s \mathbf{u}_s, \quad \mathbf{J} = \sum_s \mathbf{J}_s. \tag{2.18}$$

where m_s and q_s are the mass and electrical charge of type s particle.

Macroscopic plasma equations

As with macroscopic plasma parameters, we can obtain macroscopic plasma equations by taking the velocity moments of the Vlasov equation. These macroscopic equations are helpful to understand the average behavior of plasma motion.

To obtain the zeroth order moment, we integrate the Vlasov equation over velocity space:

$$\int \frac{\partial f_s}{\partial t} d\mathbf{v} + \int \mathbf{v} \cdot \nabla_{\mathbf{r}} f_s d\mathbf{v} + \int \frac{q_s}{m_s} (\mathbf{E} + \mathbf{v} \times \mathbf{B}) \cdot \nabla_{\mathbf{v}} f_s d\mathbf{v} = 0. \tag{2.19}$$

The time derivative in the first term can be interchanged with the integral since the velocity space, $d\mathbf{v}$, is not dependent on time, t. Thus, the first term becomes:

$$\int \frac{\partial f_s}{\partial t} d\mathbf{v} = \frac{\partial}{\partial t} \int f_s d\mathbf{v} = \frac{\partial n_s}{\partial t}. \tag{2.20}$$

From $\nabla \cdot (\Phi \mathbf{F}) = \mathbf{F} \cdot \nabla \Phi + \Phi \nabla \cdot \mathbf{F}$, the second term becomes:

$$\int \mathbf{v} \cdot \nabla_{\mathbf{r}} f_s d\mathbf{v} = \int \left\{ \nabla_{\mathbf{r}} \cdot (\mathbf{v} f_s) - f_s \nabla_{\mathbf{r}} \cdot \mathbf{v} \right\} d\mathbf{v} \tag{2.21}$$

$$= \nabla_{\mathbf{r}} \cdot \int \mathbf{v} f_s d\mathbf{v} - \int f_s \nabla_{\mathbf{r}} \cdot \mathbf{v} d\mathbf{v} \tag{2.22}$$

$$= \nabla \cdot (n_s \mathbf{u}_s). \tag{2.23}$$

Since the space and velocity coordinates are independent to each other, the differential, $\nabla_{\mathbf{r}}$, can be interchanged with the integral over velocity, $d\mathbf{v}$, in the first term of equation (2.22). For the same reason, $\nabla_{\mathbf{r}} \cdot \mathbf{v}$ in the second term is zero. Applying the same vector calculus identity used in equation (2.21), the last term of equation (2.19) becomes:

$$\int \frac{q_s}{m_s} (\mathbf{E} + \mathbf{v} \times \mathbf{B}) \cdot \nabla_{\mathbf{v}} f_s d\mathbf{v}$$

$$= \frac{q_s}{m_s} \int \nabla_{\mathbf{v}} \cdot \left\{ f_s (\mathbf{E} + \mathbf{v} \times \mathbf{B}) \right\} d\mathbf{v} - \frac{q_s}{m_s} \int f_s \nabla_{\mathbf{v}} \cdot (\mathbf{E} + \mathbf{v} \times \mathbf{B}) d\mathbf{v} \tag{2.24}$$

$$= \frac{q_s}{m_s} \int f_s (\mathbf{E} + \mathbf{v} \times \mathbf{B}) \cdot d\mathbf{S} - \frac{q_s}{m_s} \int f_s \nabla_{\mathbf{v}} \cdot \mathbf{E} d\mathbf{v} - \frac{q_s}{m_s} \int f_s \nabla_{\mathbf{v}} \cdot (\mathbf{v} \times \mathbf{B}) d\mathbf{v} \tag{2.25}$$

$$= 0.$$

To obtain the first term of equation (2.25), we used the divergence theorem:

$$\int (\nabla \cdot \mathbf{F}) dV = \int (\mathbf{F} \cdot \mathbf{n}) dS = \int \mathbf{F} \cdot d\mathbf{S} \tag{2.26}$$

where V is a volume in 3D space, $\mathbf{S}$ is the boundary of the volume V, and $\mathbf{n}$ is the normal vector to the boundary S. Since f_s becomes zero at the boundary S where $v = \infty$, the first term of equation (2.25) becomes zero. The second term also becomes zero since $\mathbf{E}$ does not depend on $\mathbf{v}$. From $\nabla \cdot (\mathbf{F} \times \mathbf{G}) = (\nabla \times \mathbf{F}) \cdot \mathbf{G} - (\nabla \times \mathbf{G}) \cdot \mathbf{F}$, the third term is:

$$-\frac{q_s}{m_s} \int f_s \nabla_{\mathbf{v}} \cdot (\mathbf{v} \times \mathbf{B}) d\mathbf{v}$$
$$= -\frac{q_s}{m_s} \int f_s (\nabla_{\mathbf{v}} \times \mathbf{v}) \cdot \mathbf{B} d\mathbf{v} + \frac{q_s}{m_s} \int f_s (\nabla_{\mathbf{v}} \times \mathbf{B}) \cdot \mathbf{v} d\mathbf{v} = 0. \tag{2.27}$$

$\nabla_{\mathbf{v}} \times \mathbf{v}$ in the first term is zero, and the second term becomes zero because there is no dependence of $\mathbf{B}$ on $\mathbf{v}$. By combining the remaining terms, equation (2.19) becomes:

$$\boxed{\frac{\partial n_s}{\partial t} + \nabla_{\mathbf{r}} \cdot (n_s \mathbf{u}_s) = 0.} \tag{2.28}$$

This is the continuity equation which describes the conservation of number density. The time variation of number density (n_s) per unit volume is balanced with the net gain or loss by the number density flux ($n_s \mathbf{v_s}$) crossing the unit volume. This continuity equation also describes conservation of mass density and charge density. By multiplying the mass, m_s, and charge, q_s, to equation (2.28), we obtain the mass and charge continuity equations:

$$\frac{\partial \rho_{ms}}{\partial t} + \nabla_{\mathbf{r}} \cdot (\rho_{ms} \mathbf{u}_s) = 0 \tag{2.29}$$
$$\frac{\partial \rho_{qs}}{\partial t} + \nabla_{\mathbf{r}} \cdot (\rho_{qs} \mathbf{u}_s) = 0. \tag{2.30}$$

To obtain the second moment of the Vlasov equation, we multiply the velocity vector $\mathbf{v}$ into the Vlasov equation and integrate that over velocity space:

$$\int \mathbf{v} \frac{\partial f_s}{\partial t} d\mathbf{v} + \int \mathbf{v} (\mathbf{v} \cdot \nabla_{\mathbf{r}} f_s) d\mathbf{v} + \frac{q_s}{m_s} \int \mathbf{v} (\mathbf{E} + \mathbf{v} \times \mathbf{B}) \cdot \nabla_{\mathbf{v}} f_s d\mathbf{v} = 0. \tag{2.31}$$

Since $\mathbf{v}$ and t are independent coordinates, the first term becomes:

$$\int \mathbf{v} \frac{\partial f_s}{\partial t} d\mathbf{v} = \frac{\partial}{\partial t} \int \mathbf{v} f_s d\mathbf{v} = \frac{\partial (n_s \mathbf{u}_s)}{\partial t}. \tag{2.32}$$

The second term becomes more difficult with dyadic algebra:

$$\int \mathbf{v}(\mathbf{v}\cdot\nabla_{\mathbf{r}} f_s)d\mathbf{v} = \nabla_{\mathbf{r}}\cdot\int \mathbf{v}\mathbf{v} f_s d\mathbf{v} \tag{2.33}$$

$$= \nabla_{\mathbf{r}}\cdot\int \{(\mathbf{v}-\mathbf{u}_s)(\mathbf{v}-\mathbf{u}_s) - \mathbf{u}_s\mathbf{u}_s + \mathbf{v}\mathbf{u}_s + \mathbf{u}_s\mathbf{v}\} f_s d\mathbf{v} \tag{2.34}$$

$$= \nabla_{\mathbf{r}}\cdot\frac{\tilde{\mathrm{P}}_s}{m_s} + \nabla_{\mathbf{r}}\cdot(n_s\mathbf{u}_s\mathbf{u}_s). \tag{2.35}$$

As $\mathbf{r}$ and $\mathbf{v}$ are independent, the operator $\nabla_{\mathbf{r}}$ in (2.33) is extracted out of the integral. Equations (2.10) and (2.11) are also used in the derivation of equation (2.35). The last term of equation (2.31) is:

$$\frac{q_s}{m_s}\int \mathbf{v}(\mathbf{E}+\mathbf{v}\times\mathbf{B})\cdot\nabla_{\mathbf{v}} f_s d\mathbf{v}$$

$$= \frac{q_s}{m_s}\int \nabla_{\mathbf{v}}\cdot\{\mathbf{v}(\mathbf{E}+\mathbf{v}\times\mathbf{B}) f_s\}\, d\mathbf{v} - \frac{q_s}{m_s}\int \nabla_{\mathbf{v}}\cdot\{\mathbf{v}(\mathbf{E}+\mathbf{v}\times\mathbf{B})\}\, f_s d\mathbf{v} \tag{2.36}$$

$$= \frac{q_s}{m_s}\int f_s\mathbf{v}(\mathbf{E}+\mathbf{v}\times\mathbf{B})\cdot d\mathbf{S} - \frac{q_s}{m_s}\int (\mathbf{E}+\mathbf{v}\times\mathbf{B}) f_s d\mathbf{v} \tag{2.37}$$

$$= -\frac{n_s q_s}{m_s}(\mathbf{E}+\mathbf{u}_s\times\mathbf{B}). \tag{2.38}$$

The first term in equation (2.37) becomes zero since $f_s \to 0$ as $\mathbf{v}\to\infty$. Finally, equation (2.31) reduces to:

$$\frac{\partial(n_s\mathbf{u}_s)}{\partial t} + \nabla_{\mathbf{r}}\cdot(n_s\mathbf{u}_s\mathbf{u}_s) + \nabla_{\mathbf{r}}\cdot\frac{\tilde{\mathrm{P}}_s}{m_s} - \frac{q_s}{m_s}(\mathbf{E}+\mathbf{u}_s\times\mathbf{B}) = 0 \tag{2.39}$$

or

$$\frac{\partial(\rho_{ms}\mathbf{u}_s)}{\partial t} + \nabla_{\mathbf{r}}\cdot(\rho_{ms}\mathbf{u}_s\mathbf{u}_s) + \nabla_{\mathbf{r}}\cdot\tilde{\mathrm{P}}_s - \rho_{qs}\mathbf{E} - \mathbf{J}_s\times\mathbf{B} = 0. \tag{2.40}$$

This describes conservation of momentum, and therefore is called the momentum equation. Note that each of the moment equations is linked to the next higher moment equation. The continuity equation relates time variation of density to the divergence of the number density flux. The momentum equation defining the flux invokes pressure gradient, which is obtained from the third velocity moment of the Vlasov

equation. In this manner, an infinite hierarchy of moment equations can be developed. We must close this system of equations to understand plasma behaviors to a reasonable extent. Scientists often solve this problem by assuming isotropic plasma pressures, i.e., $\tilde{\mathrm{P}}_s = \mathrm{p}_s\mathbf{I}$. Then, the momentum equation is written as:

$$\boxed{\frac{\partial(\rho_{ms}\mathbf{u}_s)}{\partial t} + \nabla_{\mathbf{r}} \cdot (\mathrm{p}_s\mathbf{I} + \rho_{ms}\mathbf{u}_s\mathbf{u}_s) - \rho_{qs}\mathbf{E} - \mathbf{J}_s \times \mathbf{B} = 0.} \tag{2.41}$$

The third velocity moment of the Vlasov equation describes energy conservation, linking the pressure tensor, $\tilde{\mathrm{P}}_s$, to the heat flux tensor, $\tilde{\mathrm{Q}}_s$. High-rank tensors are very complicated and it is hard to understand their physical meaning. Therefore, we multiply v^2 instead of $\mathbf{vv}$ into the Vlasov equation, and integrate it over velocity space:

$$\int v^2 \frac{\partial f_s}{\partial t} d\mathbf{v} + \int v^2 (\mathbf{v} \cdot \nabla_{\mathbf{r}} f_s) d\mathbf{v} + \frac{q_s}{m_s} \int v^2 (\mathbf{E} + \mathbf{v} \times \mathbf{B}) \cdot \nabla_{\mathbf{v}} f_s d\mathbf{v} = 0. \tag{2.42}$$

The partial derivative, $\frac{\partial}{\partial t}$, in the first term can be extracted out of the integral because of its independence on $\mathbf{v}$. Therefore, the first term becomes:

$$\begin{aligned}
\int v^2 \frac{\partial f_s}{\partial t} d\mathbf{v} &= \frac{\partial}{\partial t} \int v^2 f_s d\mathbf{v} && (2.43)\\
&= \frac{\partial}{\partial t} \int \left\{ (v - u_s)^2 + 2vu_s - u_s^2 \right\} f_s d\mathbf{v} && (2.44)\\
&= \frac{\partial}{\partial t} \left\{ \int (\mathbf{v} - \mathbf{u}_s) \cdot (\mathbf{v} - \mathbf{u}_s) f_s d\mathbf{v} + \int (2vu_s - u_s^2) f_s d\mathbf{v} \right\} && (2.45)\\
&= \frac{\partial}{\partial t} \left(\frac{3\mathrm{p}_s}{m_s} + n_s u_s^2 \right) && (2.46)
\end{aligned}$$

where equation (2.12) is used. The second term of equation (2.42) becomes:

$$\begin{aligned}
\int v^2 (\mathbf{v} \cdot \nabla_{\mathbf{r}} f_s) d\mathbf{v} &= \int v^2 \left\{ \nabla_{\mathbf{r}} \cdot (\mathbf{v} f_s) - f_s (\nabla_{\mathbf{r}} \cdot \mathbf{v}) \right\} d\mathbf{v} && (2.47)\\
&= \nabla_{\mathbf{r}} \cdot \int v^2 \mathbf{v} f_s d\mathbf{v}. && (2.48)
\end{aligned}$$

Since $\mathbf{r}$ and $\mathbf{v}$ are independent variables, the second term in equation (2.47) becomes zero and the operator $\nabla_{\mathbf{r}}$ comes out of integration as shown in equation (2.48). The

v^2 term can be expressed as the vector dot product, $\mathbf{v}\cdot\mathbf{v}$. Therefore, $v^2\mathbf{v} = (\mathbf{v}\cdot\mathbf{v})\mathbf{v}$. If we express equation (2.48) as a function of $\mathbf{v}-\mathbf{u}_s$:

$$\nabla_{\mathbf{r}}\cdot\int v^2\mathbf{v}f_s d\mathbf{v} = \nabla_{\mathbf{r}}\cdot\int(\mathbf{v}\cdot\mathbf{v})\mathbf{v}f_s d\mathbf{v} \tag{2.49}$$

$$= \nabla_{\mathbf{r}}\cdot\int(\mathbf{v}-\mathbf{u}_s)\cdot(\mathbf{v}-\mathbf{u}_s)(\mathbf{v}-\mathbf{u}_s)f_s d\mathbf{v} + \nabla_{\mathbf{r}}\cdot\int(\mathbf{v}-\mathbf{u}_s)\cdot(\mathbf{v}-\mathbf{u}_s)\mathbf{u}_s f_s d\mathbf{v}$$

$$- \nabla_{\mathbf{r}}\cdot\int u_s^2\mathbf{v}f_s d\mathbf{v} + \nabla_{\mathbf{r}}\cdot\int 2(\mathbf{v}\cdot\mathbf{u}_s)\mathbf{v}f_s d\mathbf{v} \tag{2.50}$$

$$= \nabla_{\mathbf{r}}\cdot\left\{\frac{2\tilde{\mathrm{q}}_s}{m_s} + \frac{3\mathrm{p}_s}{m_s}\mathbf{u}_s - n_s u_s^2\mathbf{u}_s + 2\mathbf{u}_s\cdot\int\mathbf{v}\mathbf{v}f_s d\mathbf{v}\right\} \tag{2.51}$$

where equations (2.10), (2.12) and (2.15) are used to obtain $\mathbf{u}_s$, p_s, and $\tilde{\mathrm{q}}_s$. From equation (2.35), the last term in equation (2.51) becomes:

$$2\mathbf{u}_s\cdot\left(\frac{\tilde{\mathrm{P}}_s}{m_s} + n_s\mathbf{u}_s\mathbf{u}_s\right) = 2\mathbf{u}_s\cdot\left(\frac{\tilde{\mathrm{P}}_s}{m_s} + n_s\mathbf{u}_s\mathbf{u}_s\right) \tag{2.52}$$

$$= 2\mathbf{u}_s\cdot\frac{\tilde{\mathrm{P}}_s}{m_s} + 2n_s u_s^2\mathbf{u}_s. \tag{2.53}$$

Therefore, the second term in equation (2.42) becomes:

$$\int v^2(\mathbf{v}\cdot\nabla_{\mathbf{r}}f_s)d\mathbf{v} = \nabla_{\mathbf{r}}\cdot\left\{\frac{2\tilde{\mathrm{q}}_s}{m_s} + \frac{3\mathrm{p}_s}{m_s}\mathbf{u}_s + n_s u_s^2\mathbf{u}_s + 2\mathbf{u}_s\cdot\frac{\tilde{\mathrm{P}}_s}{m_s}\right\}. \tag{2.54}$$

The third term in equation (2.42) is:

$$\frac{q_s}{m_s}\int v^2(\mathbf{E}+\mathbf{v}\times\mathbf{B})\cdot\nabla_{\mathbf{v}}f_s d\mathbf{v}$$

$$= \frac{q_s}{m_s}\int\nabla_{\mathbf{v}}\cdot\left\{v^2(\mathbf{E}+\mathbf{v}\times\mathbf{B})f_s\right\}d\mathbf{v} - \frac{q_s}{m_s}\int\nabla_{\mathbf{v}}\cdot\left\{v^2(\mathbf{E}+\mathbf{v}\times\mathbf{B})\right\}f_s d\mathbf{v}. \tag{2.55}$$

The volume integral of the first term can be changed to a surface integral by the divergence theorem. This surface integral becomes zero since f_s becomes zero at the volume boundary $v=\infty$. Therefore, the first term vanishes. From the vector algebra

relation $\nabla \cdot (\Phi \mathbf{F}) = \mathbf{F} \cdot \nabla\Phi + \Phi \nabla \cdot \mathbf{F}$, the second term of equation (2.55) becomes:

$$
\begin{aligned}
&-\frac{q_s}{m_s} \int \nabla_{\mathbf{v}} \cdot \left\{ v^2 (\mathbf{E} + \mathbf{v} \times \mathbf{B}) \right\} f_s d\mathbf{v} \\
&\quad = -\frac{q_s}{m_s} \int \left\{ \nabla_{\mathbf{v}} v^2 \cdot (\mathbf{E} + \mathbf{v} \times \mathbf{B}) + v^2 \nabla_{\mathbf{v}} \cdot (\mathbf{E} + \mathbf{v} \times \mathbf{B}) \right\} f_s d\mathbf{v} \qquad (2.56) \\
&\quad = -\frac{q_s}{m_s} \int 2\mathbf{v} \cdot (\mathbf{E} + \mathbf{v} \times \mathbf{B}) f_s d\mathbf{v} = -\frac{q_s}{m_s} \int 2\mathbf{v} \cdot \mathbf{E} f_s d\mathbf{v} \qquad (2.57) \\
&\quad = -\frac{2 n_s q_s \mathbf{u}_s}{m_s} \cdot \mathbf{E} = -\frac{2}{m_s} \mathbf{J}_s \cdot \mathbf{E}. \qquad (2.58)
\end{aligned}
$$

The second term in equation (2.56) vanishes because $\mathbf{E}$ and $\mathbf{B}$ do not depend on $\mathbf{v}$. By combining the remaining terms of equation (2.42), the third moment of Vlasov equation becomes:

$$
\frac{\partial}{\partial t} \left(\frac{3\mathrm{p}_s}{m_s} + n_s u_s^2 \right) + \nabla_{\mathbf{r}} \cdot \left(\frac{2\tilde{\mathrm{q}}_s}{m_s} + \frac{3\mathrm{p}_s}{m_s} \mathbf{u}_s + n_s u_s^2 \mathbf{u}_s + 2\mathbf{u}_s \cdot \frac{\tilde{\mathrm{P}}_s}{m_s} \right) - \frac{2}{m_s} \mathbf{J}_s \cdot \mathbf{E} = 0 \qquad (2.59)
$$

which describes the conservation of energy. This equation is equivalent to:

$$
\frac{\partial}{\partial t} \left(\frac{3\mathrm{p}_s}{2} + \frac{1}{2} \rho_{ms} u_s^2 \right) + \nabla_{\mathbf{r}} \cdot \left(\tilde{\mathrm{q}}_s + \frac{3}{2} \mathrm{p}_s \mathbf{u}_s + \frac{1}{2} \rho_{ms} u_s^2 \mathbf{u}_s + \mathbf{u}_s \cdot \tilde{\mathrm{P}}_s \right) - \mathbf{J}_s \cdot \mathbf{E} = 0. \qquad (2.60)
$$

If the distribution function f_s is spherically symmetric in velocity space, $\tilde{\mathrm{q}}_s = 0$ and $\tilde{\mathrm{P}}_s = \mathrm{p}_s \mathbf{I}$. Then, this energy conservation equation reduces to:

$$
\boxed{\frac{\partial}{\partial t} \left(\frac{3\mathrm{p}_s}{2} + \frac{1}{2} \rho_{ms} u_s^2 \right) + \nabla_{\mathbf{r}} \cdot \left(\frac{5}{2} \mathrm{p}_s \mathbf{u}_s + \frac{1}{2} \rho_{ms} u_s^2 \mathbf{u}_s \right) - \mathbf{J}_s \cdot \mathbf{E} = 0.} \qquad (2.61)
$$

One-fluid parameters and equations

We have introduced mass, momentum, and energy conservation equations of plasma species s. Since space plasmas consist of electrons and multiple ion species, the combined movement of all these species becomes very complicated. However, over 95% of ions in space plasmas are protons. Protons can be practically considered the sole ion source. By combining the conservation equations of protons and electrons, we obtain simple and powerful one-fluid equations.

Under the assumption that space plasma is composed of only electrons and protons, the total mass density ρ_m, total charge density ρ_q, total pressure p, total current density $\mathbf{J}$, and bulk flow velocity $\mathbf{u}$ are defined as:

$$\rho_m = m_p n_p + m_e n_e = \rho_{mp} + \rho_{me} \simeq \rho_{mp} \tag{2.62}$$

$$\rho_q = e(n_p - n_e) \simeq 0 \tag{2.63}$$

$$\mathrm{p} = \mathrm{p}_p + \mathrm{p}_e \tag{2.64}$$

$$\mathbf{J} = e(n_p \mathbf{u}_p - n_e \mathbf{u}_e) \tag{2.65}$$

$$\mathbf{u} = \frac{\rho_{mp}\mathbf{u}_p + \rho_{me}\mathbf{u}_e}{\rho_m} \simeq \mathbf{u}_p. \tag{2.66}$$

Since $m_e \ll m_i$, the total mass density and the bulk flow velocity are approximately the same as the mass density and bulk flow velocity of ions. The charge density ρ_q is approximately zero because of a plasma's quasi-neutrality, i.e. $n_p \simeq n_e$.

To obtain the continuity equation of a single fluid, we combine the continuity equations of electrons and protons. By using equation (2.29):

$$\frac{\partial}{\partial t}(\rho_{mp} + \rho_{me}) + \nabla_{\mathbf{r}} \cdot (\rho_{mp}\mathbf{u}_p + \rho_{me}\mathbf{u}_e) = 0. \tag{2.67}$$

This becomes:

$$\boxed{\frac{\partial \rho_m}{\partial t} + \nabla_{\mathbf{r}} \cdot (\rho_m \mathbf{u}) = 0.} \tag{2.68}$$

From equation (2.41), the momentum conservation equations of protons and electrons are:

$$\frac{\partial(\rho_{mp}\mathbf{u}_p)}{\partial t} + \nabla_{\mathbf{r}} \cdot (\mathrm{p}_p \mathbf{I} + \rho_{mp}\mathbf{u}_p\mathbf{u}_p) - \rho_{qp}\mathbf{E} - \mathbf{J}_p \times \mathbf{B} = 0 \tag{2.69}$$

$$\frac{\partial(\rho_{me}\mathbf{u}_e)}{\partial t} + \nabla_{\mathbf{r}} \cdot (\mathrm{p}_e \mathbf{I} + \rho_{me}\mathbf{u}_e\mathbf{u}_e) - \rho_{qe}\mathbf{E} - \mathbf{J}_e \times \mathbf{B} = 0. \tag{2.70}$$

By combining the two equations above, the first term becomes:

$$\frac{\partial(\rho_{mp}\mathbf{u}_p + \rho_{me}\mathbf{u}_e)}{\partial t} = \frac{\partial(\rho_m \mathbf{u})}{\partial t}. \tag{2.71}$$

Then, the second term becomes:

$$\nabla_{\mathbf{r}} \cdot (\mathrm{p}_p\mathbf{I} + \mathrm{p}_e\mathbf{I} + \rho_{mp}\mathbf{u}_p\mathbf{u}_p + \rho_{me}\mathbf{u}_e\mathbf{u}_e) = \nabla_{\mathbf{r}} \cdot (\mathrm{p}\mathbf{I} + \rho_{mp}\mathbf{u}_p\mathbf{u}_p + \rho_{me}\mathbf{u}_e\mathbf{u}_e) \tag{2.72}$$

$$\simeq \nabla_{\mathbf{r}} \cdot (\mathrm{p}\mathbf{I} + \rho_m\mathbf{u}\mathbf{u}). \tag{2.73}$$

Because plasma is quasi-neutral, i.e. $n_p \simeq n_e$, and $m_e \ll m_p$, we use the approximations $\rho_m \simeq \rho_{mp}$ and $\mathbf{u} \simeq \mathbf{u}_p$ in equation (2.73). Therefore:

$$\rho_{mp}\mathbf{u}_p\mathbf{u}_p + \rho_{me}\mathbf{u}_e\mathbf{u}_e \simeq \rho_{mp}\left(\mathbf{u}_p\mathbf{u}_p + \frac{m_e}{m_p}\mathbf{u}_e\mathbf{u}_e\right) \simeq \rho_m\mathbf{u}\mathbf{u}. \tag{2.74}$$

The last two terms are:

$$-(\rho_{qp} + \rho_{qe})\mathbf{E} - (\mathbf{J}_p + \mathbf{J}_e) \times \mathbf{B} = -\rho_q\mathbf{E} - \mathbf{J} \times \mathbf{B}. \tag{2.75}$$

From the quasi-neutrality of plasma, $\rho_q\mathbf{E}$ becomes zero. Finally, the momentum conservation equation for a single fluid becomes:

$$\boxed{\frac{\partial(\rho_m\mathbf{u})}{\partial t} + \nabla_r \cdot (\mathrm{p}\mathbf{I} + \rho_m\mathbf{u}\mathbf{u}) - \mathbf{J} \times \mathbf{B} = 0.} \tag{2.76}$$

To obtain the energy conservation equation, we use equation (2.61) for protons and electrons:

$$\frac{\partial}{\partial t}\left(\frac{3\mathrm{p}_p}{2} + \frac{1}{2}\rho_{mp}u_p^2\right) + \nabla_{\mathbf{r}} \cdot \left(\frac{5}{2}\mathrm{p}_p\mathbf{u}_p + \frac{1}{2}\rho_{mp}u_p^2\mathbf{u}_p\right) - \mathbf{J}_p \cdot \mathbf{E} = 0 \tag{2.77}$$

$$\frac{\partial}{\partial t}\left(\frac{3\mathrm{p}_e}{2} + \frac{1}{2}\rho_{me}u_e^2\right) + \nabla_{\mathbf{r}} \cdot \left(\frac{5}{2}\mathrm{p}_e\mathbf{u}_e + \frac{1}{2}\rho_{me}u_e^2\mathbf{u}_e\right) - \mathbf{J}_e \cdot \mathbf{E} = 0. \tag{2.78}$$

By adding these two equations, the energy equation becomes:

$$\boxed{\frac{\partial}{\partial t}\left(\frac{3}{2}\mathrm{p} + \frac{1}{2}\rho_m u^2\right) + \nabla_{\mathbf{r}} \cdot \left(\frac{5}{2}\mathrm{p}\mathbf{u} + \frac{1}{2}\rho_m u^2\mathbf{u}\right) - \mathbf{J} \cdot \mathbf{E} = 0} \tag{2.79}$$

where the same approximation used in the momentum equation was applied.

2.1.2 Generalized Ohm's law

In addition to the three conservation equations, generalized Ohm's law is also a useful equation, since it relates **E** with other variables. In an attempt to derive this

generalized Ohm's law, we introduce a collision term on the right side of equation (2.41):

$$\frac{\partial(\rho_{ms}\mathbf{u}_s)}{\partial t} + \nabla_{\mathbf{r}} \cdot (\mathrm{p}_s\mathbf{I} + \rho_{ms}\mathbf{u}_s\mathbf{u}_s) - \rho_{qs}\mathbf{E} - \mathbf{J}_s \times \mathbf{B} = \frac{\delta \mathbf{p}_s}{\delta t}_{collision}. \tag{2.80}$$

The collision term $\frac{\delta \mathbf{p}_s}{\delta t}_{collision}$ describes momentum transfer between plasma species, and can be expressed as:

$$\frac{\delta \mathbf{p}_s}{\delta t}_{collision} = -m_s n_s \nu_{sr}(\mathbf{u}_s - \mathbf{u}_r) \tag{2.81}$$

where ν_{sr} is the collision frequency between two species s and r, and $(\mathbf{u}_s - \mathbf{u}_r)$ is small compared to the thermal velocities of the two species. The momentum equations for protons and electrons are:

$$\frac{\partial(\rho_{mp}\mathbf{u}_p)}{\partial t} + \nabla_{\mathbf{r}} \cdot (\mathrm{p}_p\mathbf{I} + \rho_{mp}\mathbf{u}_p\mathbf{u}_p) - \rho_{qp}\mathbf{E} - \mathbf{J}_p \times \mathbf{B} = -\rho_{mp}(\mathbf{u}_p - \mathbf{u}_e)\nu_{pe} \tag{2.82}$$

$$\frac{\partial(\rho_{me}\mathbf{u}_e)}{\partial t} + \nabla_{\mathbf{r}} \cdot (\mathrm{p}_e\mathbf{I} + \rho_{me}\mathbf{u}_e\mathbf{u}_e) - \rho_{qe}\mathbf{E} - \mathbf{J}_e \times \mathbf{B} = -\rho_{me}(\mathbf{u}_e - \mathbf{u}_p)\nu_{ep}. \tag{2.83}$$

If we assume momentum conservation during collisions, the momentum gain of the proton system should be the same as the momentum loss of the electron system. Therefore:

$$-\rho_{mp}(\mathbf{u}_p - \mathbf{u}_e)\nu_{pe} = \rho_{me}(\mathbf{u}_e - \mathbf{u}_p)\nu_{ep} \tag{2.84}$$

$$\rho_{mp}\nu_{pe} = \rho_{me}\nu_{ep}. \tag{2.85}$$

By multiplying m_e into equation (2.82) and m_p into equation(2.83), and then subtracting the two equations from each other:

$$m_e m_p \frac{\partial}{\partial t}\{n(\mathbf{u}_p - \mathbf{u}_e)\} + (m_e\nabla_{\mathbf{r}}\mathrm{p}_p - m_p\nabla_{\mathbf{r}}\mathrm{p}_e) + m_e m_p \nabla_{\mathbf{r}} \cdot \{n(\mathbf{u}_p\mathbf{u}_p - \mathbf{u}_e\mathbf{u}_e)\}$$
$$- \rho_m e\mathbf{E} - ne(m_e\mathbf{u}_p + m_i\mathbf{u}_e) \times \mathbf{B} = -\rho_{me}\nu_{ep}(\mathbf{u}_p - \mathbf{u}_e)(m_p + m_e) \tag{2.86}$$

where we used the quasi-neutrality of a plasma, i.e., $n_p \simeq n_e \equiv n$. From $\mathbf{J} = ne(\mathbf{u}_p - \mathbf{u}_e)$, the first term becomes:

$$m_e m_p \frac{\partial}{\partial t}\{n(\mathbf{u}_p - \mathbf{u}_e)\} = \frac{m_e m_p}{e}\frac{\partial \mathbf{J}}{\partial t}. \tag{2.87}$$

The second term is approximately $-m_p\nabla_{\mathbf{r}}\mathrm{p}_e$ since $m_e \ll m_p$, and the third term becomes:

$$m_e m_p \nabla_{\mathbf{r}} \cdot \{n(\mathbf{u}_p\mathbf{u}_p - \mathbf{u}_e\mathbf{u}_e)\} = m_e m_p \nabla_{\mathbf{r}} \cdot \{n\mathbf{u}_p(\mathbf{u}_p - \mathbf{u}_e) + n(\mathbf{u}_p - \mathbf{u}_e)\mathbf{u}_e)\} \quad (2.88)$$

$$= \frac{m_e m_p}{e}\nabla_{\mathbf{r}} \cdot (\mathbf{u}_p\mathbf{J} + \mathbf{J}\mathbf{u}_e). \quad (2.89)$$

Then, the fifth term becomes:

$$-ne(m_e\mathbf{u}_p + m_i\mathbf{u}_e) \times \mathbf{B} = -ne\left\{(m_e + m_i)\mathbf{U} - (m_i - m_e)\frac{\mathbf{J}}{ne}\right\} \times \mathbf{B} \quad (2.90)$$

where the bulk flow velocity, $\mathbf{U}$, and total current density, $\mathbf{J}$, are obtained from:

$$\mathbf{U} = \frac{\rho_{mp}\mathbf{u}_p + \rho_{me}\mathbf{u}_e}{\rho_m} \quad (2.91)$$

$$\mathbf{J} = e(n_p\mathbf{u}_p - n_e\mathbf{u}_e). \quad (2.92)$$

From $m_e \ll m_p$, the right side of equation (2.86) becomes:

$$-\rho_{me}\nu_{ep}(\mathbf{u}_p - \mathbf{u}_e)(m_p + m_e) \simeq -e\rho_{mp}\left(\frac{m_e\nu_{ep}}{ne^2}\right)\mathbf{J} \quad (2.93)$$

$$\equiv -\frac{e\rho_{mp}}{\sigma}\mathbf{J} \equiv -e\rho_{mp}\eta\mathbf{J} \quad (2.94)$$

where σ is the conductivity, and η is the inverse of conductivity, i.e., resistivity. Combining all remaining terms of equation (2.86):

$$\frac{m_e m_p}{e}\frac{\partial\mathbf{J}}{\partial t} - m_p\nabla_{\mathbf{r}}\mathrm{p}_e + \frac{m_e m_p}{e}\nabla_{\mathbf{r}} \cdot (\mathbf{u}_p\mathbf{J} + \mathbf{J}\mathbf{u}_e) - \rho_m e\mathbf{E}$$
$$- ne\left\{(m_e + m_i)\mathbf{U} - (m_i - m_e)\frac{\mathbf{J}}{ne}\right\} \times \mathbf{B} + e\rho_{mp}\eta\mathbf{J} = 0. \quad (2.95)$$

Then, we re-write the above equation as an equation of $\mathbf{E}$:

$$\boxed{\mathbf{E} = -\mathbf{U} \times \mathbf{B} - \frac{1}{ne}\nabla_{\mathbf{r}}\mathrm{p}_e + \eta\mathbf{J} + \frac{1}{ne}\mathbf{J} \times \mathbf{B} + \frac{m_e}{ne^2}\left\{\frac{\partial\mathbf{J}}{\partial t} + \nabla_{\mathbf{r}} \cdot (\mathbf{u}_p\mathbf{J} + \mathbf{J}\mathbf{u}_e)\right\}.} \quad (2.96)$$

This equation is the generalized Ohm's law.

We can simplify the above equation by using scale analysis. The purpose of scale analysis is to calculate typical scales of each term and neglect very small terms. Let's assume that the typical length and time scales of the plasma motion we are interested in are L and τ, respectively. Accordingly, a typical velocity scale becomes $U = L/\tau$. The temporal and spatial derivatives can be replaced as follows:

$$\frac{\partial}{\partial t} \to \frac{1}{\tau}, \quad \nabla_{\mathbf{r}} \to \frac{1}{L}. \tag{2.97}$$

Then, equation (2.96) becomes:

$$E = -UB\left[1 + \frac{1}{UB} \cdot \frac{\mathrm{p}_e}{neL}\right] + \eta J\left[1 + \frac{eB}{m_e \nu_{ep}} + \frac{1}{\nu_{ep}}\left\{\frac{1}{\tau} + \frac{U}{L}\right\}\right]. \tag{2.98}$$

A single fluid model implicitly assumes that electrons and ions have the same temperature, i.e., $T_e = T_i = T$. Therefore, the thermal pressure of electrons can be expressed as $\mathrm{p}_e = nk_BT_e = nk_BT_i$ with quasi-neutrality of plasma, $n_e = n_i = n$. From the gyrofrequency, $\omega_c = eB/m$, and gyroperiod, $\tau_c = 1/\omega_c$, the above equation becomes:

$$E = -UB\left[1 + \frac{k_BT_i}{e\tau U^2 B} \cdot \frac{m_i}{m_i}\right] + \eta J\left[1 + \frac{\omega_{ce}}{\nu_{ep}} + \frac{2}{\nu_{ep}\tau}\right] \tag{2.99}$$

$$= -UB\left[1 + \frac{\tau_{ci}}{\tau} \cdot \frac{c_i^2}{U^2}\right] + \eta J\left[1 + \frac{\tau_{ep}}{\tau_{ce}} + \frac{2\tau_{ep}}{\tau}\right] \tag{2.100}$$

where τ_{ep} is the collision time and $c_i = \sqrt{k_BT_i/m_i}$ is the thermal velocity of ions. If the time scale of the plasma motion is much longer than both the collision time and the ion's gyroperiod, i.e., $\tau_{ep}/\tau \ll 1$ and $\tau_{ci}/\tau \ll 1$, the second term in the UB bracket and the last term in the ηJ bracket are negligible. Then, the generalized ohm's law reduces to:

$$\mathbf{E} = -\mathbf{U} \times \mathbf{B} + \eta \mathbf{J} + \frac{1}{ne}\mathbf{J} \times \mathbf{B}. \tag{2.101}$$

The last term of the above equation is called the Hall term. If we further assume that the electron's gyroperiod is much longer than the collision time, i.e., $\tau_{ep}/\tau_{ce} \ll 1$, this

Hall term becomes negligible. Then, the generalized Ohm's law is simplified as:

$$\mathbf{E} = -\mathbf{U} \times \mathbf{B} + \eta \mathbf{J}. \tag{2.102}$$

For a collisionless plasma, the resistivity, η, goes to zero as the collision frequency, ν_{ep}, becomes zero. The above equation can be further simplified as:

$$\mathbf{E} = -\mathbf{U} \times \mathbf{B} \tag{2.103}$$

which is called ideal Ohm's law. A plasma that satisfies this ideal Ohm's law is called an ideal MHD plasma.

For ideal MHD, plasma elements are frozen in magnetic field lines and do not interact with the other plasma elements in different magnetic field lines. Thus, magnetic reconnection does not happen in ideal MHD. However, reconnection phenomenon have long been observed in space plasma near the dayside magnetopause or the neutral current sheet of the magnetotail. In order to produce more realistic plasma motion, scientists have widely used the resistive form of Ohm's law, i.e., equation (2.102), because "it represents the simplest and qualitatively most important deviation from the ideal MHD model" [*Gurnett and Bhattacharjee*, 2005]. This approach does not violate severely the basic MHD assumption of collisionless plasma since reconnection occurs in a small scale. The typical length scale of reconnection is known to be ∼10 km for electrons and ∼100 km for protons [*Vaivads et al.* 2009]. Therefore, the MHD models introduce non-zero resistivity only in a small region, and apply ideal MHD approaches to the rest of the space plasma regions.

2.1.3 Maxwell's equations

Since a plasma is composed of charged particles, its motion depends on **E** and **B**, which is governed by Maxwell equations:

$$\nabla_{\mathbf{r}} \cdot \mathbf{E} = \frac{\rho_q}{\varepsilon_0} \tag{2.104}$$

$$\nabla_{\mathbf{r}} \cdot \mathbf{B} = 0 \tag{2.105}$$

$$\nabla_{\mathbf{r}} \times \mathbf{E} = -\frac{\partial \mathbf{B}}{\partial t} \tag{2.106}$$

$$\nabla_{\mathbf{r}} \times \mathbf{B} = \mu_0 \varepsilon_0 \frac{\partial \mathbf{E}}{\partial t} + \mu_0 \mathbf{J}. \tag{2.107}$$

From the quasi-neutrality of a plasma ($\rho_q \approx 0$), ρ_q/ε_0 is negligible. In addition, we can ignore the displacement current, $\mu_0\varepsilon_0 \partial \mathbf{E}/\partial t$, by using scale analysis. As in the previous section, we assume that the spatial and temporal scales of plasma motion are L and τ. Then, equation (2.106) is expressed as:

$$\frac{E}{L} = \frac{B}{\tau} \quad \rightarrow \quad E = UB. \tag{2.108}$$

From the above equation, equation (2.107) becomes:

$$\frac{B}{L} = \frac{1}{c^2}\frac{E}{T} + \mu_0 J = \frac{UB}{c^2 T} + \mu_0 J \tag{2.109}$$

$$B = \frac{U^2}{c^2} B + \mu_0 J \tag{2.110}$$

where $c = \sqrt{1/\mu_0\varepsilon_0}$ is the speed of light. If the plasma motion is much slower than the speed of light (i.e., non-relativistic), the displacement current can be neglected. Therefore, the simplified Maxwell equations for a single-fluid plasma become:

$$\nabla_{\mathbf{r}} \cdot \mathbf{E} = 0 \tag{2.111}$$

$$\nabla_{\mathbf{r}} \cdot \mathbf{B} = 0 \tag{2.112}$$

$$\nabla_{\mathbf{r}} \times \mathbf{E} = -\frac{\partial \mathbf{B}}{\partial t} \tag{2.113}$$

$$\nabla_{\mathbf{r}} \times \mathbf{B} = \mu_0 \mathbf{J}. \tag{2.114}$$

2.1.4 Summary

The complete set of one-fluid MHD equations are:

$$\frac{\partial \rho_m}{\partial t} + \nabla \cdot (\rho_m \mathbf{u}) = 0 \tag{2.115}$$

$$\frac{\partial (\rho_m \mathbf{u})}{\partial t} + \nabla \cdot (\mathrm{p}\mathbf{I} + \rho_m \mathbf{u}\mathbf{u}) - \mathbf{J} \times \mathbf{B} = 0 \tag{2.116}$$

$$\frac{\partial \varepsilon}{\partial t} + \nabla \cdot \{(\mathrm{p} + \varepsilon)\mathbf{u}\} - \mathbf{J} \cdot \mathbf{E} = 0 \tag{2.117}$$

$$\varepsilon = \frac{3}{2}\mathrm{p} + \frac{1}{2}\rho_m u^2 \tag{2.118}$$

$$\mathbf{E} = -\mathbf{U} \times \mathbf{B} + \eta \mathbf{J} \tag{2.119}$$

$$\nabla_{\mathbf{r}} \cdot \mathbf{E} = 0 \tag{2.120}$$

$$\nabla_{\mathbf{r}} \cdot \mathbf{B} = 0 \tag{2.121}$$

$$\nabla_{\mathbf{r}} \times \mathbf{E} = -\frac{\partial \mathbf{B}}{\partial t} \tag{2.122}$$

$$\nabla_{\mathbf{r}} \times \mathbf{B} = \mu_0 \mathbf{J}. \tag{2.123}$$

The above equations are derived from the following assumptions:

1. Plasma is composed of only protons and electrons.

2. Plasma is quasi-neutral.

3. Plasma pressure is isotropic.

4. Electron inertia is negligible in comparison with ion inertia, i.e., $\mathbf{u} \approx \mathbf{u}_i$, since $m_e \ll m_i$.

5. The plasma motions are non-relativistic.

6. The typical length scale of the plasma motion is much larger than kinetic length scales such as ion gyroradius and collisional mean free path.

7. The typical time scale of the plasma motion is much longer than kinetic time scales such as ion gyroperiod and collision time.

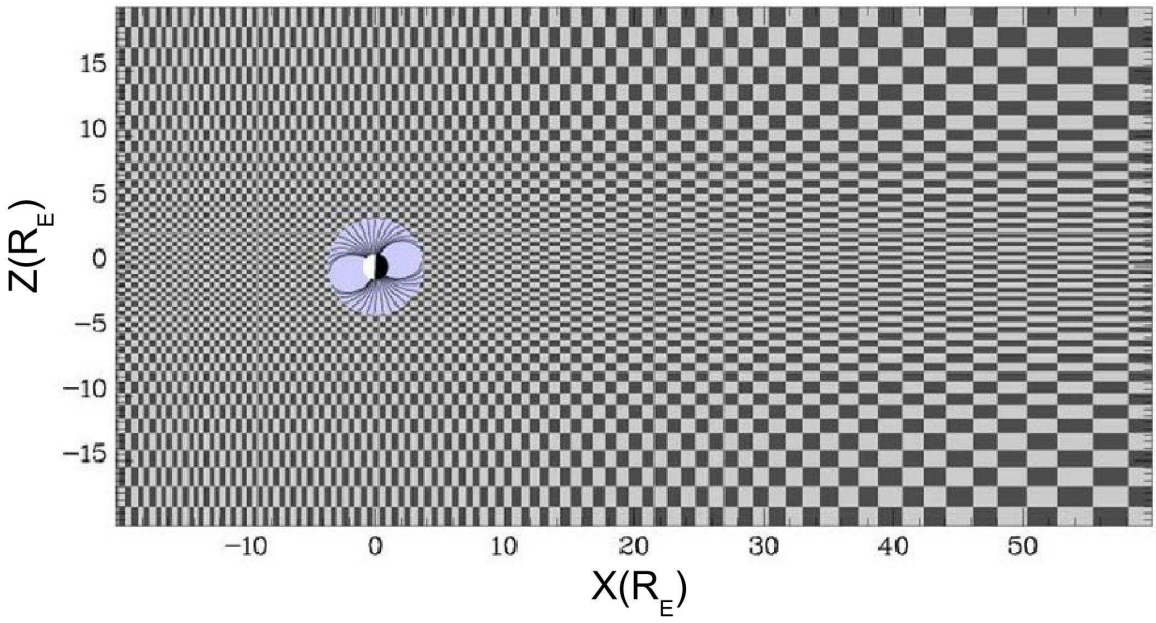

Figure 2-1: Two different sections of the OpenGGCM model. [*Raeder et al.*, 2008]

8. Plasma is collisionless except in reconnection region.

2.2 OpenGGCM

The OpenGGCM model is a 3D global magnetosphere-ionosphere MHD model. OpenGGCM divides the Earth's magnetospheric system into two regions, and applies different calculation strategies based on the main physical process in each region. One region contains the magnetosphere whose inner boundary is located at 3–4 R_E from the Earth and whose outer boundary is far enough away to cover the entire magnetospheric system. As plasma in this region acts like a fluid, the MHD equations are used. The other region is inside the inner boundary of the magnetosphere. The MHD approach is not applicable anymore in this region because of magnetosphere-ionosphere coupling. Figure 2-1 shows these two different regions inside OpenGGCM. We will discuss the calculation strategy of each region briefly in the following sub-

sections. More detailed information about the OpenGGCM model can be found in *Raeder et al.* [1998, 2001, 2003, 2008].

2.2.1 Magnetosphere

The magnetosphere is solved by MHD equations (2.115) – (2.123) as an initial boundary value problem. Since all the MHD models including OpenGGCM use discrete grids in time and space, the differential MHD equations are discretized into finite-difference equations, producing unavoidable numerical errors. These errors act like diffusion, viscosity, and resistivity inside the MHD models, allowing viscous interactions and magnetic reconnection to a limited extent. As these numerical effects are not sufficient, the MHD models introduce an anomalous resistivity that violates the ideal Ohm's law, $\mathbf{E} = -\mathbf{V} \times \mathbf{B}$. This resistivity can be aroused by a variety of MHD and kinetic plasma instabilities such as tearing instability, current-driven kinetic instabilities, coalescence instability, and radiative instability [*Schumacher and Kliem*, 1996]. OpenGGCM introduces the anomalous resistivity, η, caused by current-driven instabilities [*Sato and Hayashi*, 1979], as a function of the local current density, j, under the following conditions:

$$\eta = \begin{cases} \alpha j'^2 & : j' \geq \delta \\ 0 & : j' < \delta \end{cases} \tag{2.124}$$

$$j' = \frac{|j|\Delta}{|\mathbf{B}| + \varepsilon} \tag{2.125}$$

where j' is the normalized current density, $\mathbf{B}$ is the local magnetic field, Δ is the grid spacing, δ and α are empirical constants, and ε is a very small number for the denominator not to be zero.

The numerical grids for OpenGGCM are non-uniform Cartesian grids, and are easily changeable to obtain high-resolution data in the region of interest. The black and white squares in Figure 2-1 show how the OpenGGCM grids are located. The

grids in this figure are more densely located on the dayside magnetosphere and near the noon-midnight meridian. The simulation box for the OpenGGCM model normally extends from ∼20 R_E sunward to several hundred R_E anti-sunward and ∼45 R_E in both positive and negative directions of y and z axes.

The OpenGGCM model uses a free flow condition as the boundary condition for all sides of the simulation box except for the sunward side. This flow condition is given by:

$$\frac{\partial \Psi}{\partial \mathbf{n}} = 0 \tag{2.126}$$

where Ψ are all variables except the normal magnetic field. This normal magnetic field must be calculated from $\nabla \cdot \mathbf{B} = 0$ in order to satisfy Maxwell's equations. The boundary condition for the sunward side is set by the solar wind conditions, which are either arbitrarily given by the modeler or obtained from a solar wind monitor, such as ACE and WIND. By solving the MHD equations under these boundary conditions, OpenGGCM provides number densities, velocities, plasma pressures, and electromagnetic fields of the magnetosphere and its surrounding environments.

2.2.2 Magnetosphere-ionosphere coupling region

The magnetosphere region extends from the inner boundary, which is located at 3–4 R_E from the Earth, to the simulation box sides. Inside this inner boundary is the magnetosphere-ionosphere (MI) coupling region. Since the physical processes in this region are more of a kinetic nature, the fluid approach is not applicable. Instead of the MHD equations, OpenGGCM applies a simple magnetosphere-ionosphere coupling model. This model obtains the field aligned currents (FACs) of the inner boundary from the MHD calculations, and maps the FACs to the ionosphere along the dipole magnetic field lines. The MI coupling region of Figure 2-1 shows how the mapping is done. Because of this mapping process, the numerical grids for the ionosphere

cover $\sim$ 58° to 90° latitude. Under the assumption that the FACs are closed in the ionosphere, the MI coupling model calculates the electrical potential based on the ionospheric potential equation [*Raeder*, 2003; *Raeder et al.*, 2008]. OpenGGCM maps this potential back to the inner boundary of the MHD part, and uses it as the boundary condition for magnetospheric flows.

2.2.3 Additional OpenGGCM details for our research

In this dissertation, we set the OpenGGCM simulation box at [x= -300 – 24 R_E, y= -48 – 48 R_E, z= -48 – 48 R_E] in GSE coordinates. More than 36 million grid cells are used, and they are most densely located in the dayside magnetosphere, in order to obtain high-resolution in this region. The time resolution of the OpenGGCM output fields that are used by LTPT models is one minute.

Since the OpenGGCM model used in this study does not include the dynamic processes of the plasmasphere and the ring current, we gradually replace the MHD electromagnetic field with the dipole magnetic field and the corrotational electric field in the region between 7 – 5 R_E. Thus, the magnetic (electric) field used to integrate particle trajectories in the LTPT model is a pure dipole field (a pure corrotational electric field) inside of 5 R_E, purely the MHD magnetic (electric) field outside of 7 R_E, and in between, a linear combination of the two magnetic (electric) fields.

The cusp in the OpenGGCM model tends to be located at a lower latitude than in reality. This may be because OpenGGCM produces excessive plasma flow into the cusp or because a weak ring current in the OpenGGCM model moves the magnetopause earthward, locating the cusp at a lower latitude.

2.3 LTPT

Liouville Theorem Particle Tracer (LTPT) is composed of two codes: an ion tracer and a density calculator. The ion tracer calculates trajectories of test ions from the cusp to the magnetosheath where velocity distribution is known. The density calculator maps phase-space densities of the test ions from the magnetosheath to the cusp by using Liouville's theorem. OpenGGCM provides all the necessary information to the LTPT model in order to calculate the ion trajectories and the magnetosheath velocity distribution. Since LTPT uses the test particle approach, no coupling is considered between OpenGGCM and LTPT. In this section, we discuss the details of LTPT.

2.3.1 Ion Tracer

The ion tracer tracks ions backward in time from an observation point in the cusp to the magnetosheath. While the forward-tracing method, also called Large Scale Kinetics (LSK) [*Peroomian et al.* 1994, 2007], traces numerous ions from the upstream region to gather enough ions in the cusp, this backward-tracing method traces only ions precipitating into the cusp, therefore avoiding unnecessary calculation. To calculate the ion trajectories, the tracer integrates the Lorentz equation and the equation of motion:

$$\frac{d\mathbf{v}}{dt} = \frac{q}{m}\left(\mathbf{E} + \mathbf{v} \times \mathbf{B}\right) \tag{2.127}$$

$$\frac{d\mathbf{r}}{dt} = \mathbf{v} \tag{2.128}$$

where $\mathbf{E}$ and $\mathbf{B}$ are electromagnetic fields obtained from OpenGGCM simulations. To reduce numerical error during the integration, the Runge-Kutta 4th order method is used with a time step of 0.05 times the local gyroperiod. The maximum time step is set at 60 seconds which is OpenGGCM's time resolution. OpenGGCM calculates all values at its grid at every minute, and therefore we use linear interpolation in space

and time to obtain the values at a given position at a given time.

The ion tracer launches 336 cusp ions per minute along a satellite orbit. These ions have 28 logarithmically distributed energies from 25 eV to 32 keV, and 12 equally distributed pitch angles from 7.5° to 172.5°. The energy/pitch-angle bins are the same as the ones used in the Toroidal Imaging Mass-Angle Spectrograph (TIMAS) on Polar [*Shelley et al.*, 1995], and are chosen in order to compare our result with Polar observations later in this dissertation. The same energy/pitch-angle bins are also used for modeling Cluster observations, since the Cluster Ion Spectrometry (CIS) sensors on the Cluster satellites (which have 31 energy bins between 5 eV – 35 keV and 8 pitch-angle bins between 11.25° – 168.75° [*Reme et al.*, 2001]) observe similar energy/pitch angle ranges as TIMAS on Polar. The ion tracer introduces particles at only one arbitrary phase angle since the phase-angle does not have significant impact on the ion trajectory because of gyromotion, which has been tested with our model.

The tracer stops its backward tracing when the cusp ion reaches the simulation box of the ion tracer, x=[-50–20] R_E, y=[-45 –45] R_E, z=[-45–45] R_E. Since cusp ions can come from both the dayside and nightside of the magnetosheath, we set this box big enough to cover most of the magnetosheath so that LTPT finds more magnetosheath ions to construct cusp spectrograms. The tracer also stops when the cusp ion reaches an altitude of 300km and when the ion travels 200 R_E in order to avoid unnecessary calculation of ionospheric and magnetospheric ions. In this dissertation, we trace the cusp ions for 1∼2 hours until our model uses all the time series of the OpenGGCM fields. Because of this time limit, our model tends to produce low flux (or energy flux) at the low energy part of the cusp spectrogram, especially near the high-latitude cusp. The previous models of Onsager and Wing show that ions precipitating at high latitudes originate from the nightside magnetopause. Since the nightside magnetopause is farther from the cusp than the dayside magnetopause, 1–2

hours may not be enough for low energy ions to reach the nightside magnetopause. This is why our model does not produce a good spectrogram at low energies. However, the model produces high-energy spectrograms reasonably well, and observers often focus on these higher energies to study the relation between cusp structures and dayside reconnection. The lack of low energy ions in a modeled spectrogram can be solved by running OpenGGCM for a longer period.

2.3.2 Density Calculator

The density calculator in the LTPT searches cusp ions coming from the magnetosheath and calculates their phase-space densities (PSDs). First, we calculate the magnetopause location inside the OpenGGCM model, and define a magnetosheath surface that encompasses the magnetopause. We fit the magnetopause to a paraboloid by using points of maximum number-density gradients along the x axis at y = z = 0 R_E and along the y and z axes on the yz plane at x = 5, 0, -5, -10, -20, -30 R_E. We calculate the magnetopause every minute during the satellite's cusp-crossing event, and select the magnetopause model with the largest standoff distance as the magnetosheath surface. This simple calculation method of both the magnetopause and magnetosheath surface is used in chapter 3 for the model validation test, and is advanced later in chapter 4 to obtain their locations more accurately. We consider a cusp ion as coming from the magnetosheath if it reaches the selected magnetosheath surface. While the empirical models of Onsager and Wing have another step to calculate energy gain or loss across the magnetopause, the ion tracer of LTPT handles the process internally in the OpenGGCM, which provides magnetopause properties, such as the magnetic field shear and the magnetopause current.

Then, we calculate PSDs of the magnetosheath ions by using their velocities in the magnetosheath and the velocity distribution of the magnetosheath. The veloc-

ity distribution is calculated under the assumption that magnetosheath ions can be represented by a kappa distribution:

$$f(\mathbf{r},\mathbf{v},t) = \frac{n(\mathbf{r},t)}{\pi^{3/2}w_0^3\kappa^{3/2}}\frac{\Gamma(\kappa+1)}{\Gamma(\kappa-1/2)}\left(1+\frac{|\mathbf{v}-\mathbf{v_d}(\mathbf{r},t)|^2}{\kappa w_0^2}\right)^{-(\kappa+1)}$$

$$w_0 = \sqrt{\frac{2kT}{m}}\left(\frac{\Gamma(\kappa-1/2)}{\kappa\Gamma(\kappa-3/2)}\right)^{1/2}$$

where n, $\mathbf{v_d}$, and T are the number density, drift velocity, and plasma temperature obtained from the OpenGGCM model, and w_0 is the most probable speed. We use $\kappa = 7$, based on *Wing et al.* [2001].

We assume that all ions behave as if they are in a collisionless system. This assumption is reasonable since the reconnection diffusion region is so small that our ions seldom encounter it. According to Liouville's theorem, the phase-space density is conserved along a particle trajectory in a collisionless system. Therefore, the PSDs calculated in the magnetosheath are the same as those observed in the cusp. Since most satellites observe the differential flux or energy flux, we calculate the flux by using the PSDs:

$$J = \frac{v^2}{m}f \tag{2.129}$$

where J is the differential flux, v the ion speed at the cusp, m the ion mass, and f the PSD calculated at the magnetosheath. The differential energy flux is the value of the differential flux, J, times the ion energy at the cusp.

Finally, we display the differential flux as an energy-time spectrogram. As we calculate the flux based on the velocity distribution of the magnetosheath plasma, model results may be affected by the distribution function as well as the simulated magnetosheath which provides density, velocity, and temperature for the source distribution function. We verified the robustness of our model results by introducing different kappa values, including $\kappa = \infty$, which is the Gaussian distribution, and different magnetosheath surfaces, which change the magnetosheath parameters. Despite

these changes, the main features of cusp spectrograms remain the same.

The modeled spectrogram tends to have higher flux than the observations. The same overestimation was found in the *Onsager et al.* [1995] model. Since only a part of the magnetosheath plasma is transmitted at the rotational discontinuity [*Cowley*, 1982; *Gosling et al.*, 1990; *Smith and Lockwood*, 1996], *Onsager et al.* [1995] introduce a reflection coefficient at the magnetopause to match the modeled results with the observations. On the other hand, our model assumes no collisions throughout the particle's trajectory from the cusp to the magnetosheath, and therefore does include reflection at the magnetopause. The higher fluxes in the model have likely other causes, for example, the lack of particle scattering by waves in the model.

The LTPT model, therefore, acts like the TIMAS instrument onboard virtual satellites. The ion tracer of the LTPT measures energy and pitch angle of the precipitating solar wind ions with a time resolution of one minute. The density calculator of the LTPT measures differential flux of these ions.

2.4 Summary of the modeling method

In this section, we briefly summarize the steps to model a cusp ion structure.

1. Run the OpenGGCM simulation with solar wind and IMF input.

2. Locate a virtual satellite in the OpenGGCM's cusp.

3. Launch ions with various energies and pitch angles from the satellite location, and trace them backward in time to see where they originate.

4. Search the ions from the magnetosheath and calculate their PSDs at the magnetosheath. By assuming no collision throughout the ion trajectories, these PSDs can be mapped to the cusp by using Liouville's theorem.

5. Calculate differential flux by using these PSDs and display the flux in the energy versus time or energy versus latitude spectrogram.

Chapter 3

Dynamic modeling of cusp ion structures

3.1 Introduction

In this chapter, we demonstrate our model's ability to produce reasonable cusp structures and investigate the reconnection properties causing these structures. We select three cusp crossing events observed by the Cluster and Polar satellites during dynamic solar wind and IMF conditions. We run the OpenGGCM simulations for the three events, and use the LTPT model with time-dependent electromagnetic fields obtained from OpenGGCM to reproduce the satellite observations. In each event study, we first test our model's validity by comparing the modeled and observed cusp structures. Then, we study whether the cusp structures are temporal or spatial by investigating the magnetopause movement and the particle trajectories inside the OpenGGCM-LTPT model. We also show how cusp structures are related to magnetopause processes.

While the previous models of *Onsager et al.* [1995] and *Wing et al.* [2001] assess their model results based only on visual similarity to the observations, we introduce a more objective method for the model-observation comparison. We set the following four comparison criteria: (a) dispersion in the correct direction is present, (b) distinct steps visible in the observations are also present in the predicted structures,

(c) the slope of the upper edge of the dispersed structure agrees within a factor of 2, and (d) the highest energy of dispersed ions coincides to within a factor of 2. We assess whether the model predictions are "excellent", "good", "satisfactory", or "non-satisfactory" according to the numbers of fulfilled criteria. If all 4 criteria are fulfilled without ambiguity, we call the fit "excellent". If either 3 of 4 criteria are fulfilled without ambiguity or all 4 are fulfilled, but with some ambiguity, we call the match "good". If 3 of the 4 criteria are fulfilled with some ambiguity, we call the match "satisfactory". Otherwise the match is called "not satisfactory".

3.2 Model Results and Discussion

3.2.1 23 September 2004 Case

The first case is a cusp-crossing event of Cluster on 23 September 2004. The Cluster satellites pass the northern cusp while southward IMF turns into northward IMF. This event was studied by *Escoubet et al.* [2008a] and we select this event to check our model's validity during the IMF change.

Figure 3-1 shows the SW/IMF obtained from ACE. IMF B_z changes its sign around 15:22. The number density, velocity, and solar wind pressure are about 4 cm^{-3}, 450 km/s , and 1.5 nPa, respectively. The OpenGGCM simulation is run with these SW/IMF conditions as input. Figure 3-2 shows Cluster orbits projected on a sphere of radius 5 Re. The plasma pressure and the open/closed field line boundary at 15:20 are calculated from OpenGGCM and projected on the same sphere of radius 5 Re as the color contour and the white line, respectively. The blue line is the orbit of three Cluster satellites C1, C3, and C4. The locations between the blue/green dots with time labels show where and when the C3/C4 observe the cusp ion structures. Satellite C1 is 2 minutes behind satellite C4.

The cusp is located near $-30\,^\circ$ GSE longitude where plasma pressure is very high

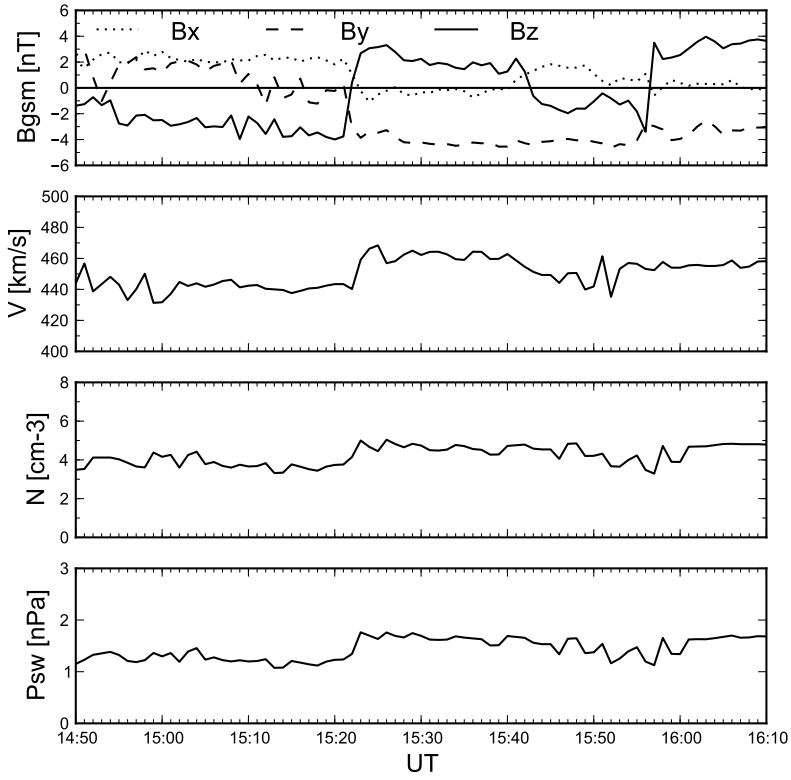

Figure 3-1: Solar wind and IMF conditions obtained from ACE on 23 September 2004. IMF, velocity, number density, and dynamic pressure are plotted. 10 minutes are added to the OMNI data in order to account for the SW/IMF propagation from the bowshock to the cusp.

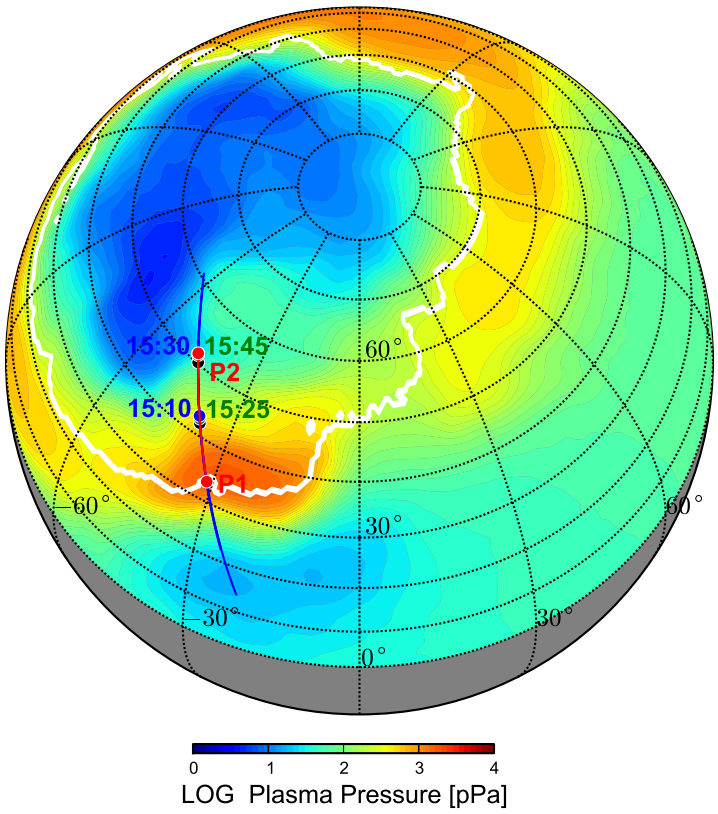

Figure 3-2: The Cluster orbit (the blue line) projected on the sphere of radius 5 Re. The plasma pressure (the color contour) and the open/closed field line boundary (the white line) at 15:20 are calculated from the OpenGGCM simulation. The C1/C3/C4 are located between the black/green/blue dots during the event. The red line between P1 and P2 is an orbit used for modeling a cusp ion structure.

(the red region in Figure 3-2). As the Cluster satellites are located outside of the model cusp, we shift the orbits toward the OpenGGCM's cusp in order to model cusp ion structures. Since the three Cluster satellites pass the same part of the cusp, we select only one orbit for modeling the three Cluster observations (the red line between two red dots P1 and P2).

In order to understand how a cusp structure changes in response to SW/IMF changes, we launch a total of 41 virtual satellites, one satellite every minute between 14:53 and 15:33. We record the cusp ion structures for 40 minutes along the red line from P1 to P2. The speeds of our virtual satellites are set at around 4.7 km/s, corresponding to the Cluster satellite speed. We present 15 of the results from the virtual satellites in Figure 3-3 for a quick look at the dependence of a cusp ion structure on the satellite crossing time. Each cusp structure is labeled with a satellite number. Satellites enter the cusp sequentially, and low-numbered satellites enter the cusp earlier than high-numbered satellites.

Virtual satellites S01-S09 pass the cusp while southward IMF changes into northward IMF. Satellites S01-S04 observe normally dispersed structures in spite of the IMF change because the magnetosphere is still influenced by the southward IMF. Satellites S05-S09 begin observing the reverse dispersions at the end of the spectrograms, and Satellites S10-13 enter the cusp during northward IMF, observing irregularly dispersed structures. This irregularity may appear because the magnetosphere adjusts to the IMF change at this time. The normal dispersions shown at the beginning of the S09-S11 observations have weaker energy flux than the ones in the S05-S08 observations, indicating that the subsolar reconnection becomes weaker as IMF turns northward. Satellites S14-S15 observe reverse dispersion of high-energy cutoff, which persists until the end of our model run.

Figure 3-4 shows where along the Cluster orbit the open/closed field line boundary

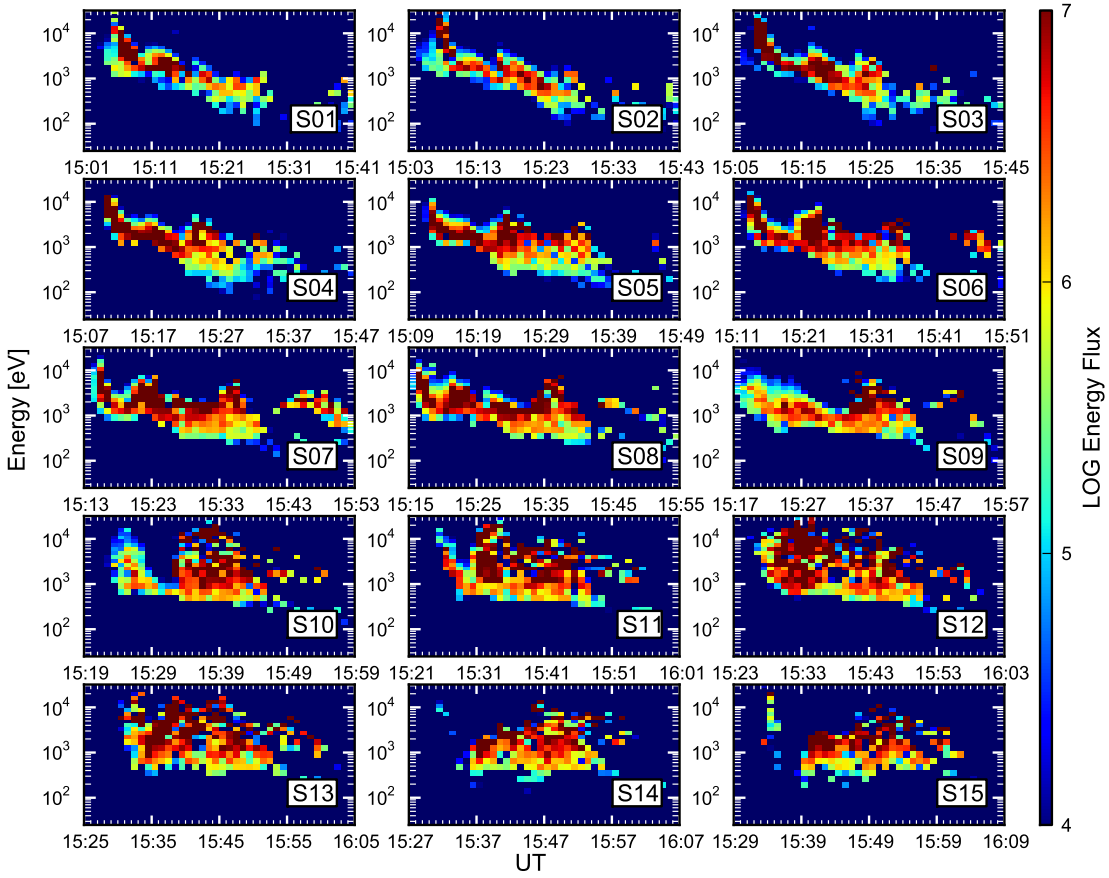

Figure 3-3: Model results of the Cluster event on 23 September 2004.

(OCB) is located. The white area represents the open field line zone and the gray area represents the closed field line zone. The black line shows the OCB and the red line shows the P1 location. We also show the magnetopause standoff distance (the blue line) by calculating the location of maximum current density along the Sun-Earth line.

The OCB slowly moves to the higher latitudes since IMF changes northward. This is because the subsolar reconnection changes into the lobe reconnection. At 15:23, we observe the temporal increase of OCB location with earthward movement of the magnetopause. This may relate to the sudden increase of solar wind pressure at 15:23 since northward IMF usually expands the magnetopause. The increased pressure may shrink the magnetopause and compress the magnetosphere. Since the OCB in Figure 3-4 is calculated at the altitude of Cluster near 4 Re, the OCB at this altitude moves to a higher latitude due to the compression. Then, the magnetosphere may adjust quickly to the new pressure and the closed field line is back to normal, therefore moving the OCB back to a lower latitude. Note that S03–S09 observe a bump around 15:23 in Figure 3-3. They observe high energy ions since the northward movement of OCB pushes newly opened field lines to the higher latitude.

The comparison of our modeled results with Cluster observations are shown in Figure 3-5. The left panels show the spectrograms observed from Cluster spacecraft C4, C1, and C3. The right panels show three selected spectrograms from the simulations. The V1 is the S02 in Figure 3-3, the V2 is the virtual satellite launched between S02 and S03, and the V3 is the virtual satellite launched between S11 and S12. For the model-observation comparison, we fit the straight line, $log\,\mathrm{E} = a\mathrm{T} + b$ where E is energy, T is time, a is the slope, and b is the intercept, to the upper edge of each dispersion by using the linear least squares. The magenta lines represent the upper edges and the white lines represent the fitted lines. In each spectrogram, we

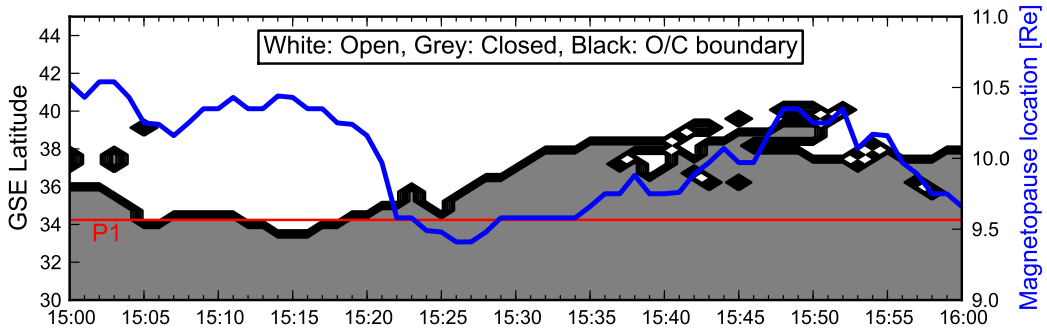

Figure 3-4: The open/closed field line boundary (the black line) along the Cluster orbit and the magnetopause location (the blue line) at the Sun-Earth line. The red line represents the P1 location.

display the highest energy of the upper edge, i.e., the highest energy of the dispersed ions, and the slope a of the fitted line.

The C4 and C1 probes pass the cusp during southward IMF, observing normally dispersed structures. The dispersion slopes in the C4 and C1 observations are $(-2.116 \pm 0.051) \times 10^{-3}$ and $(-2.128 \pm 0.029) \times 10^{-3}$, and the highest energies of the dispersed ions are about 27.61 and 28.90 keV. The V1 and V2 also observe normal dispersions, similar to the C4 and C1 observations. However, the dispersion appears a few minutes earlier than the observations and has a smaller slope. The model orbit may expose the virtual satellites to a slightly different environment than the Cluster satellites, causing these differences. The slopes of both modeled dispersions are $(-1.067 \pm 0.113) \times 10^{-3}$ and $(-1.040 \pm 0.133) \times 10^{-3}$. The highest energies of both dispersions are 32 keV.

Our model successfully reproduces normal dispersions, the distinct structures of C4 and C1 observations. This fulfills the comparison criteria (a) and (b) which we stated in section 2. The difference between the modeled and observed dispersion slopes are about a factor of 2 within the error margin, satisfying criterion (c). The

highest energies of both modeled and observed dispersions also coincide within a factor of 2, satisfying criterion (d). Since both V1 and V2 spectrograms fulfill all four criteria, we consider that the model predictions are "excellent".

The C3 probe passes the cusp after the IMF turns northward and observes an irregular ion structure. The upper edge of this dispersion is flatter than the ones in the C1 and C4 observations. The beginning of this structure shows the widening of the high flux region with the decreasing low-energy edge and the increasing high-energy edge. The virtual satellite V3 also observes an irregularly dispersed structure with a flatter upper edge than the ones in the V1 and V2 observation. The widening high-flux region is also visible at the beginning of the V3 spectrogram. These patterns satisfy the comparison criteria (a) and (b).

The slopes of both modeled and observed structures are $(-0.328 \pm 0.124) \times 10^{-3}$ and $(-0.221 \pm 0.044) \times 10^{-3}$, matching within a factor of 2 and thus satisfying criterion (c). The highest energy of the modeled dispersion, however, is 21.53 keV, more than two times higher than the highest energy of the observed dispersion, 9.24 keV. Therefore, criterion (d) is not satisfied. As three of four criteria are fulfilled without ambiguity, the model result of the C3 observation is considered to be "good".

Note that the high-energy flux bands around 10keV seen in the Cluster observations are not present in the model results. Since our model considers only ions that originate from the magnetosheath, it does not reproduce these bands, which are composed of hot magnetospheric ions.

3.2.2 28 August 2003 Case

The second case is a cusp-crossing event of Cluster on 28 August 2003. While SW/IMF conditions are quite variable, Cluster satellites(C1/C3/C4) sequentially enter the cusp and observe slightly different dispersions. This event was introduced by

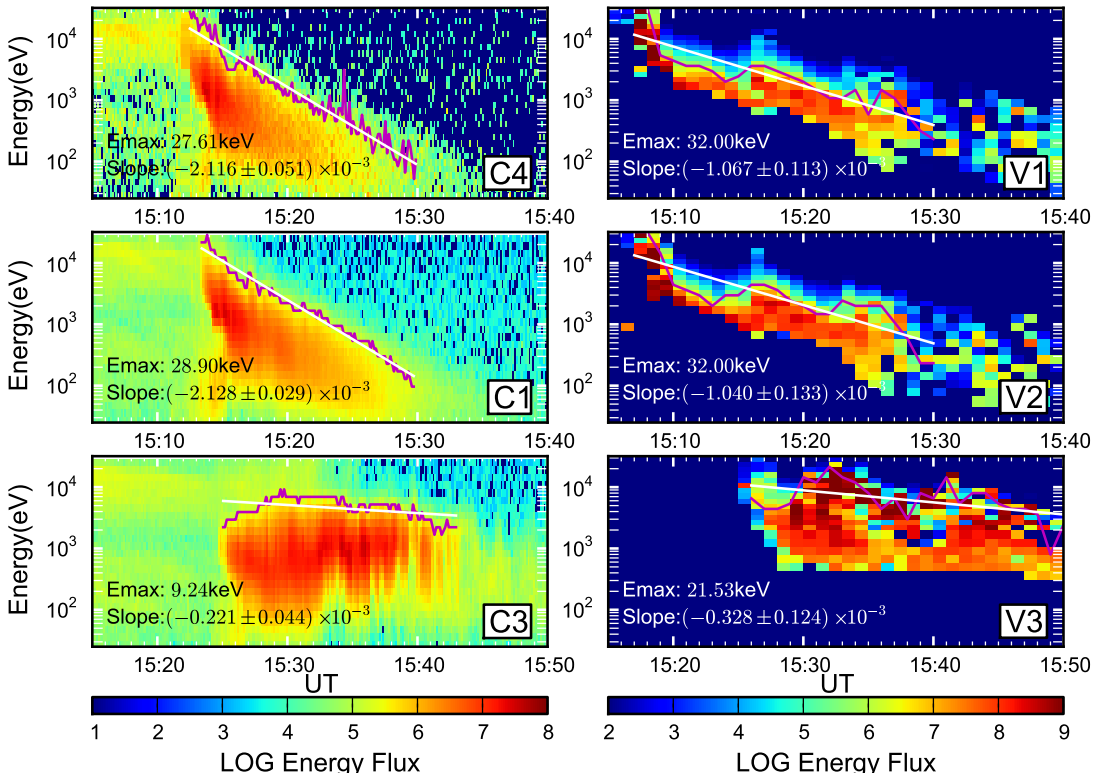

Figure 3-5: Comparison of the modeled results with Cluster observations on 23 September 2004. The magenta lines show the upper edges of dispersions and the white lines show the fitted lines to the upper edges. The highest energy of dispersed ions and the slope of the fitted line are labeled in each spectrogram.

Escoubet et al. [2008b], and we select this event to prove our model's validity and study temporal properties of these cusp structures.

The SW/IMF conditions obtained from ACE are shown in Figure 3-6 and used as an input for OpenGGCM. IMF B_z changes its direction several times during 18:55–19:15 while IMF B_x and B_y stay in the same direction. Figure 3-7 shows the Cluster orbit (the blue line) projected on a sphere of radius 5 Re. We calculate plasma pressure and open/closed field line boundary at 18:10 with the OpenGGCM results and project them on the same sphere. The Cluster satellites(C1/C3/C4) are located between the black/blue/green dots while observing the ion dispersions. Since they do not pass the OpenGGCM's cusp, the high plasma pressure region, we introduce a new orbit (the red line from P1 to P2) to model the cusp structures.

We launch a total of 15 satellites, one every minute between 18:55–19:10 along the red line, in order to find cusp structures similar to Cluster observations. Each satellite observes a cusp structure for 40 minutes. This approach is justified because there is considerable uncertainty in propagating the SW/IMF from the ACE observations $\sim$ 226Re upstream of Earth and $\sim$ 23Re off the Sun-Earth line to the inflow boundary of the simulation 24Re upstream of Earth. By launching one satellite every minute into the cusp, we can also investigate how a cusp ion structure changes in time and find out if any of these modeled ion structures compare reasonably well with the observations.

We present our results in Figure 3-8. As in the previous case, low-numbered satellites pass the cusp earlier than high-numbered satellites. Double dispersion shown in the S01-S03 spectrograms becomes one thick dispersion with a flat high-energy cutoff around 19:05 in the S04-S05 spectrograms. The S06-S08 also observe double dispersions, one at the beginning and another starting around 19:16. Then, the S09-S15 observe continuously dispersed structures with irregular high-energy cutoff.

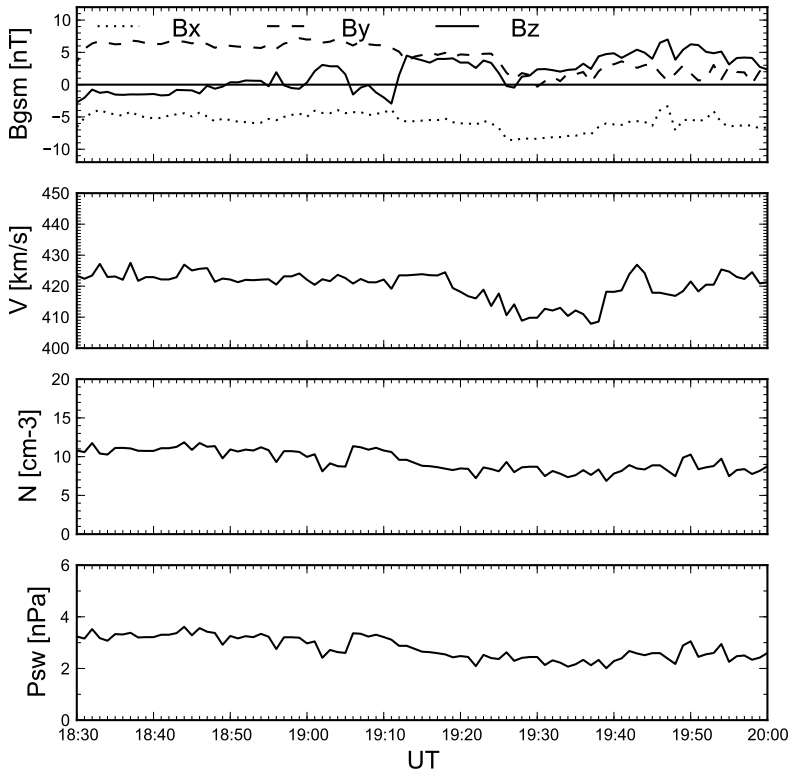

Figure 3-6: Solar wind and IMF conditions obtained from ACE on 28 August 2003. 65 minutes are added to the ACE data to account for SW/IMF propagation from ACE to the cusp.

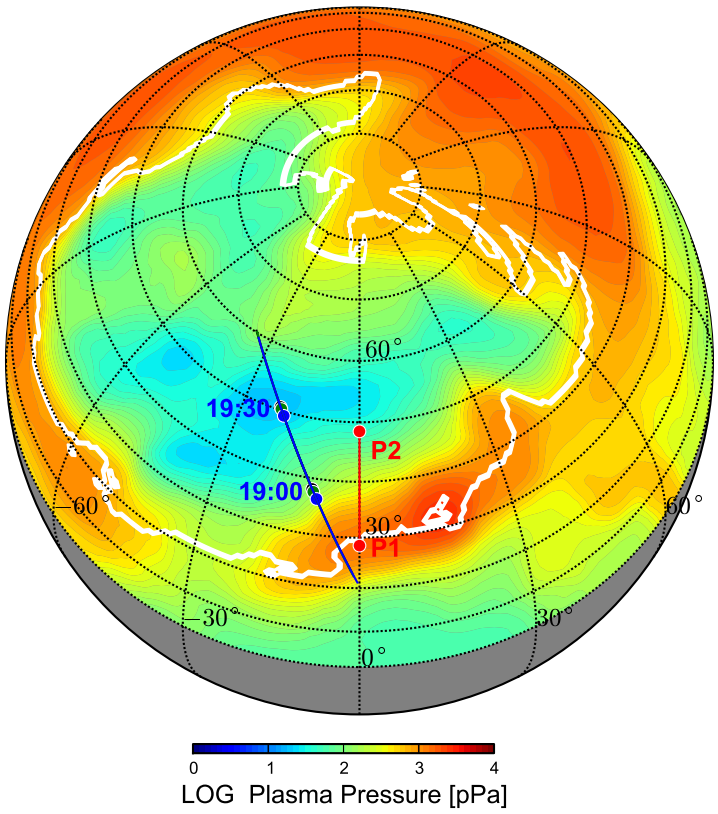

Figure 3-7: The Cluster orbit (the blue line) projected on a sphere of radius 5 Re. Plasma pressure at 19:10 (the color contour) and the open/closed field line boundary (the white line) are calculated from the OpenGGCM simulation. The Cluster C1/C3/C4 are located between the black/green/blue dots during the event. The red line between P1 and P2 is the orbit used for modeling a cusp structure.

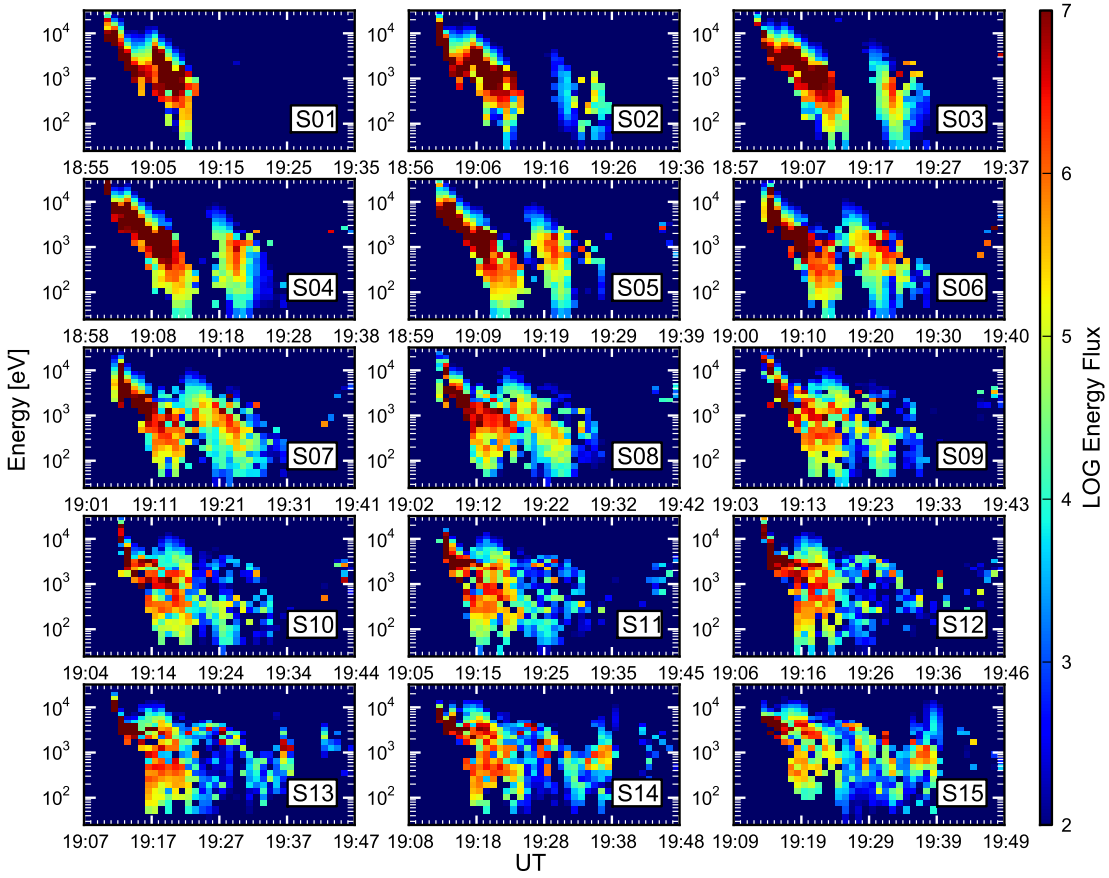

Figure 3-8: Model results of the Cluster event on 28 August 2003

To study the magnetosheath origins of cusp ions, we calculate where on the magnetosheath surface the ions penetrate. The magnetosheath surface is where we calculate PSDs. We project the ion entry points on the YZ plane as seen from the Sun in Figure 3-9 (a). To relate the origins to cusp ion structures, we color the points according to the time observed by the satellites. The first/second/third columns of Figure 3-9 (a) show the entry points of ions observed by S01/S07/S14, respectively. Then, we study how the ions enter the magnetosphere. We select two example ions and trace magnetic field lines on which each ion has been. Figure 3-9 (b) and (c) show the two ion trajectories (the black lines) and the magnetic field lines (the colored lines) calculated every minute along the trajectories. The color shows the time when each ion is on each field line.

The ions observed by S01 come mostly from the dawnside of the magnetosheath along Zgse=0 axis. Especially, the ions observed before 19:05, which compose the first dispersion of S01, have the same magnetosheath origin as the ions observed during 19:05–19:10, which compose the second dispersion of S01. We select two ions, one from each dispersion, and show the trajectories in the first column of Figure 3-9 (b) and (c). Although the ions arrive at S01 at different times, both of them pass similar open field lines caused by reconnection on the duskside of magnetopause (the magenta markers). The reconnection site is selected from Figure 3-10(a) where the magnetic configuration of the GSE equatorial plane at 19:05 is displayed on the contour of magnetic field magnitude. The reconnection appears on the duskside magnetopause where the dawnward IMF meets the duskward magnetospheric field. Ion precipitation originates from the same reconnection site at different times, indicating that double dispersions are temporal structures caused by variations of the reconnection rate on the duskside magnetopause.

The second column of Figure 3-9(a) shows that the ions observed by S07 have

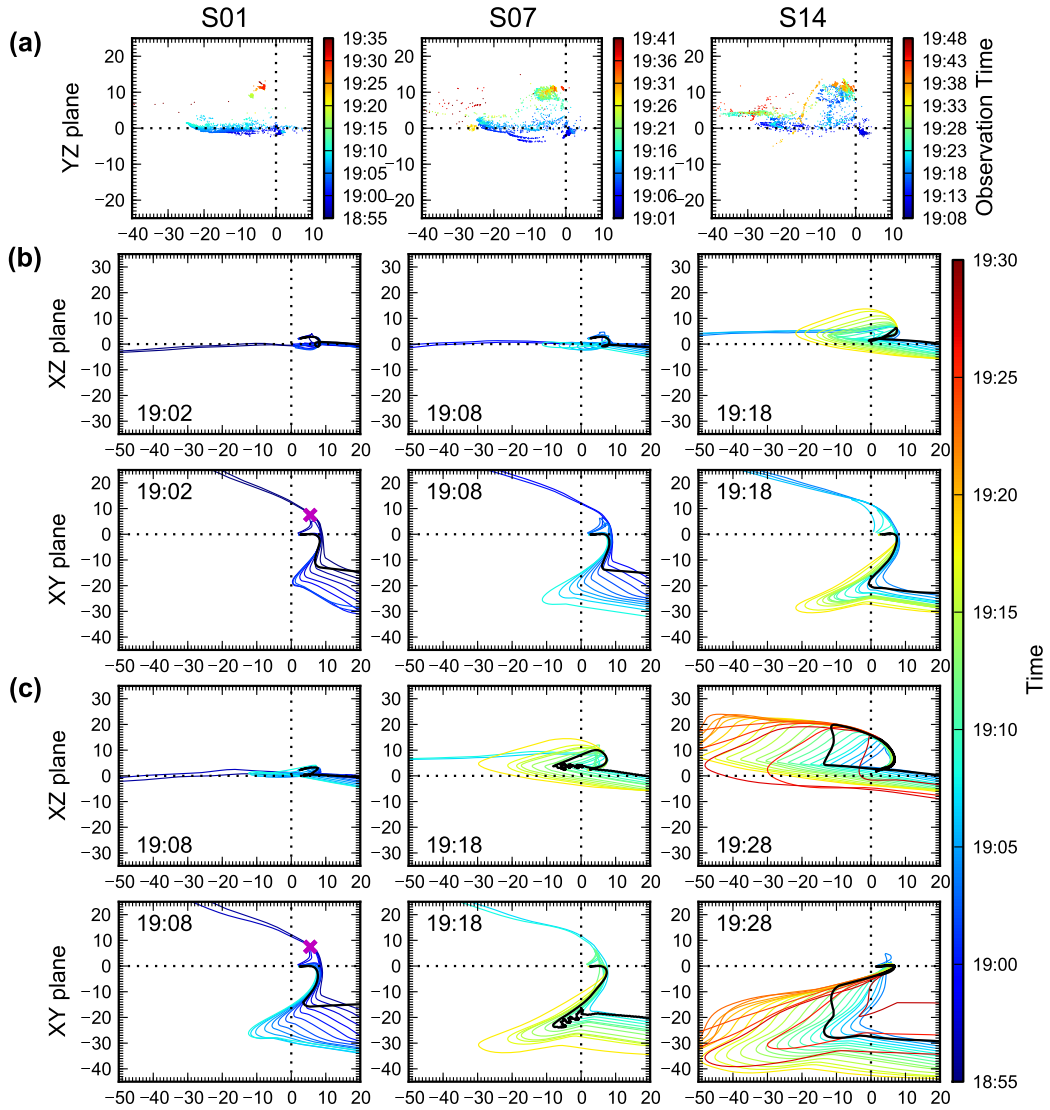

Figure 3-9: **(a)** Ion entry points on the magnetosheath surface, projected on the YZ plane as viewed from the Sun. The 1st/2nd/3rd column shows the S01/S07/S14 observations. The color represents the time when satellites observe the ions. The magenta 'x' markers represent the reconnection site shown in Figure 3-10(a). **(b),(c)** Two ion trajectories (the black lines) observed by each satellite, projected on XZ and XY planes. The colored lines are magnetic field lines calculated every minute along the ion trajectories. The printed time represents when the ion is observed by a satellite.

two major regions of origin on the magnetosheath. The ions observed before 19:16, which compose the first dispersion, are mostly from the dawnside magnetosheath along Zgse=0 axis while the ions observed after 19:16, which compose the second dispersion, are from the dawnside northern magnetosheath near Zgse=10. Two ion trajectories, one from each dispersion, are shown in the second column of Figure 3-9 (b) and (c). The ion observed at 19:08 passes similar open field lines as the ions of S01, indicating that the first dispersion of S07 is caused by reconnection on the duskside magnetopause. However, the ion observed at 19:18 precipitates to the cusp after the zigzag motion in the dawn flank of the magnetosheath.

This zigzag motion is the result of the magnetic mirror force. Figure 3-10(b) shows the magnetic configuration of the equatorial plane at 19:15 where magnetic field magnitude is color-contoured. We observe the increase of magnetic field at the sunward boundary of the dawnside magnetosheath as well as the strong magnetic field at the earthward boundary. Thus, the dawnside magnetosheath is surrounded by regions of strong magnetic field. Since the magnetic mirror force repels a particle from a strong magnetic field region, the ion observed at 19:18 moves back and forth between the two boundaries. This ion precipitates into the cusp as it moves closer to the nightside of the earthward boundary. The mirror force of this region is no longer strong enough to repel the ion because of the earth's weak magnetic field. Therefore, the second dispersion of S07 is composed of ions temporarily trapped in the dawnside magnetosheath while the sunward boundary has a strong magnetic field. The enhanced field is caused by the reformation of the bow shock as the IMF rotates at 19:10 UT (see Figure3-6) from an orientation that creates a parallel shock on the dawnside to an orientation that produces a quasi-perpendicular shock. The interaction of the IMF rotation (either a rotational or a tangential discontinuity) with the bow shock apparently creates the transient magnetic cavity in the sheath.

However, a detailed analysis of the mechanism responsible for the appearance of this strong magnetic field is beyond the scope of this dissertation.

The ions observed by S14 have various source regions on the magnetosheath, shown in the third column of Figure 3-9(a). They originate from the dawnside flank of the magnetosheath near Zgse=0 and Zgse=5 and from the dawnside of northern lobe near Zgse=10. We select two ions observed at two different latitudes by S14 to show how each ion takes a different path according to the latitude. The third columns of Figure 3-9(b) and (c) show trajectories of the two ions observed at 19:18 and 19:28. Since S14 moves from low to high latitude, the ion observed at 19:28 precipitates at higher latitude than the one observed at 19:18.

The ion arriving at high latitude reaches the nightside of the dawn flank magnetopause while the ion arriving at low latitude reaches the dayside of the magnetopause. The field lines on the nightside of the dawn magnetopause are draped over the northern magnetopause and connected to high latitudes of the cusp by the reconnection on the duskside magnetopause. Therefore, the ion observed at high latitudes takes a longer time to arrive at the cusp from the magnetosheath, and 1–2 hours of tracing time are not enough for these ions, especially low energy ions, to travel between the cusp and magnetosheath. This is why the modeled spectrogram has weak or no energy flux at low energy level near the high latitudes.

Figure 3-11 compares our model results to the Cluster observations. The left panels show the spectrograms observed from Cluster spacecraft C1, C3, and C4. The right panels show the modeled spectrograms observed from our virtual satellites S01, S04, and S14. The magenta lines represent the upper edges of dispersions and the white lines are the fitted lines to the upper edges. We also present the slopes of the fitted lines and the highest energies of the dispersed ions in the spectrograms.

S01 observes double dispersions while S04 observes one broad single dispersion.

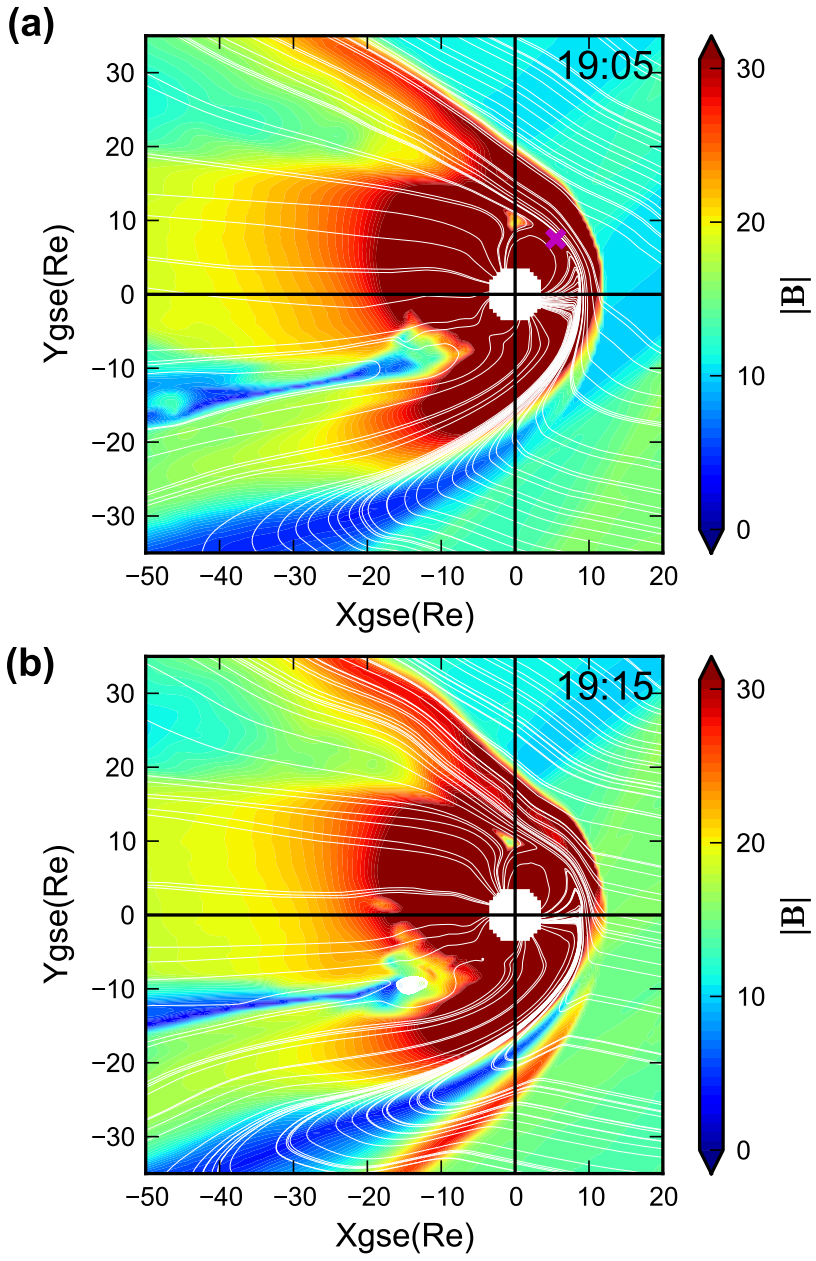

Figure 3-10: Magnetic configuration of the GSE equatorial plane (a) at UT 19:05 and (b) at UT 19:15. The color contour represents magnitude of the magnetic field, and the magenta 'x' marker in (a) represents the reconnection site on the duskside magnetopause.

These patterns match the C1 and C3 observations. Our results in Figure 3-9 suggest that double dispersions are temporal structures caused by various reconnection rates on the duskside flank of magnetopause. Thus, the single thick dispersion shown in the C3 spectrogram may appear since C3 observes the second dispersion, caused by increased reconnection rate, right after observing the first dispersion at the entry into the cusp. The dispersion direction in the modeled spectrograms agrees with the one in the observations, fulfilling comparison criterion (a). However, our model does not produce flux at low energy as seen in the observations because of limited tracing time. Therefore, we consider that the model predictions fulfill criterion (b) with some ambiguity.

The slopes of the modeled double dispersions are $(-2.908 \pm 0.376) \times 10^{-3}$ and $(-2.774 \pm 0.108) \times 10^{-3}$, coinciding to the slopes of the observed double dispersions $(-4.094 \pm 0.591) \times 10^{-3}$ and $(-2.559 \pm 0.266) \times 10^{-3}$ within a factor of 2. The slopes of the modeled and observed single dispersions are $(-0.684 \pm 0.093) \times 10^{-3}$ and $(-0.839 \pm 0.045) \times 10^{-3}$, also matching within a factor of 2. Therefore, the S01 and S04 spectrograms fulfill criterion (c). The highest energies of double dispersions are 32.0 and 8.0 keV for the model and 6.94 and 3.93 keV for the observation. The highest energies of single dispersions are 32.0 keV for the model and 9.24 keV for the observation. All the highest energies of the modeled dispersions are more than two times higher than those of the observed dispersions, thus failing criterion (d). Since the model predictions on the C1 and C3 observations fulfill only 3 criteria with some ambiguity, the model results are considered "satisfactory".

The bottom panels in Figure 3-11 show the observations of C4 and S14. S14 observes continuous normal dispersion with a wavy high-energy cutoff similar to the one that C4 observes. Therefore, the model prediction fulfills comparison criteria (a) and (b). The wavy cutoff may be a result of fast convection speed of open field lines

during intermittent reconnection on the duskside magnetopause. Thus, S14 observes a slight increase of high energy cutoffs when S14 is connected to newer open field lines, which have more ions of high energy. OpenGGCM may not produce intermittent reconnection at the same time as in reality, and therefore S14 observes the increase of high energy cutoff at different times than C4.

The dispersion slopes in the S14 and C4 spectrograms are $(-0.684 \pm 0.093) \times 10^{-3}$ and $(-0.839 \pm 0.0045) \times 10^{-3}$, satisfying criterion (c). However, the highest energies of the modeled and observed dispersions are 9.75 and 4.0 keV, and therefore fails criterion (d). Since three of all four criteria are fulfilled without ambiguity, the model result of S14 is considered "good".

3.2.3 25 August 1998 Case

The third case is a cusp-crossing event by Polar and FAST on 25 August 1998. Polar and FAST cross the northern cusp during stable solar wind conditions, and observe similar stepped dispersions, although they enter the cusp 27 minutes apart. *Trattner et al.* [2002] concluded that the stepped structure is a spatial structure, caused by the spatial variation of reconnection. In this case study, we reproduce the cusp structure observed by Polar and investigate whether it is spatial or temporal.

Figure 3-12 shows SW/IMF conditions obtained from WIND. The black bars in the top panel represent the time when Polar and FAST reside in the low-latitude cusp. Both satellites pass the cusp during southward and duskward IMF. Figure 3-13 shows the Polar location (the blue lines) projected on spheres of radius 5 Re. The color contours and white lines represent plasma pressures and open/closed field line boundaries at 00:15 and 00:25, calculated from the OpenGGCM simulation.

The OpenGGCM cusp, a region of high plasma pressure, is located in the vicinity of local noon at 00:15, and moves to the duskside around 15° GSE longitude at 00:25.

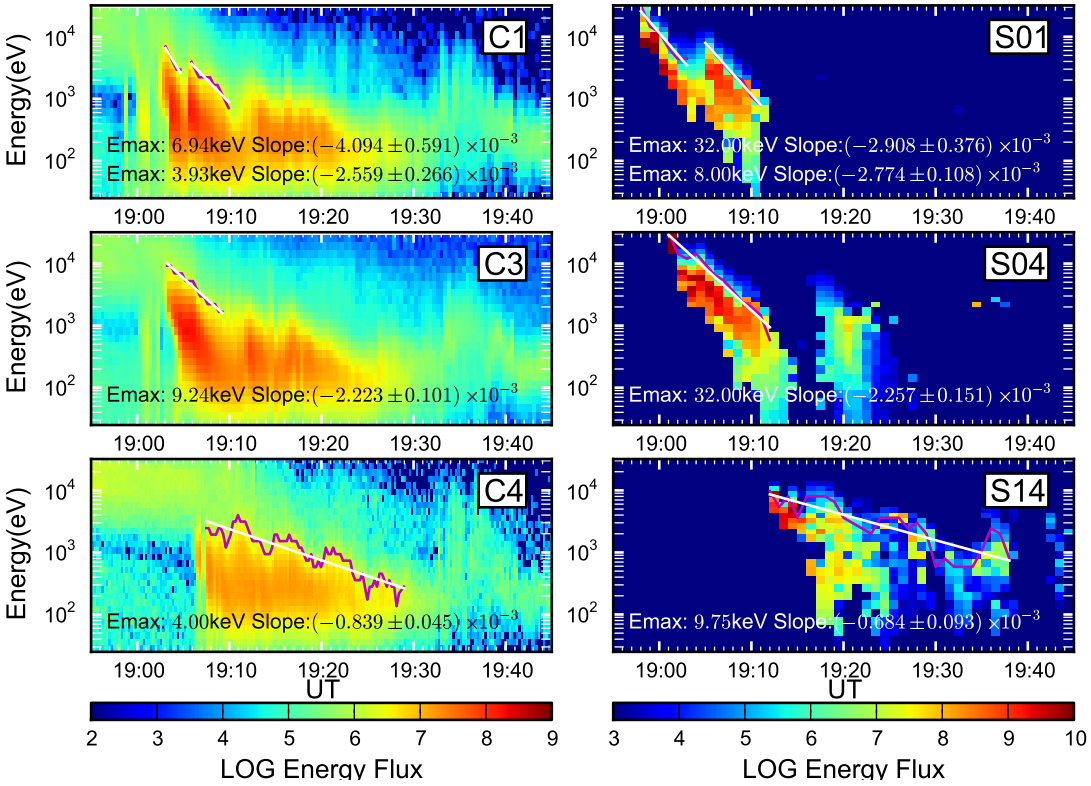

Figure 3-11: Comparison of the modeled results with Cluster observations on 28 August 2003. The magenta and white lines are the upper edges of dispersions and the fitted lines to the upper edges. The highest energies of dispersions and the slopes of the fitted lines are also displayed.

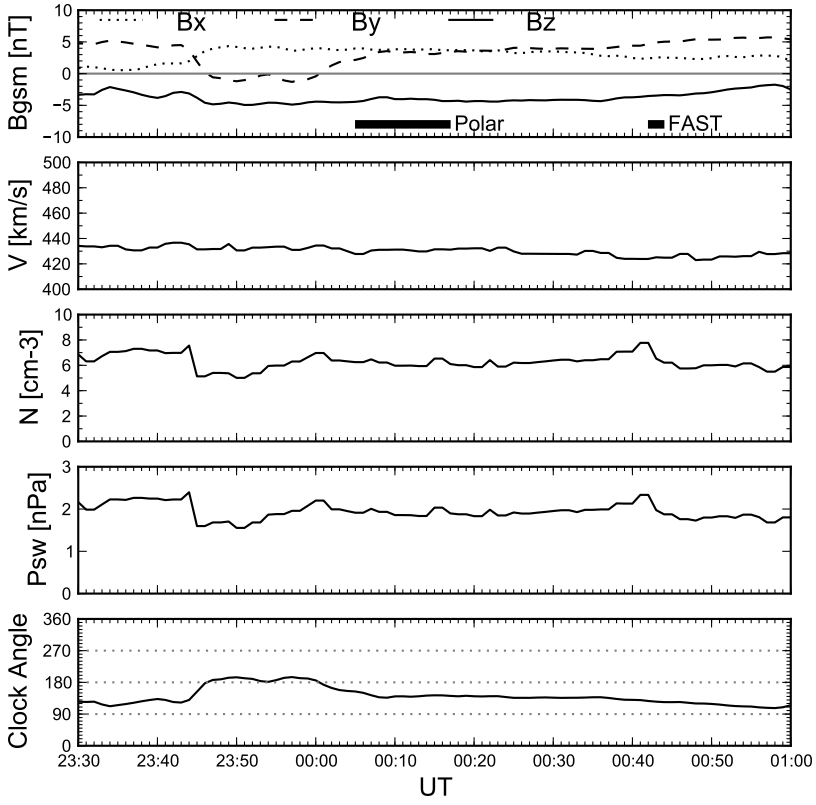

Figure 3-12: Solar wind and IMF conditions obtained from WIND spacecraft on 25 August 1998. Horizontal bars in the top panel represent the time when FAST/Polar pass the low-latitude cusp. 27 minutes are added to the WIND data to account for the propagation from WIND to the magnetopause.

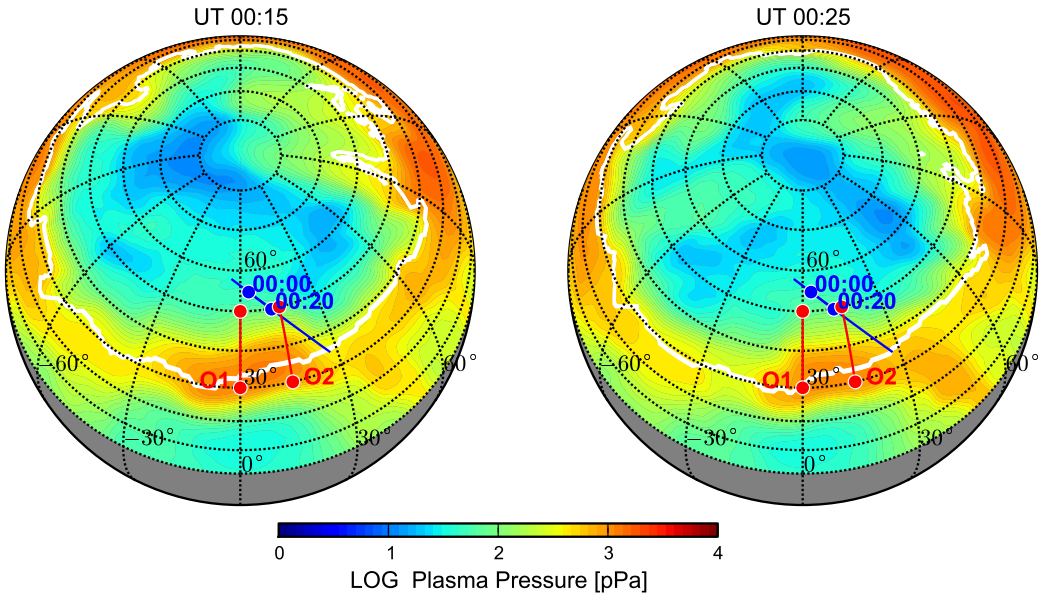

Figure 3-13: Polar orbit (the blue line) projected on the spheres of radius 5 Re. The plasma pressures (the color contour) and the open/closed field line boundaries (the white line) at 00:15 and 00:25 are obtained from the OpenGGCM simulation. Polar is located between the blue dots during the event. The red lines O1 and O2 are the orbits for our virtual satellites.

Then, the cusp stays on the duskside until 01:00. For this event, Polar and FAST observe the stepped dispersion at two different magnetic local times, 13:43 MLT and 14:57 MLT. This finding may relate to cusp motion. Since Polar does not pass through the modeled cusp, we introduce two orbits, O1 and O2, which interact with the cusp centers at 00:15 and 00:25, respectively. The O1 and O2 pass along the noon-midnight meridian and a longitudinal line at 15° GSE longitude, respectively. The altitudes of both orbits are 4 Re, i.e., the Polar altitude.

A total of five virtual satellites are introduced: one for comparison with the Polar observation, and the rest for investigating whether the dispersed ion structure is of spatial or temporal nature. The first satellite (S1) passes the cusp along the O1 orbit during 00:20–00:05. Since the cusp during this time is located near the local noon, we introduce O1 as S1's orbit. S1's speed is set at around 4km/s, to correspond to Polar's speed. To increase the resolution of the spectrogram, we launch ions every 30 seconds in this case. The spectrogram obtained from the S1 orbit is compared with the Polar observation in order to assess our model's validity.

The remaining satellites (S2–S5) pass the cusp at 00:15, 00:25, 00:35, and 00:45, respectively, with infinite speed. Thus, these satellites provide spatial snapshots at these times, removing all temporal variations. Since the cusp center moves from noon to the dusk around 00:20, we select O1 as S2's orbit and O2 as the orbits of S3–S5. FAST observed a stepped structure during 00:42–00:44, 27 minutes after Polar observed a similar structure. If the structure is purely spatial, our virtual satellites S2–S5 should observe essentially the same cusp ion structures as S1 during 00:15–00:45.

Figure 3-14 compares the Polar observation and model results (S1–S5). The three vertical lines separate three steps in the cusp ion structures. We display structures backward in time, i.e., increasing in latitude, as they were displayed in Figure 9 of

Trattner et al. [2002]. The first two spectrograms on the left side show Polar observation and our model prediction for the virtual satellite S1. We use these spectrograms for the model-observation comparison. The magenta and white lines represent the upper edges of the dispersions and the lines fitted to the upper edges. The highest energies of the dispersed ions and the slopes of the fitted lines are also presented.

Although the orbit O1 is quite different from the Polar orbit, S1 observes continuously dispersed structures with high-energy ion injection in the first step, a wide high-flux region in the second step, and a rather flat dispersion in the third step. This result matches well with the Polar observation, and thus fulfills comparison criteria (a) and (b). The slopes of observed and modeled dispersions agree within a factor of 2, satisfying criterion (c). However, the highest energies of both dispersed ions do not coincide within a factor of 2, failing criterion (d). By fulfilling three criteria without ambiguity, the model prediction is considered "good".

The remaining spectrograms are used to analyze whether the stepped dispersion is temporal or spatial. The spectrogram S2, which is the cusp snapshot at 00:15, shows very similar stepped structures to S1. After the cusp moves to the dusk, S3–S5 pass the cusp at 00:25, 00:35, and 00:45, respectively. Although their cusp structures are not quite the same as that of the S1 observation, the key properties of each step are still observed. The energy of cusp ions continuously decreases through the whole stepped structure as the latitude increases, and the second step has wider high-flux region than the first step. This stepped structure remains steady for 30 minutes between 00:15–00:45, supporting the conclusion of *Trattner et al.* [2002] that the stepped dispersion is spatial.

Figure 3-15, however, suggests that the stepped dispersion is not only spatial but also temporal. To understand the precipitating patterns of cusp ions, we examine the magnetosheath origins of the ions by calculating ion entry points on the magne-

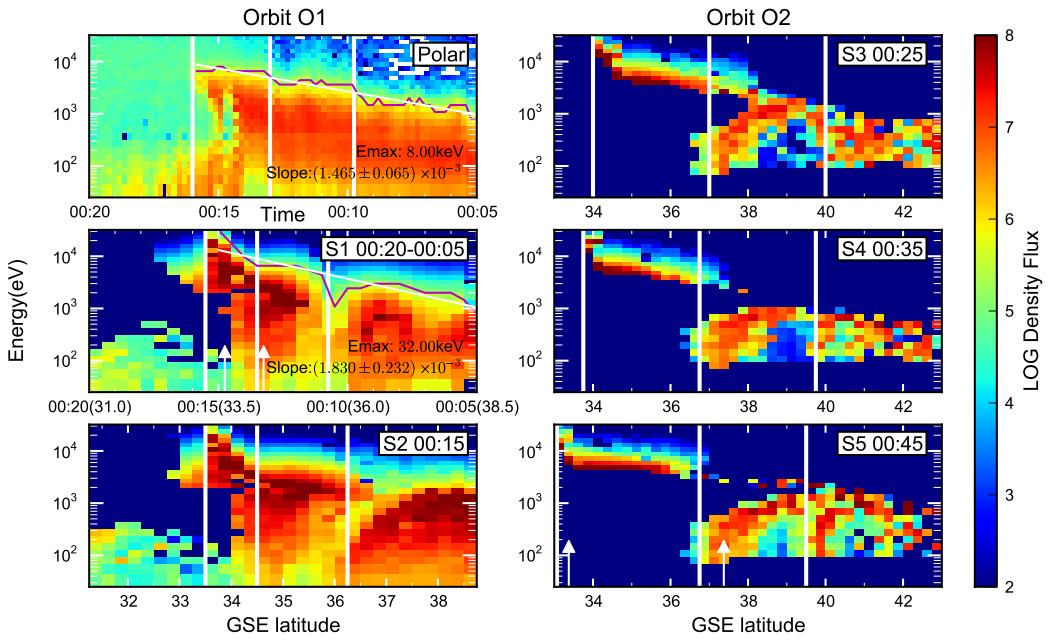

Figure 3-14: Comparison of the modeled results with the Polar observation on 25 August 1998. The time next to the satellite number represents the time when the satellite passes the cusp. The white bars separate the three distinct structures and the white arrows represent the selected positions for the ion trajectories in Figure 3-15(b). The magenta and white lines in the Polar and S01 spectrograms represent the upper edges of dispersions and the fitted lines to the edges. The highest energies of dispersions and the slopes of the fitted lines are also displayed in the two spectrograms.

tosheath surface, which is located a few tenths of an Re outside the magnetopause where we calculated the PSDs. Figure 3-15(a) shows the projection of these points on the YZ plane as seen from the Sun. The entry points in the top panel are colored according to the latitude where ions are observed in order to relate the points with the stepped dispersion. The entry points in the middle and bottom panels are colored according to the ion energy at the cusp and the time when ions penetrate the magnetosheath surface, respectively, in order to distinguish the magnetosheath source regions.

Two magnetosheath source regions are mainly observed and easily distinguishable by the colors of entry points in the middle and bottom panels of Figure 3-15(a). We point to the source regions with the magenta arrows in Figure 3-15(a). One source region is located in the dawnside magnetosheath and moves to local noon as the satellite orbit changes from O1 to O2 in order to pass the cusp center. Another source region is located in the duskside magnetosheath, and moves further into the duskside of the magnetosheath as the orbit changes. The ions from the dawnside source region are of high energy and precipitate mostly at the low and mid latitudes of the cusp, where the first and second steps are observed. The ions from the duskside source region are of low energy and precipitate at the mid and high latitudes of the cusp where the second and third steps are observed.

Ion entry times on the magnetosheath surface are also different depending on the source regions. While ions from the duskside source region enter the magnetosheath surface mostly before 00:10, ions from the dawnside source region have different entry times according to the satellites, i.e., about 00:10, 00:13, 00:22, 00:33, and 00:43 for S1–S5, respectively. Thus, there are two reconnection sites that produce these ions. The first site is located on the duskside magnetopause and disappears around 00:10. The next site is located on the dawnside magnetopause near the local noon, and is constantly active since 00:10.

To study how ions from these two different source regions penetrate the magnetopause, we select two typical ions, one from each source, and show their trajectories with magnetic field lines they have passed. For simplicity, we display the results from only two satellites, S1 and S5, in Figure 3-15(b). The top panels show the trajectories of ions from the dawnside source region, and the bottom panels show the trajectories of ions from the duskside source region. The black lines are the trajectories projected on XZ and YZ planes. The colored lines are the magnetic field lines, and the color

represents the time when each ion is on each of the field lines. Each plot is labeled with the satellite number and the observed latitude.

All ions from both source regions enter the magnetopause via kinked open field lines caused by subsolar reconnection. However, their trajectories are aligned with different IMF clock angles depending on the magnetosheath source regions. The trajectories of ions from the duskside source region are aligned with about 180° clock angle, while the trajectories of ions from the dawnside source region are aligned with 140° clock angle. Note that the IMF clock angle changes from 190° to 140° around 00:02 (See Figure 3-12). The two different magnetosheath source regions relate to this IMF clock angle change. The open field lines connect the northern cusp to the duskside magnetosheath during 190° clock angle and the dawnside magnetosheath during 140° clock angle. Therefore, the magnetosheath source region changes from dusk to dawn as the IMF clock angle changes from 190° to 140°.

The dawnside source region of the S3–S5 is located near local noon, not the dawnside magnetosheath. However, this region is still located on the dawnside of another source region, the duskside magnetosheath, showing that the magnetosheath source region changes as the IMF clock angle changes. The bottom panels of Figure 3-15(a) show that ions from the duskside source region still penetrate the magnetosheath surface until 00:10 after the IMF clock angle change at 00:02. This is probably because the magnetosphere takes time to adjust to the IMF change.

The stepped dispersion observed by Polar is therefore caused by two subsolar reconnection sites before and after the IMF clock angle change. One subsolar reconnection site is located on the duskside magnetopause during 190° IMF clock angle and is ceased around 00:10. This reconnection causes ion precipitation from the duskside magnetosheath to the mid and high latitudes of the cusp, producing the low energy part of the second step and most of the third steps. Another subsolar reconnection

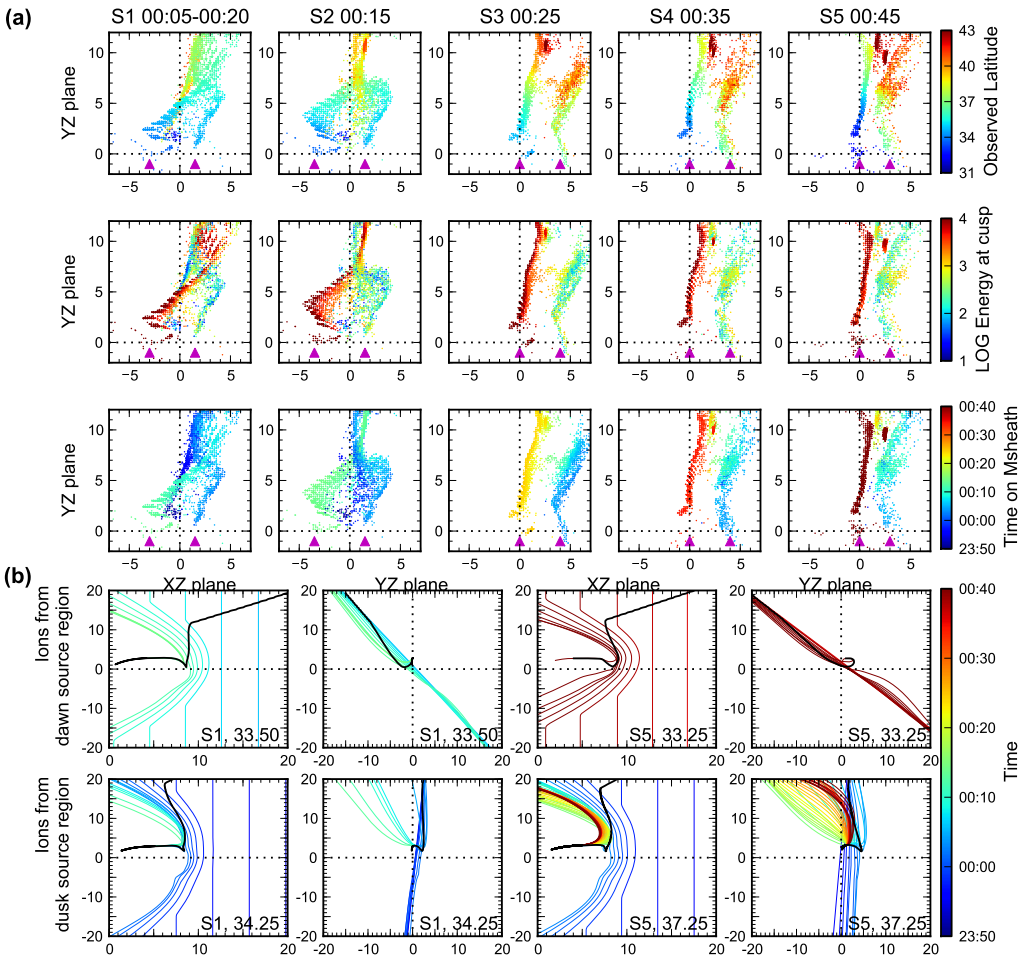

Figure 3-15: (a) Ion entry points on the magnetosheath surface, projected on the YZ plane as viewed from the Sun. The 1st to 5th columns show the S1–S5 observations, respectively. The color represents the latitude where the ions are observed, the ion energy at the cusp, and the time when it penetrates the magnetosheath surface. The magenta arrows point to the two main magnetosheath source regions. (b) Two typical trajectories of ions, one from each magnetosheath region, projected on the XZ and XY planes. The ions in the top and bottom panels originate from the dawn and dusk source regions, respectively. The left two columns show the ion trajectories observed from S1, and the right two columns shows the ones observed from S5. The black lines are ion trajectories and the colored lines are magnetic field lines which each ion has passed. The color represents the time when the ion passes each field line.

site is located on the dawnside magnetopause near the local noon during 140° IMF clock angle, and consistently active since 00:10. This reconnection causes ion precipitation from both the dawnside magnetosheath and the local noon to the low and mid latitudes of the cusp, producing most of the first step and the high energy part of the second step.

This stepped dispersion is a temporal structure in that the two subsolar reconnection sites appear at different times by the change of the IMF clock angle. It is also a spatial structure in that ions from both reconnection sites are consistently observed for 30 minutes by our virtual satellites. Ions originating from the ceased reconnection are low energy, i.e., slow ions which take a long time to travel from the magnetopause to the cusp. This is why our satellites observe these ions for 30 minutes although the reconnection is already ceased. Thus, this stepped dispersion is of both temporal and spatial nature.

3.3 Summary and Conclusion

In this chapter, we demonstrated our model's validity by reconstructing cusp ion structures during three cusp-crossing events of the Cluster and Polar satellites. We defined four comparison criteria: (a) the modeled dispersion is in the correct direction, (b) the model reproduces the distinct structures visible in the observation, (c) the slope of modeled dispersion matches with the slope of observed dispersion within a factor of 2, and (d) the highest energies of the modeled and observed dispersions coincide within a factor of 2. We assessed the model predictions as being "excellent", "good", "satisfactory", or "non satisfactory" based on the number of fulfilled criteria. The summary of the model assessment is shown in Table 3.1. Despite the difficulty of locating satellites in the OpenGGCM's cusp, our model produced two excellent, three good, and two satisfactory results.

Table 3.1: Summary of the model-observation comparison. "o" means that the model result fulfills the comparison criterion, "△" means that the model result satisfies the criterion with some ambiguity, and "x" means that the model result does not fulfill the criterion. "E", "G", and "S" represents that the model prediction is excellent, good, and satisfactory.

Comparison criteria	2004Sep23			2003Aug28			1998Aug25
	C4	C1	C3	C1	C3	C4	Polar
a. dispersion in a correct direction	o	o	o	o	o	o	o
b. existence of distinct structures	o	o	o	△	△	o	o
c. the slope of dispersion	o	o	o	o	o	o	o
d. the highest energy of dispersed ions	o	o	x	x	x	x	x
Comparison result	E	E	G	S	S	G	G

The comparison result showed that combining a global fluid model with a test particle tracer and PSD reconstruction is a viable approach. Furthermore, we covered a wide range of possible ion structures (i.e., normal dispersion, reverse dispersion, double dispersions, and stepped dispersion). This gave us confidence that the model includes all the essential physics and can be used for further studies of the properties of cusp ion structures and their relation to magnetopause processes.

We used these three case studies to shed light on the physical processes that lead to observed ion dispersion. Specifically, we addressed the question of whether dispersed structures are of temporal or spatial nature and where ions originate. We found that :

1. In the 23 September 2004 case, the bump around 15:23 observed by several virtual satellites is a temporal structure caused by the sudden increase of solar wind pressure at 15:23.

2. In the 28 August 2003 case, the double dispersions in the C1 observation are temporal structures caused by different reconnection rates on the duskside flank of magnetopause.

3. In the 25 August 1998 case, the stepped dispersion observed by Polar is not only temporal but also spatial. This is because two subsolar reconnection sites appear at different times by the temporal change of the IMF clock angle, and because both sites consistently produce ion precipitation for 30 minutes.

From the detailed study of ion trajectories, we also found that:

4. Although reconnection is the cause of the ions entering the cusp, most of them cross the magnetopause far from the reconnection site, even in the other hemisphere. In the 28 August 2003 case, the double dispersions observed by S01 are the result of reconnection on the duskside magnetopause. However, ions composing double dispersions are mostly from the dawnside magnetosheath. In the 25 August 1998 case, the stepped dispersion is the result of two different subsolar reconnection sites, but most ions precipitate from the northern magnetosheath, away from the equatorial plane where the reconnection sites are located.

5. In addition to dayside reconnection, the magnetic configuration of the magnetosheath itself can cause energy dispersion in the cusp ion structure. In the 28 August 2003 case, the second dispersion observed by S07 is composed of ions temporarily trapped in the dawn flank of the magnetosheath because of a local minimum in magnetic field strength. The sunward boundary of the dawnside magnetosheath has strong magnetic field strength around 19:15, and therefore, ions move back and forth between the earthward and sunward boundaries of the magnetosheath until they reach the nightside of the earthward boundary where the magnetic field is no longer strong enough to repel them.

Chapter 4

Cusp structures and their relation to magnetopause processes during four different IMF clock angles

4.1 Introduction

We have developed a new model for cusp ion structures and tested its validity by comparing the model's predictions with satellite observations. We also have shown our model's ability to investigate the relation of observed cusp structures with dayside magnetopause processes. Motivated by these results, this chapter focuses on the general relation between cusp ion structures and dayside reconnection during four different IMF clock angles, 0°, 60°, 120°, and 180°.

Section 2 discusses the details of the OpenGGCM simulations, and section 3 introduces how to determine the magnetopause location inside OpenGGCM. Later in this chapter, this magnetopause location will be used to investigate reconnection patterns. Section 4 introduces OpenGGCM's cusp, and presents various cusp structures obtained by our virtual satellites that cross the cusp center. Section 5 investigates the relation between cusp structures and dayside reconnection. Section 6 summarize our results and discusses our conclusion.

4.2 The OpenGGCM simulation

We perform a total of four OpenGGCM simulations with four different IMF clock angles of 0°, 60°, 120°, and 180°. In each simulation, we first introduce due southward IMF for at least 2 hours, and then input the new IMF clock angle. Since we focus only on a general cusp ion structure caused by each IMF condition, we keep the other solar wind parameters constant, avoiding undesired magnetopause activities that variance in these parameters may produce. The following solar wind conditions are introduced equally to the four OpenGGCM runs:

$$\text{Dipole tilt} = 0^\circ,$$
$$N = 6.6/cm^3, P = 10.0pPa,$$
$$V_x = -450.0km/s, V_y = V_z = 0,$$
$$B_x = 0., |B| = 5nT$$

where N, P, V_x, V_y and V_z are solar wind number density, plasma pressure, and velocity in GSE coordinate. B_x and $|B|$ are IMF B_x in GSE coordinates and IMF magnitude. The above parameters stay constant for the duration of each simulation. IMF B_y and B_z are the only parameters that vary among the four OpenGGCM runs.

Figure 4-1 shows the magnetic configuration of the dayside magnetosphere in the noon-midnight meridian plane. The color contour and the white lines represent plasma number density and magnetic field lines obtained from the OpenGGCM simulations. We also display the magnetopause location (the black lines) and its standoff distance (D_{mp}) in each panel. The top panels show the magnetic configuration during 0° and 60° IMF clock angles. The bottom panels show the configuration during 120° and 180° IMF clock angles.

When solar wind approaches the Earth, it meets the bowshock where the sudden increase of density occurs. The solar wind plasma is slowed, compressed, and heated

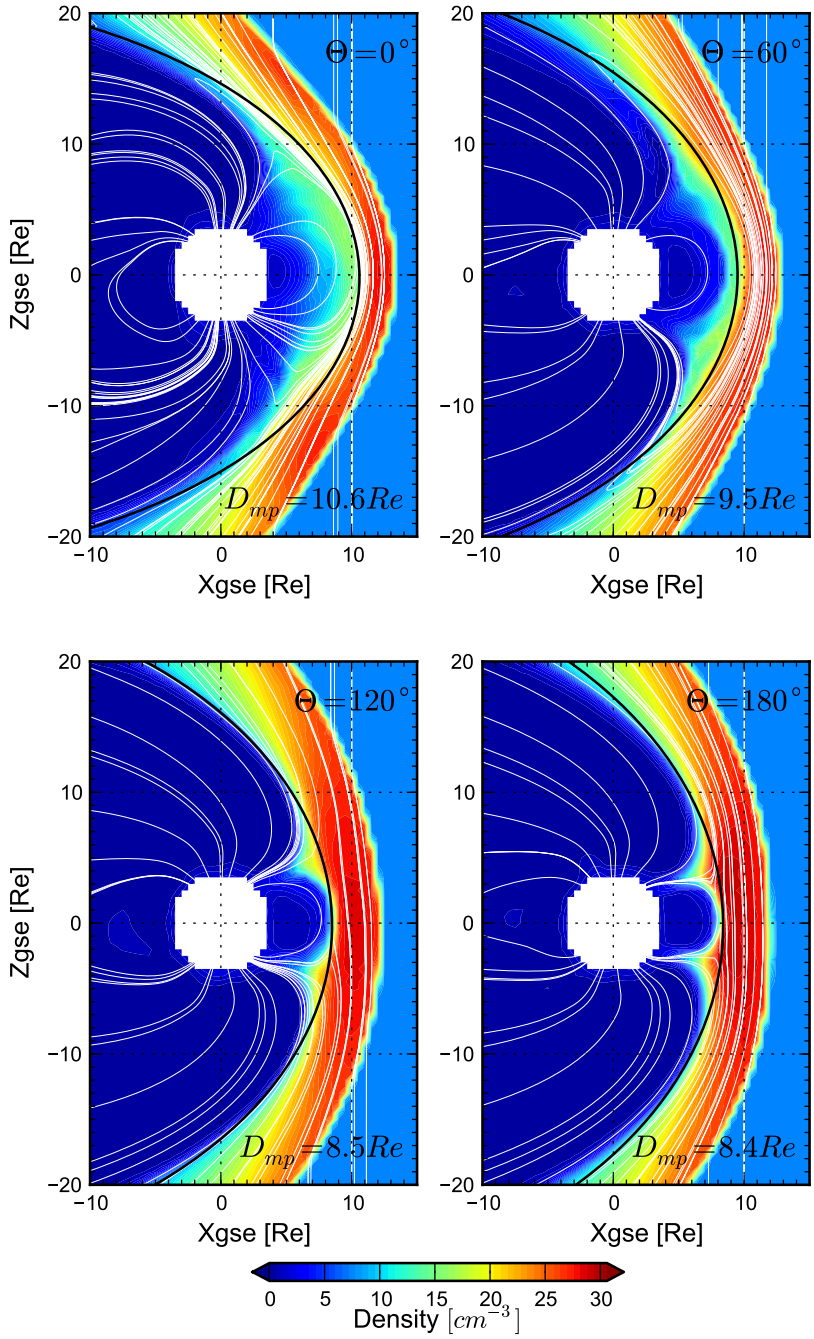

Figure 4-1: Magnetic configuration of the dayside magnetosphere on the noon-midnight meridian plane during four different IMF clock angles (Θ). The color contour represents number density, the white lines are magnetic field lines, and the black lines show the magnetopause location. D_{mp} represents the standoff distance of the magnetopause.

at this location, composing the magnetosheath (the high density region between the bowshock and the magnetopause). The low density region behind the magnetopause is the magnetosphere. Note that the magnetopause standoff distance (D_{mp}) decreases during southward IMF. This coincides with the satellite observations [*Aubry et al.*, 1970; *Fairfield*, 1971; *Maezawa*, 1974; *Formisano et al.*, 1979; *Rijnbeek et al.*, 1984]. There are many theories about the inward movement of the magnetopause [*Hill and Rasbach*, 1975; *Maltsev and Lyatsky*, 1975; *Voigt*, 1986; *Sibeck et al.*, 1991]. One of them is that the internal magnetospheric processes during southward IMF, such as increases of cross-tail current and region 1 Birkeland current, weaken dayside magnetic fields. To maintain the balance between the solar wind dynamic pressure and the Earth's magnetic field pressure, the magnetopause moves earthward.

Magnetic field topology also depends on IMF conditions. Magnetic reconnection happens near the subsolar location during southward IMF and near the lobe region (i.e., the high-latitudes of magnetopause) during northward IMF, creating kinked open field lines near the reconnection sites. OpenGGCM produces kinked field lines near subsolar region during southward IMF and near high-latitude magnetopause during northward IMF, which agrees with our understanding.

4.3 The magnetopause location in the OpenGGCM model

In order to study magnetopause activities that cause various cusp structures, we first need to determine the magnetopause location. In the previous chapters, we have fitted the magnetopause to a paraboloid. However, the paraboloid becomes so wide on the nightside that the fitted magnetopause in this region is located away from the actual location of the OpenGGCM's magnetopause. To obtain a more accurate magnetopause location, we use an ellipsoid fitting in this chapter. This section introduces the detailed method.

We first define an approximate location of the magnetopause by tracing streamlines from the upstream solar wind region to the downstream magnetotail as in *Palmroth et al.* [2003]. Since the streamlines encompass the magnetosphere, the void region of the streamlines is the magnetosphere and the outer boundary of the void is the magnetopause. We introduce a set of streamlines at $X_{gse} = 20R_E$. They are located every 0.5 Re in the YZ plane whose range is $[-45R_E \leq Y_{gse} \leq 45R_E]$ and $[-45R_E \leq Z_{gse} \leq 45R_E]$. We integrate the streamline locations with 0.5 Re step in the $-X_{gse}$ direction from 20 R_E to –30 R_E, and at each step, we calculate the minimum distance of these streamlines from the X_{gse} axis (i.e., the void size). If the void size becomes larger than 1 Re, we start looking for the magnetopause location. We divide each YZ plane into 36 sections according to their azimuthal angle. Thus, each section covers 10° azimuthal angle. To calculate the magnetopause location at each section, we ignore the first three lowest distances of the streamlines, and average the next four lowest distances. We neglect the first three lowest values because some of streamlines travel into the magnetosphere. The average distances we calculated at each azimuthal section is chosen as the magnetopause location, which we refer to as "streamline magnetopause".

We then define a more accurate magnetopause location by finding the maximum current density locations near the streamline magnetopause. The strong current layer develops on the magnetopause by magnetic shear between the IMF and the Earth's magnetic field. After the current is produced, the $\mathbf{J} \times \mathbf{B}$ force goes into effect and keeps solar wind plasma away from the magnetopause, protecting the magnetosphere. We use this strong magnetopause current to define the OpenGGCM's magnetopause. To avoid the bowshock current and the high current density region inside the magnetosphere, we locate two ellipsoids a few R_E inside and outside of the streamline magnetopause, and search between them to find the location at which current density

becomes maximum. The resultant magnetopause is referred to the "current-density magnetopause".

Finally, we calculate a smooth magnetopause by fitting the current-density magnetopause to the ellipsoid equation:

$$\frac{(x-x_0)^2}{a^2}+\frac{(y-y_0)^2}{b^2}+\frac{(z-z_0)^2}{c^2}=1 \tag{4.1}$$

where the center of the ellipsoid is located at (x_0, y_0, z_0), and the semi-axes are the length of a, b, and c. X_0 is set to be -30R_E, which is the downstream boundary of streamline calculation. In order to obtain the other ellipsoid parameters, we project the current-density magnetopause on the XY and XZ planes, and fit its outer boundary to the corresponding ellipsoid equation on each plane. The obtained magnetopause is referred to as the "ellipsoid magnetopause". The black lines in Figure 4-1 show the ellipsoid magnetopause during four different IMF conditions. We define the magnetosheath surface to be a few R_E outside of the ellipsoid magnetopause, and choose the ions reaching the surface to construct a cusp structure.

4.4 Cusp ion structures

In this section, we locate the OpenGGCM's cusp during four different IMF clock angles, and select the virtual satellite orbits that cross the cusp center. We then display cusp ion structures obtained from the OpenGGCM-LTPT model.

Since we focus on the mid-altitude cusp where dispersed ion signatures are observed, we search for the cusp location at the altitude of 4 R_E. Figure 4-2 displays the OpenGGCM's cusp at this altitude. The top panels show the cusp locations during 0° and 60° IMF clock angles, and the bottom panels show the location during 120° and 180° IMF clock angles. The color contour represents plasma pressure obtained from OpenGGCM at the altitude of 4 R_E, and the white lines are open/closed field line boundaries calculated at this altitude.

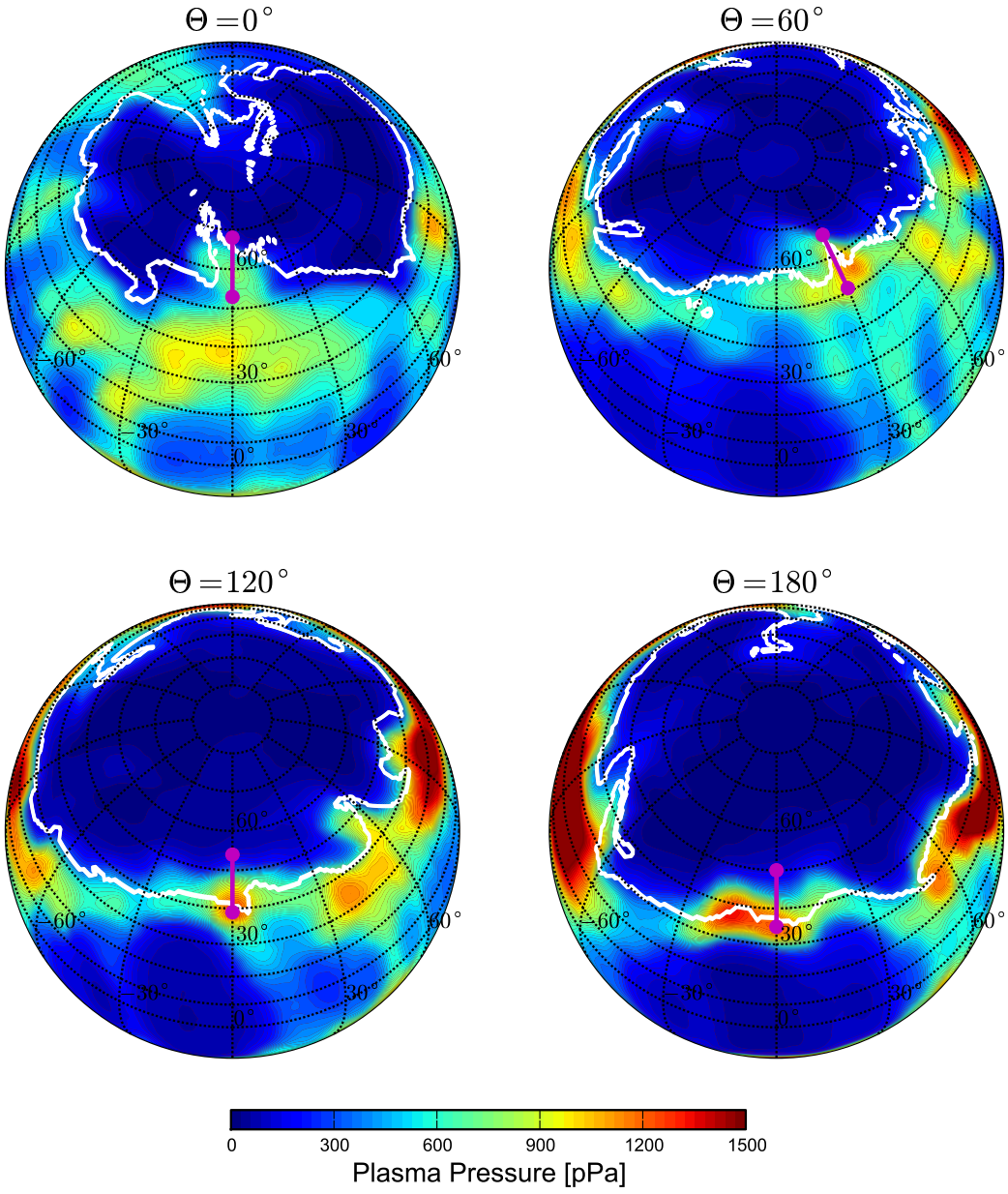

Figure 4-2: The cusp locations at the altitude of 4 Re during four different IMF clock angles. The plasma pressure (the color contour) and the open-closed field line boundary (the white lines) at this altitude are obtained from the OpenGGCM simulations. The cusp resides in the high plasma pressure region near the open-closed field line boundary. We launch virtual satellites along the magenta lines to obtain cusp structures.

The cusp is full with the magnetosheath plasma that precipitates from the reconnection sites along the open field lines. The cusp plasma has high density and strong plasma pressure, and the low-latitude boundary of the cusp is located near the open-closed field line boundary. Based on this information, we determine the strong plasma pressure region near the open-closed field line boundary as the OpenGGCM's cusp. The cusp is located near (GSE longitude, GSE latitude) = (0°, 60°) during 0° IMF clock angle and near (30°, 60°) during 60° IMF clock angle. Unlike the two northward IMF cases, the cusp resides at a much lower latitude during southward IMF. We observe the cusp near (0°, 40°) during 120° IMF clock angle and near (0°, 35°) during 180° IMF clock angle.

The cusp location varies due to different reconnection locations. During northward IMF, reconnection occurs near the lobe region, dropping magnetosheath plasma into high latitudes. This causes a strong plasma pressure region at the high latitudes. However, reconnection during southward IMF happens near the subsolar region. The magnetosheath plasma precipitates at low latitudes, producing a high plasma pressure region.

To obtain cusp ion structures, we determine virtual satellite orbits to cross the modeled cusps. The magenta lines in Figure 4-2 show the orbits chosen for this study. They pass the cusp along the noon-midnight meridian during 0°, 120°, and 180° IMF clock angles, and along the 30° longitudinal line during 60° IMF clock angle. Although we introduce constant solar wind and IMF conditions for the OpenGGCM runs, the magnetosphere is not quiet, producing not only spatial but also temporal magnetopause activities. The cusp mixes with magnetosheath ions precipitating by both the temporal and spatial magnetopause processes, causing a variety of cusp ion structures. Since we are interested in a spatial cusp structure that each IMF condition produces, it is important to investigate whether the modeled structure is

spatial. Therefore, we launch virtual satellites every 5 minutes along the selected orbits, and choose a cusp ion structure whose main features remain stationary at least for 15 minutes as a spatial structure.

Figure 4-3 shows cusp ion structures predicted by the OpenGGCM-LTPT model. Our model produces normal dispersion during due southward IMF and reverse dispersion during due northward IMF, as expected. As IMF B_y becomes strong, it produces different cusp structures. We observe double reverse dispersions during 60° IMF clock angle and flat structure followed by normal dispersion during 120° IMF clock angle. The flat and dispersed pattern matches the DMSP observation shown in Plate 5 of *Wing et al.* [2001].

4.5 The relation between cusp ion structures and magnetopause processes

4.5.1 0° IMF clock angle

To understand the precipitating patterns of cusp ions, we display their magnetopause entry points in Figure 4-4. To calculate the ion entry points, we first determine the magnetopause location with the method introduced in section 4.3. Then, we follow the trajectories of cusp ions back to the magnetopause and find where the ions penetrate the magnetopause. These entry points are projected as colored dots on the YZ plane as viewed from the Sun. The entry points of each column are colored according to the latitude at which the ions precipitate, ion energy at the cusp, and travel time between the cusp and the magnetopause. Since latitudinal coverage of cusp structures varies according to IMF conditions, we color the entry points of the first column based on the distance to the lower latitude boundary of the cusp spectrograms shown in Figure 4-3. Thus, 52°, 49°, 38°, and 34° GSE latitude are the boundaries (lat_0) for

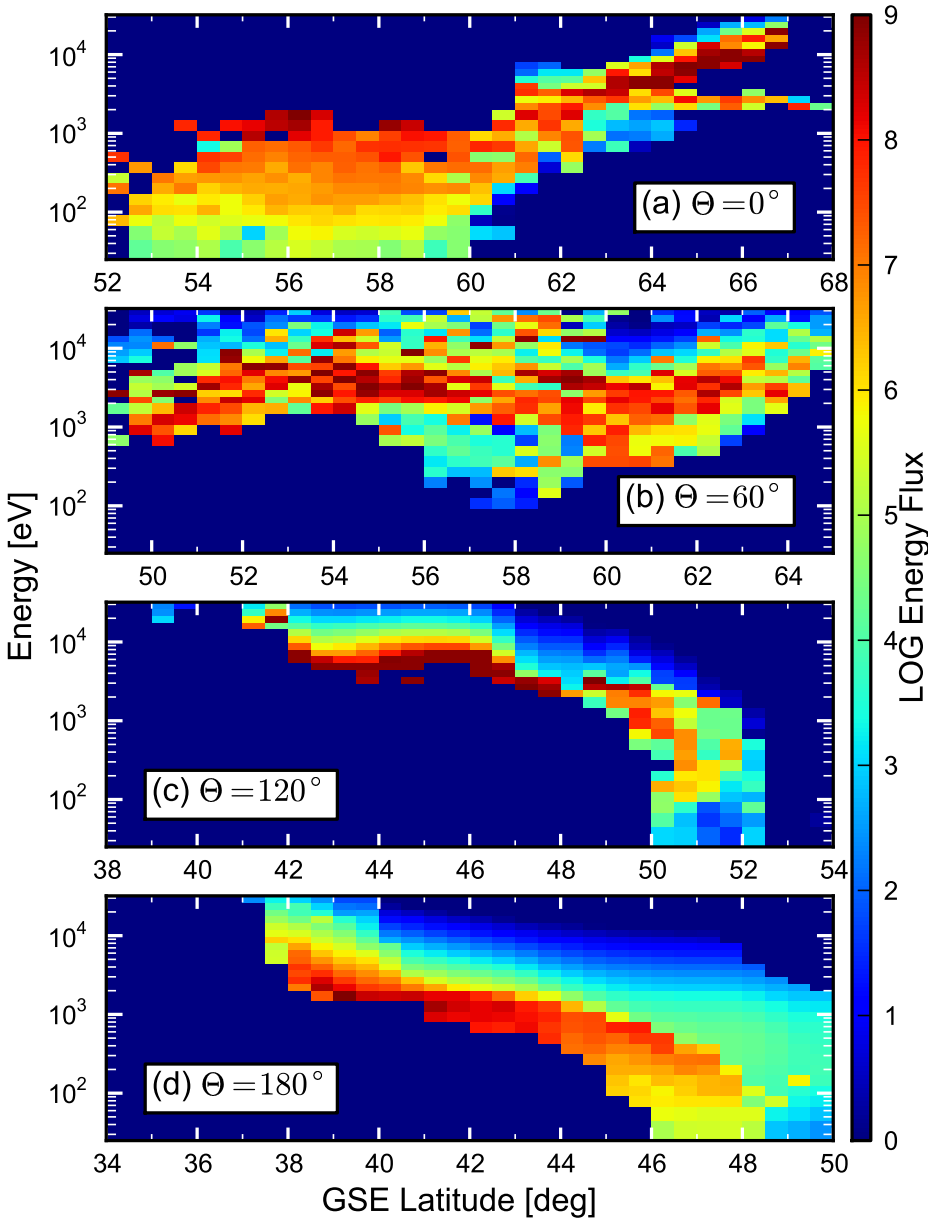

Figure 4-3: Energy versus latitude spectrograms obtained from the OpenGGCM-LTPT model during different IMF clock angles.

0°, 60°, 120° and 180° IMF clock angles. The black circles in Figure 4-4 represent the magnetopause location at the terminator plane.

Figure 4-4 (a) shows the ion magnetopause entry points during due northward IMF. We observe three major ion source regions near the high latitudes of northern magnetopause, the high latitudes of southern magnetopause, and the region along the noon-midnight meridian. The ions from the first two sources precipitate at high latitudes of the cusp, producing reverse dispersion in Figure 4-3 (a). These ions have higher energy, arriving at the cusp from the magnetopause in less than 15 minutes. The ions from the noon-midnight meridian region produce the flat ion structures at low latitudes of the cusp. These ions have lower energies than ions from high latitudes of the magnetopause, taking much longer to reach the cusp.

Figure 4-5 shows how ions from different source regions penetrate the magnetopause. We select an ion from each source region and project its trajectory on the XZ and YZ planes with magnetic field lines that the ion has passed. The black lines are ion trajectories, and the green, red, and blue lines represent IMF field lines, open field lines, and closed field lines. The top, middle, and bottom panels of Figure 4-5 show cusp ions originating from the high latitudes of northern magnetopause, the high latitudes of southern magnetopause, and the region along the noon-midnight meridian. In each panel, we provide the latitude where each ion is observed, its energy at the cusp, and the duration to reach the cusp from the magnetopause.

The ions in the top two panels precipitate at the high-latitude cusp after passing open field lines. These field lines are kinked at high latitudes of both the northern and southern magnetopause, suggesting that lobe reconnection occurs at both the northern and southern hemisphere and produces reverse dispersion. The ion in the bottom panel is an old ion that entered the magnetopause 81 minutes before. It moves back and forth between the northern and southern cusp along the closed field lines until

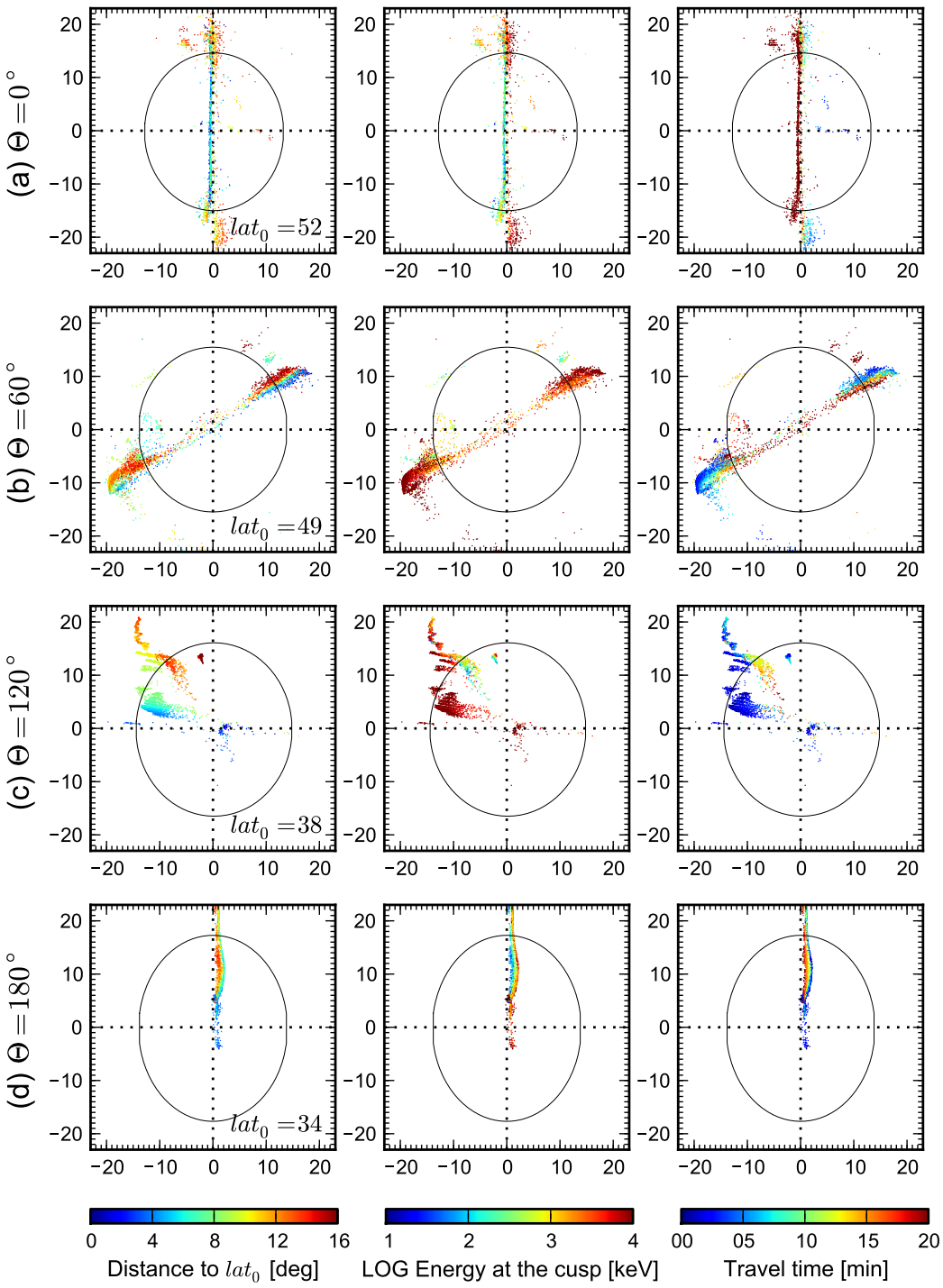

Figure 4-4: The magnetopause entry points of cusp ions as viewed from the Sun. The black circles represent the magnetopause location at a terminator plane, and lat_0 is the low-latitude boundary of cusp spectrograms in Figure 4-3.

our virtual satellite observes it. As the field lines have almost zero convection speed, ions precipitate at the same latitudes despite their speed, producing dispersionless structure at the low-latitude cusp.

To understand the reconnection pattern during 0° IMF clock angle, we calculate magnetic shear over the magnetopause and display them with the ion entry points. Figure 4-6 (a) shows the results projected on YZ plane. We select two points $3R_E$ inward and outward of the magnetopause along the radial line, obtaining pure magnetic fields of the magnetosheath and magnetosphere for the shear angle measurement. The color contour represents the magnetic shear, and the blue line contour shows an anti-parallel reconnection region whose shear angle is over 170°. The black circles are the magnetopause location at the terminator plane. The anti-parallel reconnection zones appear at high latitudes of both the northern and southern magnetopause. The major ion source regions match well with the anti-parallel reconnection zones, showing that the reconnection causes reverse dispersion.

4.5.2 60° IMF clock angle

Figure 4-4 (b) shows where cusp ions penetrate the magnetopause. We observe two major source regions near $Z_{gse} = -10\,R_E$ on the dawnside magnetopause and near $Z_{gse} = 10\,R_E$ on the duskside magnetopause. Ions from the two source regions precipitate at both low-latitude cusp and high-latitude cusp, producing double dispersions observed in Figure 4-3 (b). Ions producing the high-latitude dispersion are fresh ions that recently penetrated the magnetopause, while ions producing the low-latitude dispersion are old ions which entered the magnetopause more than ∼15 minutes previously. Thus, these ions precipitate into the cusp at different times from the same ion source regions, indicating that intermittent reconnection leads to double dispersions.

Figure 4-7 displays how ions enter the cusp from the two major source regions.

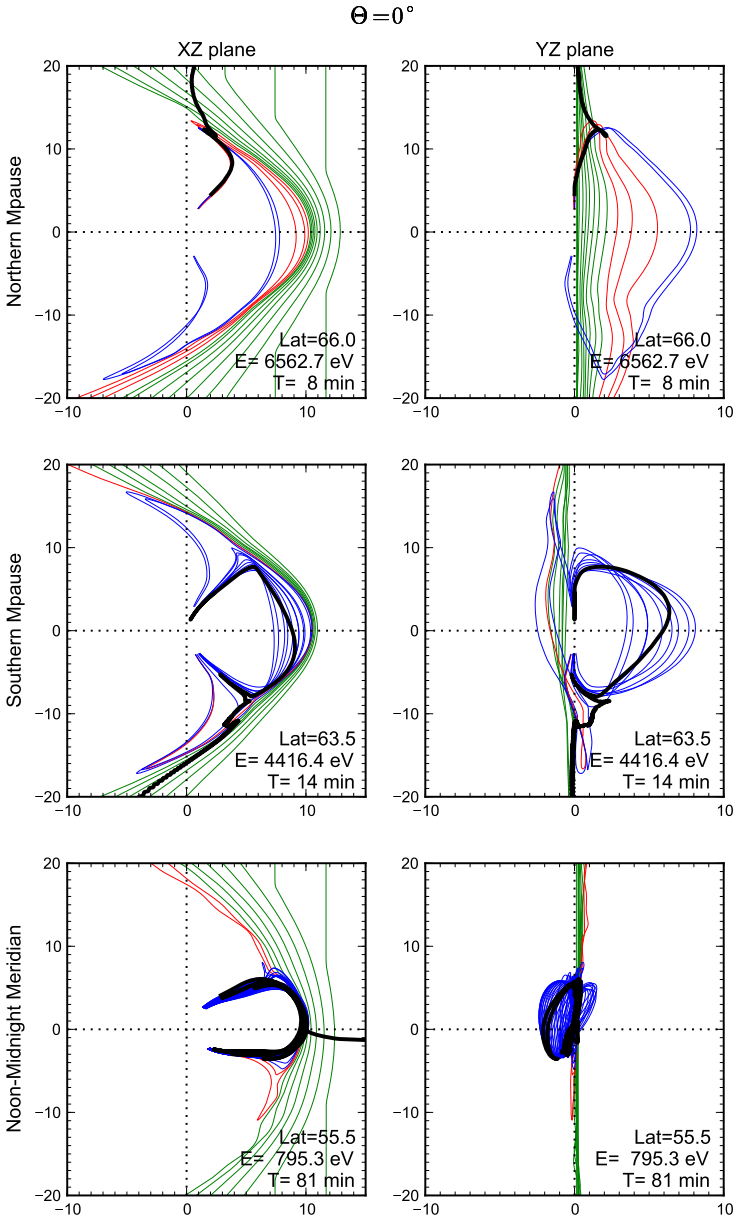

Figure 4-5: Trajectories of cusp ions from different magnetopause source regions during 0° IMF clock angle. The green, red, blue lines are IMF, open, and closed field lines, and the black lines are ion trajectories.

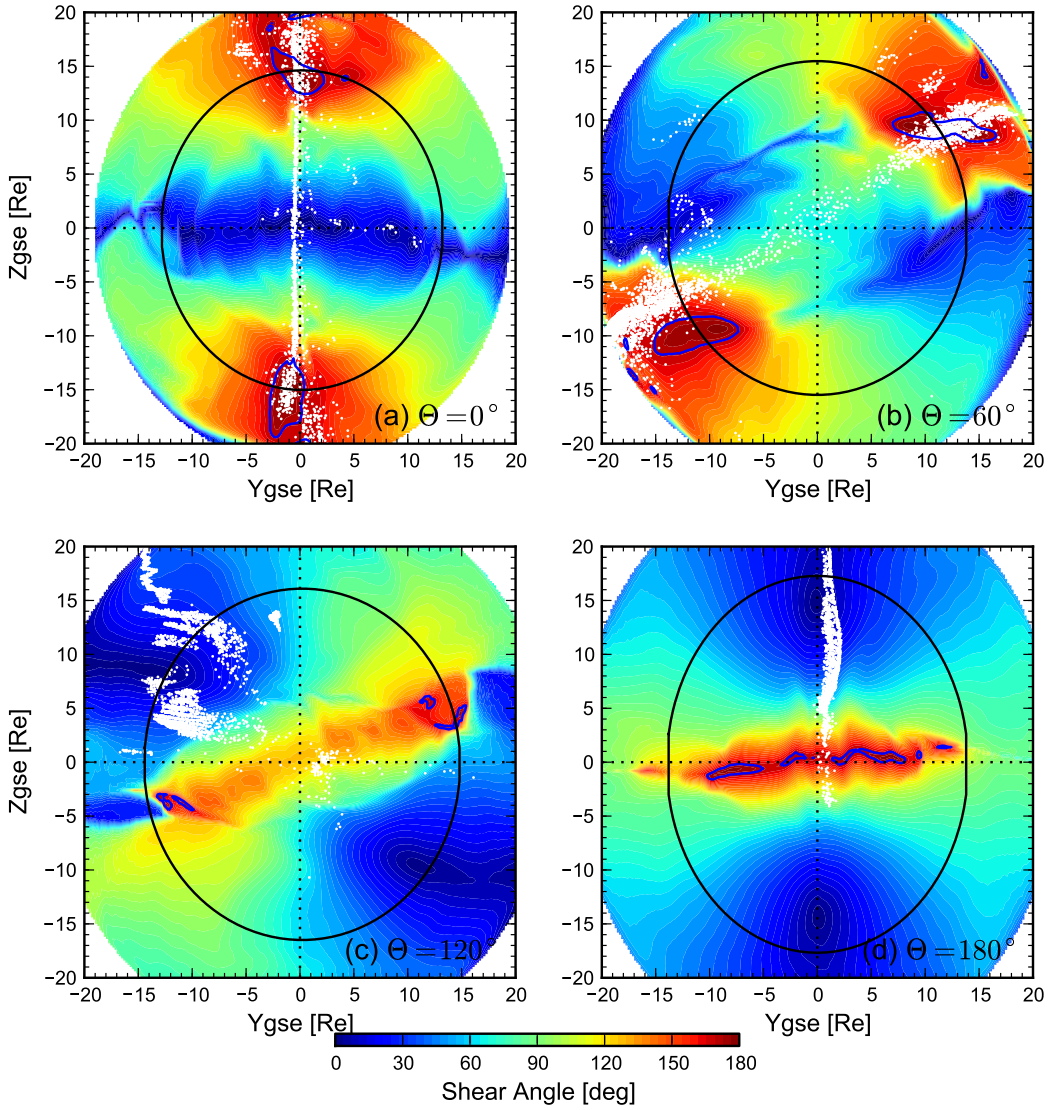

Figure 4-6: Magnetic shear over the magnetopause with the ion entry points.

The top two panels show ions precipitating at high latitudes of the cusp. The ion from the northern magnetopause passes the open field lines kinked near the northern magnetopause, demonstrating that reconnection near this region causes ion precipitation. The ion from the southern magnetopause also passes similar open field lines before entering the cusp. However, one of the field lines in the southern magnetopause is roped, indicating a flux transfer event (FTE) near this region. FTEs are signatures of intermittent magnetic reconnection [*Fear et al.*, 2009; *Hasegawa et al.*, 2010], observed near the Earth's magnetopause with magnetic field enhancement and a bipolar variation of magnetic field component along the normal to the magnetopause. Magnetic field lines around the FTEs are roped as seen in the second row of Figure 4-7. Thus, this ion precipitates into the cusp via reconnection on both the northern and southern magnetopause. The bottom two panels show ions entering the low-latitude cusp from the two ion source regions. The kinked open field lines that these ions have crossed indicate that reconnection happens at both the northern and southern magnetopause. The ions penetrated the magnetopause more than 10 minutes ago, undergoing the periodic motions between the northern and southern cusp along the closed field lines before being observed by our virtual satellite.

To understand the reconnection pattern, we display magnetic shear on the magnetopause with the ion entry points in Figure 4-6 (b). The details of this Figure are the same as those of Figure 4-6 (a). The anti-parallel reconnection zone appears near $Z_{gse} = -10\,R_E$ on the dawnside magnetopause and near $Z_{gse} = 10\,R_E$ on the duskside magnetopause. The major ion source regions are in the vicinity of these reconnection zones, supporting the idea that dual reconnection at both hemispheres is the major process of ion precipitation.

We observe several FTEs on the southern magnetopause during 1.5 hours of the ion tracing period. Figure 4-8 shows the repetitive formation of an FTE during 60°

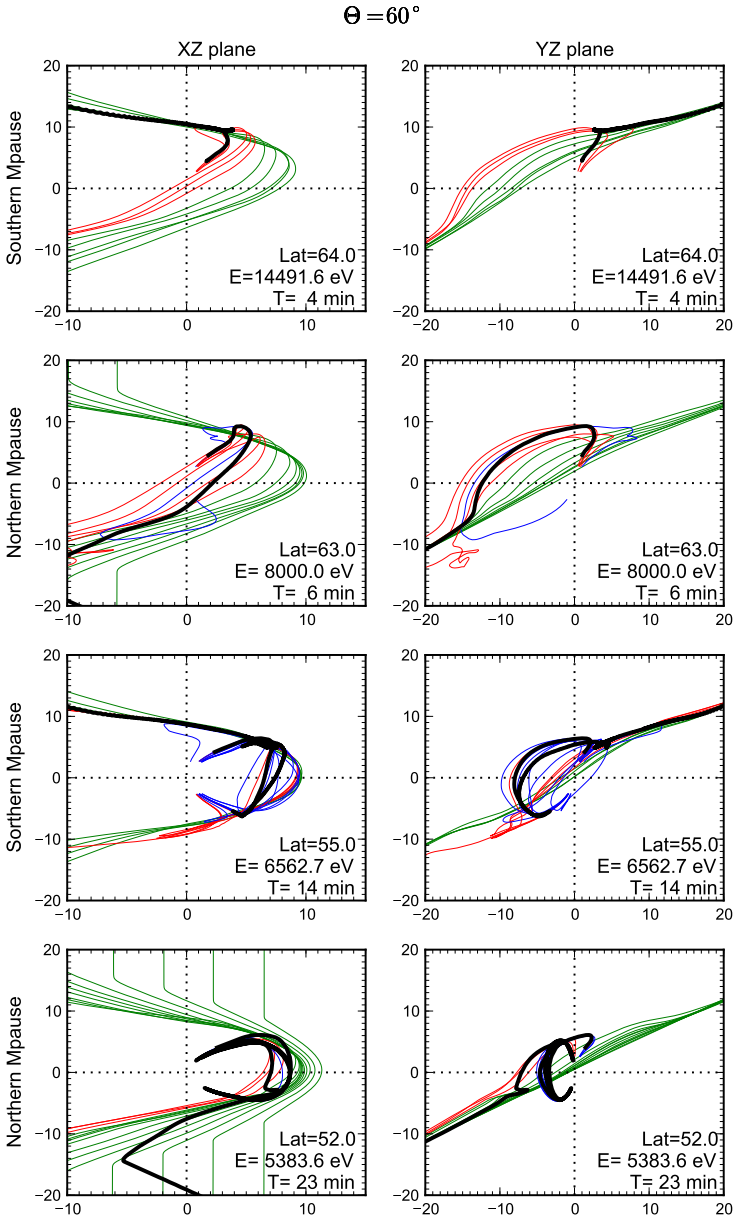

Figure 4-7: Trajectories of cusp ions from different magnetopause source regions during 60° IMF clock angle. The other details are the same as Figure 4-5.

IMF clock angle. To display this event effectively, we select the plane parallel to the 60° IMF clock angle, and calculate magnetic field magnitude ($|B|$) and Z component of plasma velocity (V_z) of this plane. t_0 represents the time we observe the double dispersions. At $T = t_0 - 25\,min$, an FTE occurs near $Z_{gse} = -4\,R_E$ with increased magnetic field and strong northward flow. After it convects tailward, the northward plasma flow slows down at $T = t_0 - 15\,min$, indicating that reconnection at the southern magnetopause becomes quiet. At $T = t_0 - 10\,min$, a new FTE appears near $Z_{gse} = -6\,R_E$ with magnetic field enhancement and fast northward plasma flow. Note that reconnection also happens on the northern magnetopause, causing the southward plasma flow. The recurring FTE formation drops ions intermittently into the magnetosphere along the open field lines. These field lines are draped over the magnetopause, connecting the southern cusp and the northern magnetosheath. The reconnection on the northern magnetopause closes the open field lines, causing ion precipitation into the northern cusp and producing double reverse dispersions.

Several statistical studies have shown that FTEs appear predominantly during southward IMF. [*Rijnbeek et al.*, 1984; *Berchem and Russell*, 1984; *Kuo et al.*, 1995]. However, FTEs have been also observed during northward IMF [*Kawano and Russell*, 1997; *Chandler and Avannov*, 2003; *Fear et al.*, 2005]. Although this chapter does not discuss the FTE events during southward IMF, our OpenGGCM-LTPT model does observe the FTE signatures during southward IMF as well as northward IMF.

4.5.3 120° IMF clock angle

Figure 4-4 (c) shows the magnetopause entry points of cusp ions during 120° IMF clock angle. Two major ion source regions are observed near $Z_{gse} = 4\,R_E$ and $Z_{gse} = 10\,R_E$. Ions from the low-latitude magnetopause precipitate at low latitudes of the northern cusp, composing the flat cusp structure in Figure 4-3 (c). These ions are

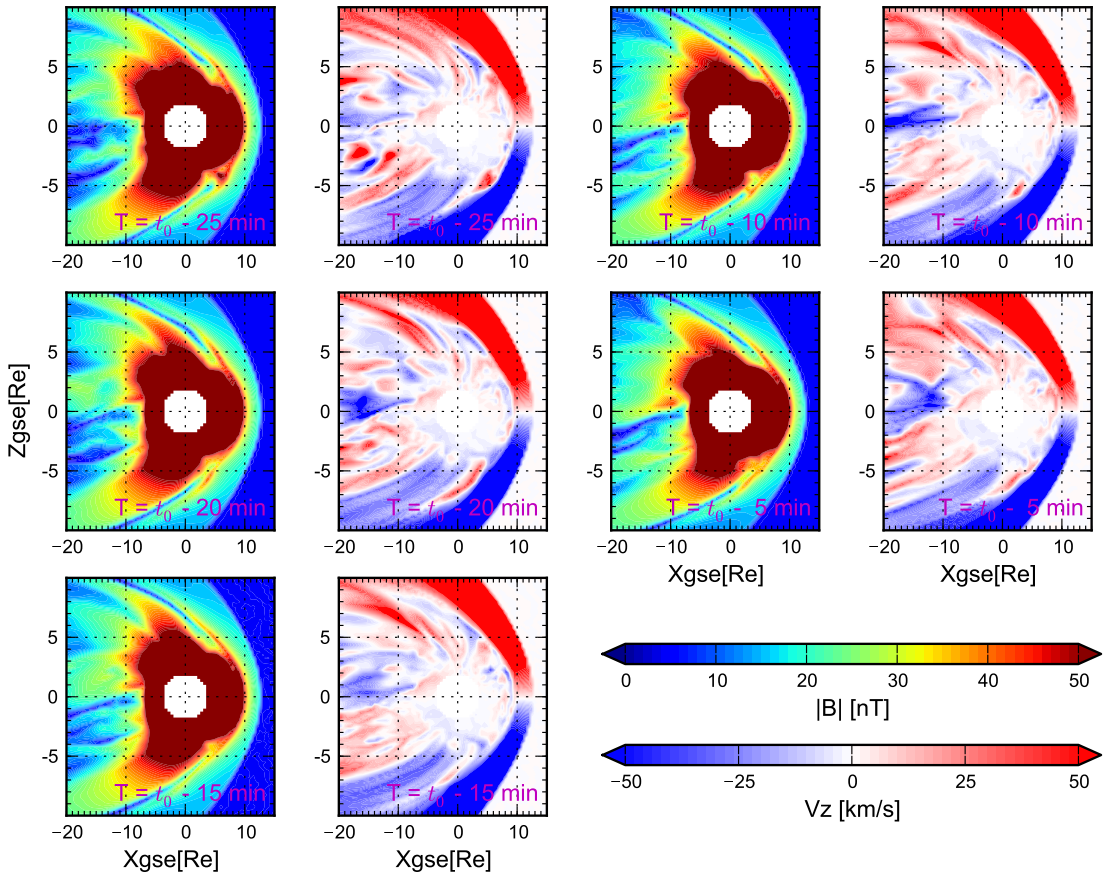

Figure 4-8: Repetitive FTE formation during 60° IMF clock angle. The color contours represent magnetic field magnitude and Z_{gse} component of flow velocity, projected on the 60° tilted plane (i.e., the plane parallel to the IMF clock angle). t_0 is the time when our virtual satellite observes double dispersions.

high-energy, and take less than 5 minutes to travel between the magnetopause and the cusp. This source region is aligned with 120° IMF clock angle. Ions from the high-latitude magnetopause precipitate mostly at high latitudes of the cusp where dispersed signature is observed. These ions are less energetic than ions from the low-latitude magnetopause, and arrive at the cusp ∼15 minutes after entering the magnetopause.

Figure 4-9 shows how cusp ions enter the magnetopause. The top three panels show three ions from the low-latitude magnetopause, and the bottom panel shows an ion from the high-latitude magnetopause. The green and red lines are IMF and open field lines that each ion has crossed, and the black lines are the ion trajectories. The ions in the top three panels have different field line histories, although they originate from the same source region. The first open field lines they encounter are kinked at two different locations, one near the subsolar region and another near the northern duskside magnetopause. Thus, two reconnection sites appear near these regions, causing ion precipitation into the low-latitude cusp. The ion in the bottom panel passes the open field lines kinked near the northern duskside magnetopause, indicating that the ion enters the high-latitude cusp by reconnection in this region.

Note that the dispersed signature in Figure 4-3 (c) starts from 46° GSE latitude. Ions in the bottom two panels of Figure 4-9 precipitate at 46° and 49.5° GSE latitude, producing the dispersion at this latitude. Ions in the top two panels arrive at 42 and 43.5 GSE latitude, composing the flat structure. Thus, the ion source region at the low-latitude magnetopause produces both the flat structure and dispersion, while the source region at high latitude produces only the dispersion.

Figure 4-6 (c) displays the reconnection pattern during 120° IMF clock angle. The details of this Figure is the same as Figure 4-6 (a). The anti-parallel reconnection zones appear near $Z_{gse} = -4\,R_E$ on the dawnside magnetopause and near

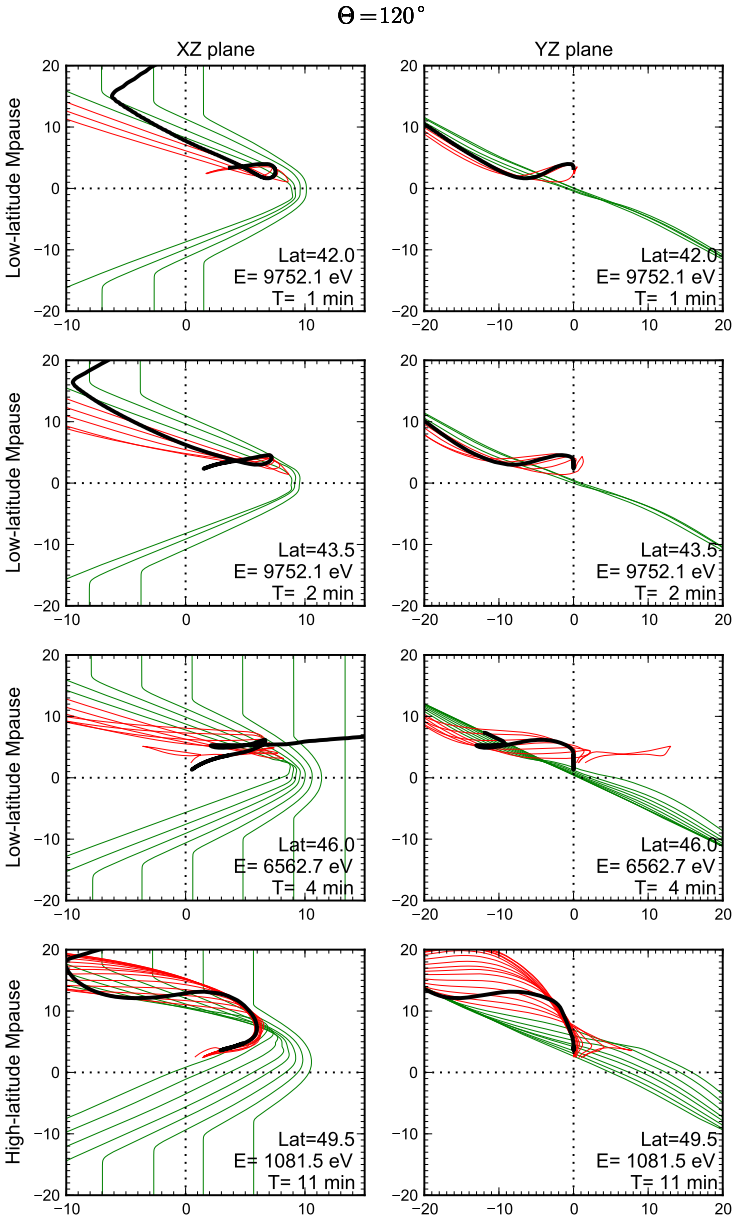

Figure 4-9: Trajectories of cusp ions from different magnetopause source regions during 120° IMF clock angle. The details are the same as Figure 4-5.

$Z_{gse} = 5\,R_E$ on the duskside magnetopause. Unlike the northward IMF cases, a high magnetic shear zone whose angle is over 120° crosses the subsolar region, connecting the two anti-parallel reconnection zones. This pattern agrees with Figure 7 in *Trattner et al.* [2007]. However, the high shear angle zone in our model does not extend to the nightside magnetopause, and the angle falls down to 0° in the regions near $(Y_{gse}, Z_{gse}) = (-15,\, -5)\,R_E$ and $(18,\, 5)\,R_E$. Since the OpenGGCM's magnetopause does not fit into the ellipsoid in these regions, the two points selected for the shear angle calculation are located in the same region, in either magnetosphere or magnetosheath, producing 0° magnetic shear.

Unlike the anti-parallel reconnection theory, the theory of component reconnection predicts that reconnection happens along the line that maximizes magnetic shear [*Moore et al.* 2002; *Trattner et al.* 2007]. The high magnetic shear zone crossing the subsolar region is therefore considered to be the component reconnection zone. Ions in the top two panels of Figure 4-9 (i.e., the ions composing the dispersionless structure) precipitate into the cusp via kinked open field lines near this subsolar region, showing that component reconnection causes precipitation. Ions in the bottom two panels (i.e., ions composing the dispersed structure) pass the open field lines kinked at the northern duskside magnetopause near $(Y_{gse}, Z_{gse}) = (10,\, 5)\,R_E$. The magnetic shear angle in this region is almost 180°, indicating that anti-parallel reconnection drops ions into the cusp. Thus, component reconnection causes a flat structure, and anti-parallel reconnection produces normal dispersion.

The kinked open field lines are created by both component and anti-parallel reconnection, linking the low-latitude magnetopause and the low-latitude cusp. Strong magnetic tension force moves these field lines dawnward, and the energy of ions is dispersed along the latitudinal line. As our virtual satellite orbits along the longitudinal line, dispersion is difficult to observe. This is why we observe a flat structure at

the low-latitude cusp. On the other hand, the high-latitude cusp is connected to the high-latitude magnetopause via straight magnetic field lines. Because of weak magnetic tension force, these field lines convect northward by the magnetosheath flow. Dispersion appears along the longitudinal line, the same direction of our satellite orbit. This is the reason we observe dispersion at the high-latitude cusp.

4.5.4 180° IMF clock angle

In Figure 4-4 (d), ion magnetopause entry points are aligned with 180° IMF clock angle. High-energy ions (over 1 keV) originate mainly from the low-latitude magnetopause, and precipitate into the low-latitude cusp for less than 10 minutes. Low-energy ions (less than 1 keV) originate from the high-latitude magnetopause, and take more than 10 minutes to reach the high-latitude cusp.

To understand how ions penetrate into the magnetosphere, Figure 4-10 displays their trajectories. The top, middle, and bottom panels show ions originating from the low, mid, and high latitudes of the magnetopause. The details of this Figure are the same as Figure 4-5. The ion from the high-latitude magnetopause is high energy, precipitating at the low-latitude cusp in a short time. The ion from low-latitude magnetopause is low energy, therefore taking more time to arrive at the high-latitude cusp. All three ions pass the open field lines kinked near subsolar region, indicating that subsolar reconnection causes ion precipitation.

Figure 4-6 (d) displays magnetic shear over the magnetopause during due southward IMF. The color contour shows the shear angle, and the white dots are the ion entry points. The anti-parallel reconnection zones (the blue contour lines) appear near the equatorial plane. This pattern agrees with Figure 5 in *Trattner et al.* [2007]. The ion source regions spread from the anti-parallel reconnection zone to a low magnetic shear angle zone. However, as seen in Figure 4-10, all the ions penetrate into

the cusp via the kinked open field lines near subsolar region, supporting the idea that subsolar reconnection produces normal dispersion.

4.6 Summary and Discussion

We have investigated the relation between cusp ion structures and magnetopause processes during 0°, 60°, 120°, and 180° IMF clock angles. We ran an OpenGGCM simulation for each IMF condition, and used their electromagnetic fields for modeling a cusp ion structure. Since we were interested in the spatial nature of cusp structures, we launched virtual satellites every five minutes along the longitudinal line that passes the OpenGGCM's cusp. Then we selected a cusp spectrogram that remains stationary for at least 15 minutes, and studied which reconnection process causes it. Our model produced a normal dispersion during southward IMF and a reverse dispersion during northward IMF. These results reinforce our understanding. As IMF B_y becomes dominant, we observed a flat and dispersed structure for 120° IMF clock angle and double reverse dispersions for 60° IMF clock angle.

To understand the magnetopause processes that lead to various cusp structures, we analyzed the precipitating patterns of cusp ions, and related them to the reconnection processes inside OpenGGCM. We first calculated magnetopause entry points of cusp ions and displayed them with colored points based on the latitude at which the ions were observed, their energy at the cusp, and the travel time between the cusp and the magnetopause. From this process, we found multiple ion source regions for each IMF condition, and observed that each source region has a unique precipitating pattern. To study how ions from different source regions penetrate the magnetopause, we selected an ion from each source region and represented its trajectory with magnetic field lines that it had passed. All the ions passed the kinked open field lines, indicating that reconnection occurs nearby, causing ion precipitation. To support these results, we

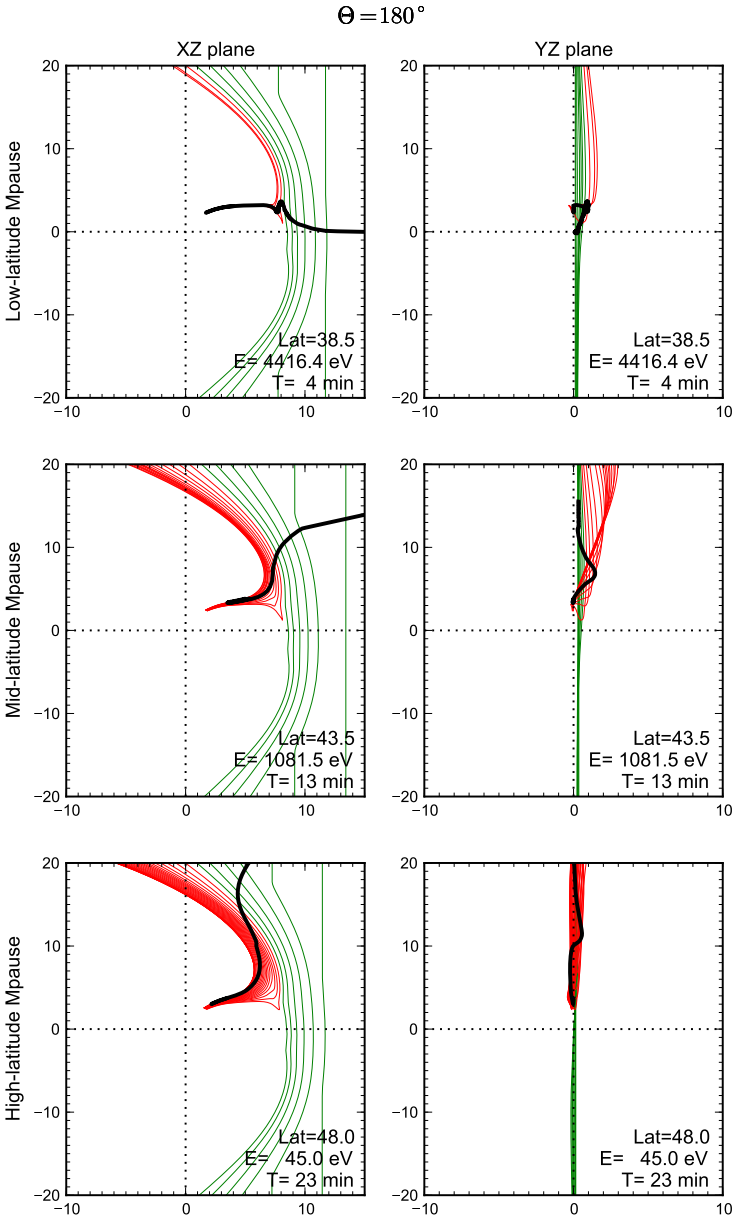

Figure 4-10: Trajectories of cusp ions from different magnetopause source regions during 180° IMF clock angle. The other details are the same as Figure 4-5.

studied the OpenGGCM's reconnection patterns by displaying magnetic shear angle over the magnetopause. The anti-parallel and component reconnection zones agree with the region where the field lines are kinked. From this investigation, we found that:

1. During 0° IMF clock angle, anti-parallel reconnection at both the northern and southern lobes produces a reverse dispersion.

2. During 60° IMF clock angle, the repetitive FTE formation on the southern magnetopause drops ions intermittently into the northern cusp, causing double reverse dispersions.

3. During 120° IMF clock angle, component reconnection occurs near the subsolar region, producing a flat structure at low latitudes of the cusp. At the same time, anti-parallel reconnection happens at low-latitude magnetopause, resulting in a dispersed signature at high latitudes of the cusp.

4. During 180° IMF clock angle, anti-parallel reconnection appears along the equatorial plane, causing a normal dispersion in the northern cusp.

From the study of ion magnetopause entry points, we found different precipitating patterns between the northward and southward IMF cases.

1. Cusp ions originate from both the northern and southern magnetopause during northward IMF. Conversely, during southward IMF, ions precipitate only from the northern magnetopause. Lobe reconnection happens at both hemispheres during northward IMF, creating closed field lines which connect the northern and southern cusp. Therefore, ions entering both northern and southern magnetopause easily precipitate into the northern cusp along the closed field lines. However, during southward IMF reconnection happens at low-latitude magnetopause, creating kinked open field lines which convect toward the south pole.

Since ions entering the southern magnetopause move poleward with these field lines, it is very rare to observe these ions at the northern cusp. Therefore, the major ion source regions for the northern cusp are located only on the northern magnetopause during southward IMF.

2. The major ion source regions during northward IMF are located in the vicinity of anti-parallel reconnection zones, while during southward IMF, source regions expand from a high magnetic shear zone to a very low magnetic shear zone. During northward IMF, reconnection occurs at high latitudes of both the northern and southern magnetopause, creating kinked open field lines that convect equatorward. As they move against the magnetosheath flow, the convection speed decreases, becoming almost zero near the low-latitude boundary of the cusp. This confines the open field lines in the narrow region between the reconnection site and the low-latitude cusp boundary, causing ion precipitation near the reconnection zones. During southward IMF, on the other hand, reconnection happens near the low-latitude magnetopause, moving kinked open field lines poleward. As they move in the same direction as the magnetosheath flow, the field lines convects away from the reconnection sites at faster speed, spreading the ion source region from a high to low magnetic shear zone.

Chapter 5

Summary

Magnetic reconnection is a key mechanism for transferring solar wind energy into the Earth's magnetosphere. The magnetosphere uses this energy as fuel, producing various geomagnetic events such as magnetic storms, substorms, and auroras. Despite many studies on magnetic reconnection, there are still underlying questions: where, when, and which reconnection (anti-parallel or component) occurs on the dayside magnetopause. The observations are not conclusive to answer these questions, since direct observation of reconnection is limited by the small number of satellites. Previous models of reconnection patterns [*Cowley et al.*, 1982; *Moore et al.*, 2002] are based on static magnetic field configuration although reconnection is a dynamic process. The model studies do not answer whether reconnection actually happens at the predicted locations.

In this dissertation, we focused on cusp ion structures, a dynamic result of reconnection, to investigate reconnection patterns. As the cusp is connected to the dayside magnetopause along the open field lines, it is filled with solar wind ions precipitating from the reconnection sites wherever they occur on the magnetopause. Many studies have used cusp ion structures, especially dispersed ion signature, to infer the locations and properties of dayside reconnection. However, the satellites move relative to the cusp, producing temporal and spatial ambiguities in the observations. More than one satellite needs to be in the cusp in order to understand the spatial or temporal nature of reconnection. Under this restriction, models of cusp ion structures have been

developed as a tool for studying the relationship between cusp structures and dayside reconnection. However, previous models of cusp structures use static empirical electromagnetic field models, and their study is limited only to spatial cusp structures during constant solar wind conditions. A dynamic model of cusp ion structures is necessary.

We developed a new model of cusp ion structures by using the OpenGGCM global MHD model and the Liouville Theorem Particle Tracer. OpenGGCM produces reconnection by calculating the resistive MHD equations, and provides time-dependent electromagnetic fields as well as number density, velocity, and plasma pressure of the magnetosphere and its surrounding environments. The LTPT conducts a full particle tracing by integrating the Lorentz equation and the equation of motion with electromagnetic fields obtained from the OpenGGCM. It traces test particles backward in time from the cusp to the magnetosheath, calculates phase-space densities of test particles at the magnetosheath, and then maps the densities into the cusp using Liouville's Theorem. We displayed these densities in energy-time or energy-latitude spectrograms, obtaining cusp ion structures. By using this advanced model, we can study both of temporal and spatial cusp structures as well as reconnection processes that lead to these structures.

We first demonstrated our model's ability to produce reasonable cusp structures and investigate dayside reconnection properties. We selected three cusp crossing events of the Cluster and Polar satellites during non-steady solar wind conditions, and reproduced cusp spectrograms observed by these satellites. We set four criteria to compare the modeled and observed spectrograms, evaluating the model results as "excellent", "good", "satisfactory" and "not satisfactory" based on the number of fulfilled criteria. We obtained two excellent, three good, and two satisfactory results, showing our model includes all the essential physics to produce observed cusp

structures. To investigate the physical processes on the magnetopause, we analyze ion precipitating patterns and magnetopause movements inside the OpenGGCM-LTPT model. We concluded that sudden increase of solar wind pressure, non-steady reconnection rates, and change of IMF clock angles are the main mechanisms that produce observed structures.

After the model validation test, we expanded our study to obtain the general relation between cusp structures and magnetopause processes. We introduced four IMF clock angles of 0°, 60°, 120°, and 180° as inputs for the OpenGGCM runs, and kept the other solar wind parameters constant to avoid undesired magnetopause activities. Our model produced a normal dispersion during due southward IMF and a reverse dispersion during due northward IMF, coinciding with our understanding of cusp structures. As IMF B_y became dominant, we observe different cusp structures, double reverse dispersions during 60° IMF clock angle, and a flat and dispersed structure during 120° IMF clock angle. We studied which magnetopause activity leads to various cusp structures by analyzing ion magnetopause entry points, ion trajectories, and magnetic shear on the magnetopause. We found that lobe reconnection, repetitive FTE formation, combination of component and anti-parallel reconnection, and subsolar reconnection cause the cusp structures during 0°, 60°, 120°, and 180° IMF clock angles. We also found that the precipitating pattern depends on the IMF conditions. For the northward IMF cases, cusp ions precipitate mostly from the anti-parallel reconnection zones (whose magnetic shear is over 170°) on both the northern and southern magnetopause. However, for the southward IMF cases ions in the northern cusp precipitate only from the same northern magnetopause, and magnetic shear of these ion source regions varies from 0° to 180°.

We developed a new model of cusp ion structures, and finished its validation test. Then, we revealed the general relationship between cusp ion structures and

dayside reconnection during four different IMF clock angles. Although we focused only on spatial cusp structures in this dissertation, we observed a variety of temporal cusp structures during the same steady IMF conditions. In future work, we will analyze physical processes behind this variety. We will also study cusp ion structures under strong solar wind velocity, high solar wind density, dominant IMF B_x, and different dipole tilt angles, and investigate which reconnection patterns cause these structures. This research will provide not only a complete profile of dispersed ion signatures caused by dayside reconnection, but also a comprehensive understanding of reconnection patterns as a function of solar wind and IMF conditions. These results will provide a firm research background for the future MMS mission whose primary goal is to understand magnetic reconnection.

Bibliography

[1] Aubry, M. P., C. T. Russell, and M. G. Kivelson (1970), Inward motion of the magnetopause before a substorm, *J. Geophys. Res., 75*, 7018–7031.

[2] Berchem, J., and C. T. Russell (1984), Flux transfer events on the magnetopause: Spatial distribution and controlling factors, *J. Geophys. Res., 89*, 6689.

[3] Chandler, M. O., and L. A. Avanov (2003), Observations at low latitudes of magnetic merging signatures within a flux transfer event during a northward interplanetary magnetic field, *J. Geophys. Res., 108*(A10), 1358, doi:10.1029/2003JA009852.

[4] Cowley, S. W. H. (1982), The causes of convection in the Earth's magnetosphere: A review of developments during IMS, *Rev. Geophys., 20,* 531.

[5] Cravens, T. E. (1997), *Physics of Solar system plasmas*, Cambridge Univ. Press, New York.

[6] Escoubet, C. P., et al. (2008a), Effect of a northward turning of the interplanetary magnetic field on cusp precipitation as observed by Cluster, *J. Geophys. Res., 113*, A07S13, doi:10.1029/2007JA012771.

[7] Escoubet, C. P., et al. (2008b), Ion energy steps observed by Cluster multi-point mission in the polar cusp: similarities and differences, paper presented at 2008 AGU Fall Meeting, AGU, San Francisco, CA.

[8] Fairfield, D. H. (1971), Average and unusual locations of the earth's magnetopause and bow shock, *J. Geophys. Res., 76*, 6700–6716.

[9] Fear, R. C., A. N. Fazakerley, C. J. Owen, and E. A. Lucek (2005), A survey of flux transfer events observed by Cluster during strongly northward IMF, *Geophys. Res. Lett., 32,* L18105, doi:10.1029/2005GL023811.

[10] Fear, R. C., S. E. Milan, A. N. Fazakerley, K.-H. Fornacon, C. M. Carr, and I. Dandouras (2009), Simultaneous observations of flux transfer events by THEMIS, Cluster, Double Star, and SuperDARN: Acceleration of FTEs, *J. Geophys. Res., 114,* A10213, doi:10.1029/2009JA014310.

[11] Formisano, V., V. Domingo, and K.-P. Wenzel (1979), The three-dimensional shape of the magnetopause, *Planet. Space Sci., 27*, 1137-1149.

[12] Gosling, J. T., M. F. Thomsen, S. J. Bame, T. G. Onsager, and C. T. Russell (1990), The electron edge of the low-latitude boundary layer during accelerated flow events, *Geophys. Res. Lett., 17*, 1833.

[13] Gurnett, D. A., and A. Bhattachjarjee (2005), *Introduction to Plasma Physics With Space and Laboratory Applications,* Cambridge University Press, United Kingdom.

[14] Hasegawa, H., et al. (2010), Evidence for a flux transfer event generated by multiple Xline reconnection at the magnetopause, *Geophys. Res. Lett., 37,* L16101, doi:10.1029/2010GL044219.

[15] Hill, T. W., and M. E. Rassbach (1975), Interplanetary magnetic field direction and the configuration of the dayside magnetosphere, *J. Geophys. Res., 80*, 1–6.

[16] Hill, T. W., and P. H. Reiff (1977), Evidence of magnetospheric cusp proton acceleration by magnetic merging at the dayside magnetopause, *J. Geophys. Res., 82*, 3623.

[17] Kawano, H., and C. T. Russell (1997), Cause of postterminator flux transfer events, *J. Geophys. Res., 102,* 27,029-27,038.

[18] Kuo, H., C. T. Russell, and G. Le (1995), Statistical studies of flux transfer events, *J. Geophys. Res., 82*, 3623.

[19] Lavraud, B., and P.J. Cargill (2005), Cluster reveals the magnetospheric cusps, *Astronomy and Geophysics 46*, 1.32–1.35.

[20] Maezawa, K. (1974), Dependence of the magnetopause position on the southward interplanetary magnetic field, *Planet. Space Sci., 22*, 1443–1453.

[21] Maltsev, Yu. P., and W. B. Lyatsky (1975), Field-aligned currents and erosion of the dayside magnetopause, *Planet. Space Sci., 23*, 1257–1260.

[22] Maynard, N. (2005), Coupling the solar-wind/IMF to the ionosphere through the high latitude cusps, *Surveys in Geophysics, 26*, 255-280.

[23] Moore, T. E., M.-C. Fok, and M. O. Chandler (2002), The dayside reconnection X line, *J. Geophys. Res., 107*(A10), 1332.

[24] Onsager, T. G., S.-W. Chang, J. D. Perez, J. B. Austin, and L. X. Janoo (1995), Low-altitude observations and modeling of quasi-steady magnetopause reconnection, *J. Geophys. Res., 100*, 11831–11844, doi:10.1029/94JA02702.

[25] Palmroth, M., T. I. Pulkkinen, P. Janhunen, and C.-C. Wu (2003), Stormtime energy transfer in global MHD simulation, *J. Geophys. Res., 108*(A1), 1048, doi:10.1029/2002JA009446.

[26] Perromian, V. (1994), Large scale kinetic modeling of magnetospheric plasma, Ph.D. thesis, Univ. of Calif. at Los angeles, Los Angeles, Calif.

[27] Perromian, V., M. El-Alaoui, M. A. Abdalla, and L. M. Zelenyi (2006), Dynamics of ionospheric O+ ions in the magnetosphere during the 24-25 September 1998 magnetic storm, *J. Geophys. Res., 111*, A12203, doi:10.1029/2006JA011790.

[28] Raeder, J. (2003), Global magnetohydrodynamics: A tutorial, in *Space Plasma Simulation*, edited by J. Buechner, C. T. Dum, and M. Scholer, *Lect. Not. in Phys.*, vol. 615, Springer, New York.

[29] Raeder, J., J. Berchem, and M. Ashour-Abdalla (1996), The importance of small scale processes in global MHD simulations: Some numerical experiments, in *The Physics of Space Plasmas*, edited by T. Chang, and J.R. Jasperse, vol. 14, p. 403, Cambridge, MA, MIT Center for Theoretical Geo/Cosmo Plasma Physics.

[30] Raeder, J., J. Berchem, and M. Ashour-Abdalla (1998), The Geospace Environment Modeling grand challenge: Results from a Global Geospace Circulation Model, *J. Geophys. Res., 103*, 14787.

[31] Raeder, J., D. Larson, W. Li, E. L. Kepko, and T. Fuller-Rowell (2008), OpenGGCM Simulations for the THEMIS Mission, *Space Sci. Rev.*, DOI: 10.1007/s11214-0421-5.

[32] Raeder, J., R. L. McPherron, L. A. Frank, W. R. Paterson, J. B. Sigwarth, G. Lu, H. J. Singer, S. Kokubun, T. Mukai, and J. A. Slavin (2001), Global simulation of the geospace environment modeling substrom challenge event, *J. Geophys. Res., 106*, 381.

[33] Reiff, P. H., T. W. Hill, and J. L. Burch (1977), Solar wind plasma injection at the dayside magnetospheric cusp, *J. Geophys. Res., 82*, 479.

[34] Reme, H., et al. (2001), First multispacecraft ion measurements in and near the earth's magnetosphere with the identical Cluster ion spectrometry (CIS) experiment, *Ann. Geophys., 19,* 1303-1354

[35] Rijnbeek, R. P., S. W. H. Cowley, D. J. Southwood, and C. T. Russell (1984), A survey of dayside flux transfer events observed by ISEE 1 and 2 magnetometers, *J. Geophys. Res., 89*, 786–800.

[36] Rosenbauer, H., H. Gruenwaldt, M. D. Montgomery, G. Paschmann, and N. Skopke (1975), HEOS 2 plasma observations in the distant polar magnetosphere: the plasma mantle, *J. Geophys. Res., 80*, 2723.

[37] Ruohoniemi, J. M., and R. A. Greenwald (1996), Statistical patterns of high-latitude convection obtained from Goose Bay HF radar observations, *J. Geophys. Res., 101*, 21743–21763.

[38] Sato, T. and T. Hayashi (1979), Externally driven magnetic reconnection and a powerful magnetic energy converter, *Phys. Fluids, 22*, 1189, doi:10.1063/1.862721.

[39] Schumacher, J., and B. Kliem (1996), Dynamic current sheets with localized anomalous resistivity, *Phys. Plasmas, 3*, 4703, doi:10.1063/1.872037.

[40] Shelley, E. G., R. D. Sharp, and R. G. Johnson (1976), He^{++} and H^{+} flux measurements in the dayside magnetospheric cusp, *J. Geophys. Res., 81*, 2363.

[41] Shelley, E. G., et al. (1995), The toroidal imaging mass-angle spectrograph (TIMAS) for the Polar mission, *Space Sci. Rev., 71*, 497.

[42] Sibeck, D. G., R. E. Lopez, and E. C. Roelof (1991), Solar wind control of the magnetopause shape, location, and motion, *J. Geophys. Res., 96*(A4), 5489–5495.

[43] Smith, M. F., and M. Lockwood (1996), Earth's magnetospheric cusps, *Rev. Geophys, 34*, 233-260.

[44] Spreiter, J. R., and S. S. Stahara (1985), Magnetohydrodynamic and gas-dynamic theories for planetary bow waves, in *Conllisionless Shocks in the Heliosphere: Reviews of Current Research, Geophys. Monogr. Ser.* , Vol. 35, edited by B. T. Tsurutani and R. G. Stone, p. 85, AGU, Washington, D.C.

[45] Stern, D. P. (1985), Parabolic harmonics in magnetospheric modeling: The main dipole and the ring current, *J. Geophys. Res., 90*, 10851–10863.

[46] Trattner, K. J., S. A. Fuselier, W. K. Peterson, M. Boehm, D. Klumpar, C. W. Carlson, and T. K. Yeoman (2002), Temporal versus spatial interpretation of cusp ion structures observed by two spacecraft, *J. Geophys. Res., 107*(A10), 1287, doi:10.1029/2001JA000181.

[47] Trattner, K. J., S. A. Fuselier, T. K. Yeoman, C. Carlson, W. K. Peterson, A. Korth, H. Reme, J. A. Sauvaud and N. Dubouloz (2005), Spatial and temporal cusp structures observed by multiple spacecraft

and ground based observations, *Surveys in Geophysics, 26*, 281–395, doi:10.1007/s10712-005-1883-3.

[48] Trattner, K. J., S. A. Fuselier, S. M. Petrinec, T. K. Yeoman, C. P. Escoubet, and H. Reme (2008), The reconnection site of temporal cusp structures, *J. Geophys. Res., 113*, A07S14, doi:10.1029/2007JA012776.

[49] Trattner, K. J., J. S. Mulcock, S. M. Petrinec, and S. A. Fuselier (2007), Probing the boundary between antiparallel and component reconnection during southward IMF conditions, *J. Geophys. Res., 112*, A08210, doi:10.1029/2007JA012270.

[50] Tsyganenko, N. A., and D. P. Stern (1996), Modeling the global magnetic field of the large-scale Birkeland current systems, *J. Geophys. Res., 101*, 27187–27198.

[51] Vaivads, A., A. Retino, and Mats Andre (2009), Magnetic reconnection in space plasma, *Plasma Phys. Control. Fusion, 51*, 124016, doi:10.1088/0741-3335/51/12/124016.

[52] Voigt, G.-H. (1986), Magnetospheric equilibrium configurations and slow adiabatic convection, in *Solar Wind-Magnetosphere Coupling*, edited by Y. Kamide and J. A. Slavin, p. 223–273, Terra, Tokyo.

[53] Wing, S., P. T. Newell, and J. M. Rouhoniemi (2001), Double Cusp: Model prediction and observational verification, *J. Geophys. Res., 106*, 25571.

[54] Woch, J., and R. Lundin (1992), Magnetosheath plasma precipitation in the polar cusp and its control by the interplanetary magnetic field, *J. Geophys. Res., 97*, 1421.